**Democratic and Popular Republic of Algeria**

**Ministry of High Education and Scientific Research**

**University of Ferhat Abbas Setif1**

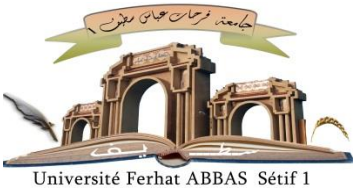


# THESIS

Presented at Faculty of Sciences

Department of Physics

To obtain the degree of

## Doctor

Option: Condensed Matter Physics

By

**LOUBNA DEBACHE**

**Title**

# Study of Fundamental Physical Properties of Some Ternary Nitride-Based Compounds ($Ca_5Si_2N_6$ and $Sr_5Ge_2N_6$).

Discussed publicly at 19 / 05 / 2024 with the board of examiners:

| | | | |
|---|---|---|---|
| Mr. D.MAOUCHE | Professor | Univ. F. ABBAS Setif 1 | Chairman |
| Mr. Y.MEDKOUR | M.C.A | Univ. F. ABBAS Setif 1 | Supervisor |
| Mr. A.BENAMER | M.C.A | ENS Boussaada | Examiner |
| Mr. M.REFFAS | M.C.A | Univ. F. ABBAS Setif 1 | Examiner |
| Mr. A.ROUMILI | Professor | Univ. F. ABBAS Setif 1 | Invited |

## *Acknowledgement*

We thank Allah Almighty first t and thank Him for His bounty, favor, and generosity upon me by facilitating for me a path of knowledge, and for granting me success in accomplishing this humble work. We ask Him, Glory be to Him, to make this work purely for His honorable sake, and to make it an asset for me and a benefit for every seeker of knowledge who desires to serve humanity.

Above all, I would like to express my deep gratitude to my supervisor **Mr YOUCEF MEDKOUR**, Laboratory for Studies of Surfaces and Interfaces of Solid Materials (LESIMS), Ferhat ABBAS SETIF University for his confidence in me during these years, for giving me independence in the work I had to do and for his kind advice, patience and valuable discussions. I wish him great success in his noble career.

I would also like to express my deepest gratitude to Mr. **Abdelkrim ROUMILI** He was like a real link for me, I thank him for his follow-up, his wise advice, his great human qualities and the support he constantly gave me. I wish him a happy long life.

I would like to express my sincere thanks to Ms. **Fatima Djeghloul**, for her wise advice both with regard to the treatment of the subject of my article and with regard to the scientific and human aspects. The thoroughness that went into the long moments spent correcting and discussing the article was really much appreciated. May God grant her success for what he loves and pleases.

To Mr. **Ahmed Kharmouche**, Mr. **Makhlouf Kharoubi** and Mr. **Nacir Guechi** who gives me valuable advice and support which allowed me to benefit from their skills and enthusiasm throughout my research career. Many thanks to them, May God protect them and direct their steps.

I would like to thank my thesis committee members who have done me the honor to agree to read and judge this thesis.

I also extend my gratitude to those who have helped me in some way or another to carry out this work, particularly: **Mr Yusuf. Atalay is a professor of physics at Sakarya University.**

I express my deep gratitude to all members and colleagues, Laboratory for Studies of Surfaces and Interfaces of Solid Materials (LESIMS), for their support and appreciated help.

I am so grateful to all my teachers, professors and colleagues throughout my academic career, from the elementary school to the University.

Finally, I would like to thank my parents who always encouraged me to pursue my scientific way to this distant point, and my brothers, sisters and my all family and friends, for supporting me spiritually throughout this thesis as well as throughout my life.

***LOUBNA DEBACHE***

## Abstract

Our work consists in studying the structural, elastic, electronic, optical, thermoelectric and thermodynamic properties of the ternary nitrides $Ca_5Si_2N_6$ and $Sr_5Ge_2N_6$, using the density functional theory (DFT) within the GGA-PBEsol and TB-mBJ approaches. The theoretically predicted lattice parameters constants are consistent with the available experimental results. According to the estimated cohesive energy, formation enthalpy and Born-Huang stability criterion, the examined compounds are thermodynamically and mechanically stable. Findings on elastic properties suggest that both nitrides are ductile in nature with significant elastic anisotropy. Using the TB-mBJ electronic band structure, these nitrides were found to be semiconductors with a direct band gap (V-V) of 3.55 eV for $Ca_5Si_2N_6$ and indirect band gap (V-Γ) of 3.15eV for $Sr_5Ge_2N_6$. The nitridosilicate compound can be used as a phosphor material because the band gap and Deby temperature values are within the recommended range. Substitution with heavier cations leads to narrowing the Eg value and reducing the $\Theta_D$(K) value. Even that, this material is still useful for other optical applications. The computed optical functions show a modest static dielectric, a notable optical anisotropy and a strong absorptivity of electromagnetic waves in the ultraviolet range, indicating that the title compounds are suitable for UV-optoelectronic applications. Furthermore, transport properties, including Seebeck coefficient, electrical conductivity, thermal conductivity, power factor and figure of merit have been studied employing classical BoltzTrap software. The large figure of merit (ZT) values of these ternary nitrides, suggests their potential use in thermoelectric devices, especially at low and room temperature. Using Debye's quasi-harmonic model, we explored the thermodynamic properties of $Ca_5Si_2N_6$ and $Sr_5Ge_2N_6$ under the effect of temperature and pressure such as: the modulus of compressibility B, coefficient of thermal expansion α, heat capacity at constant volume $C_V$, heat capacity at constant pressure $C_P$ and the Debye temperature $\Theta_D$(K) .



**Keywords:** ternary nitrides; density functional theory; GGA-PBEsol; TB-mBJ; elastic properties; electronic band structure; optical properties; transport properties; thermodynamic properties.

## ملخص

يتكون عملنا من دراسة الخصائص الهيكلية، المرونية، الإلكترونية، البصرية، الكهروحرارية، الديناميكية الحرارية للنيتريدات الثلاثية $Ca_5Si_2N_6$ و$Sr_5Ge_2N_6$ التي تم دراستها باستخدام نظرية الكثافة الوظيفية (DFT) ضمن نهجي GGA-PBEsol وTB-mBJ.ثوابت الشبكة المتوقعة نظريًا توافق النتائج التجريبية المتاحة. وفقًا لطاقة التماسك والطاقة الحرارية للتكوين ومعيار ثبات Born-Huang، فإن المركبات التي تم فحصها مستقرة ديناميكيًا وميكانيكيًا. من خلال استخدام بنية النطاق الإلكتروني TB-mBJ، تم العثور على أن هذه النتريدات لتكون أشباه موصلات ذات فجوة نطاق مباشرة (V-V) تبلغ 3.55 فولتًا لـ $Ca_5Si_2N_6$ وفجوة نطاق غير مباشرة (Γ-V) تبلغ 3.15 فولتًا لـ $Sr_5Ge_2N_6$. يمكن استخدام مركب نيتريدوسيليكات كمادة فسفورية لأن فجوة النطاق وقيم درجة حرارة ديباي تقع ضمن النطاق الموصى به. يؤدي الاستبدال بالكاتيونات الأثقل إلى تضييق قيمة Eg وتقليل قيمة $\Theta_D(K)$. وحتى مع ذلك، فإن هذه المادة لا تزال مفيدة للتطبيقات البصرية الأخرى. تُظهر الوظائف البصرية المحسوبة عازلًا ثابتًا متواضعًا، وتباينًا بصريًا ملحوظًا وامتصاصًا قويًا للموجات الكهرومغناطيسية في نطاق الأشعة فوق البنفسجية، مما يشير إلى أن المركبات المدروسة مناسبة للأشعة الضوئية فوق البنفسجية لتطبيقات الإلكترونية. علاوة على ذلك، تمت دراسة خصائص النقل، بما في ذلك معامل سيبيك، والتوصيل الكهربائي، والتوصيل الحراري، وعامل الطاقة ومعامل الجدارة باستخدام برنامج BoltzTrap الكلاسيكي. وتشير قيم الجدارة الكبيرة (ZT) لهذه النتريدات الثلاثية إلى إمكانية استخدامها في الأجهزة الحرارية، وخاصة في درجة حرارة منخفضة ودرجة حرارة الغرفة. باستخدام نموذج ديباي شبه التوافقي، قمنا باستكشاف الخواص الديناميكية الحرارية لـ $Ca_5Si_2N_6$ و$Sr_5Ge_2N_6$ تحت تأثير درجة الحرارة والضغط مثل: معامل الانضغاط B، معامل التمدد الحراري α، السعة الحرارية عند حجم ثابت $C_V$، السعة الحرارية عند ضغط ثابت $C_P$ ودرجة حرارة ديباي $\Theta_D(K)$.



**الكلمات المفتاحية:** النتريدات الثلاثية؛ نظرية الكثافة المتدرجة؛ تقريب GGA-PBEsol ; TB-mBJ ; الخواص المرنة; بنية النطاق الإلكتروني ; الوظائف الضوئية ; خصائص النقل الكهربائي-الحراري; الخواص الديناميكية الحرارية.

## Résumé

Notre travail consiste à étudier les propriétés structurelles, élastiques, électroniques, optiques, thermoélectriques et thermodynamiques des nitrures ternaires $Ca_5Si_2N_6$ et $Sr_5Ge_2N_6$ en utilisant la théorie fonctionnelle de la densité (DFT) dans le cadre des approches GGA-PBEsol et TB-mBJ. Les paramètres de maille sont cohérents avec les résultats expérimentaux disponibles. Selon l'énergie de cohésion estimée, l'enthalpie de formation et le critère de stabilité de Born-Huang, les composés examinés sont thermodynamiquement et mécaniquement stables. Les résultats sur les propriétés élastiques suggèrent que les deux nitrures sont de nature ductile avec une anisotropie élastique significative. Grâce à l'utilisation de la structure de bande électronique TB-mBJ, ces nitrures révélés d'être des semi-conducteurs avec une bande interdite directe (V-V) de 3,55 eV pour $Ca_5Si_2N_6$ et une bande interdite indirecte (V-Γ) de 3,15 eV pour $Sr_5Ge_2N_6$. Le composé nitridosilicate peut être utilisé comme matériau phosphoreux car les valeurs de bande interdite et de température de Deby se situent dans la plage recommandée. La substitution par des cations plus lourds conduit à un rétrécissement de la valeur Eg et à une réduction de la valeur $\Theta_D$(K). Même cela, ce matériau est toujours utile pour d'autres applications optiques. Les fonctions optiques calculées montrent un diélectrique statique modeste, une anisotropie optique notable et une forte capacité d'absorption des ondes électromagnétiques dans la gamme ultraviolette, indiquant que les composés étudiés conviennent à l'optoélectronique UV.En outre, les propriétés de transport, y compris le coefficient Seebeck, la conductivité électrique, la conductivité thermique, le facteur de puissance (PF) et le facteur de mérite (ZT), ont été étudiées à l'aide du logiciel BoltzTrap. Les grandes valeurs du facteur de mérite (ZT) de ces nitrures ternaires suggèrent leur utilisation potentielle dans les appareils thermoélectriques, en particulier à basse température et à température ambiante. A l'aide du modèle quasi-harmonique de Debye, nous avons exploré les propriétés thermodynamiques de $Ca_5Si_2N_6$ et $Sr_5Ge_2N_6$ sous l'effet de la température et de la pression telles que : le module de compressibilité B, le coefficient de dilatation thermique α, la capacité thermique à volume constant $C_V$, la capacité thermique à pression constante. $C_P$ et la température de Debye $\Theta_D$(K)



**Mots clés :** nitrures ternaires ; la théorie fonctionnelle de la densité; GGA-PBEsol; TB-mBJ ; propriétés élastiques ; structure de bande électronique ; propriétés optiques; propriétés de transport; propriétés thermodynamiques.

# Contents

**Chapter III: Classes of Potentials**



**Chapter IV: Results and Discussions**

# List of Figures

**Figure IV.26:** Variation of the Debye temperature $\theta_D(K)$ with the temperature at different pressures For $Ca_5Si_2N_6$ and $Sr_5Ge_2N_6$.



X

# List of Tables

# CHAPTER I

# GENERAL INTRODUCTION

**Chapter I: General introduction**



## I.1. Preface

Materials science and condensed matter physics are critical components of the current technological revolution Scientists' research, these two areas has led to a lot of exciting discoveries, new materials and new applications. Therefore, condensed matter physics and materials science are being renewed, which are very broad and very active areas of theoretical and experimental scientific research. In fact, before selecting and using a material for a particular technological application, it is essential to ascertain that its properties are adapted to the desired applications as a first step. Therefore, detailed and accurate knowledge of the physical and chemical properties (structural, electronic, mechanical, optical, thermoelectric...etc.) of synthetic materials is important and necessary to determine the possibilities of their use in technological applications. These properties find their origin in the behavior of the electrons inside such systems, knowing the electronic structure is essential to understand material properties. Determination of electronic structures constitute the main object of condensed matter physics. Diverse theoretical methods have been developed by theoretical physicists and chemists allowing for calculate the electronic structures of materials. Let us first mention the semi-experimental methods which require experimental data to determine several adjustable parameters. We should also mention the ab-initio methods (first-principles methods), based on Quantum mechanics theory, which only needs to define atomic constants solid-state electronic structure, such as the Hartree method [1-2] and Hartree-Fock [3] and theory Density functional (DFT: density functional theory) [4]. Ab initio methods have now become an indispensable tool for forecasting and identifying material

properties. Different methods for calculating the properties of solids. It's also a favorite tool for predicting new material, and has been able to replacing expensive experiments or even impossible to perform in a laboratory.

The formality of ab initio calculations comes from Density functional theory (DFT) [5] and its approximation for exchange energy. The fundamental formalism of DFT is based on the theory developed by Hohenberg and Kohn (1964) [6], which holds that the total energy of a system is functional of electron density. The various methods are dependent on the development of DFT. Among the exact methods developed under DFT are the pseudo potential plane wave (PP-PW) [7] and full-potential linear augmented-plane wave (FP-LAPW) methods [8]. In the current dissertation, PP-PW and FP-LAPW based DFT approaches were used to investigate the structural, elastic, electronic, optical, thermoelectric and thermodynamic properties of nitride based materials.

## I.2. Different classes of nitride semiconductors

Nitride semiconductors are a type of material that has nitrogen atoms in its crystalline structure. They are typically wide-band gap semiconductors with a substantial energy difference between the valence and conduction bands. As a result, they are appropriate for a wide range of electronic applications, such as light-emitting diodes (LEDs), laser diodes, and solar cells. [9]

### I.2.1.Binary nitride semiconductors

Binary nitride semiconductors are materials composed of an element from the third column (B, Al, Ga, In, etc.) and an element from the fifth column (N) of the periodic table. They have a wide band gap, meaning that more energy is required to excite an electron from the valence band to the conduction band. This gives them unique properties that make them useful in a variety applications.

Boron nitride (BN) is a non-oxidized ceramic material with a variety of crystallographic forms. It was first synthesized by Balmain in 1842 and commercialized a century later. Boron nitride's excellent properties enable it to be used in a wide range of applications, including tribological systems, optical guides and electronics. Its resistance to high temperatures and chemicals makes it ideal for high-temperature aerospace applications. BN is a III-V compound with four stable polytypic: hexagonal (hBN), cubic (cBN), wurtzite (wBN) and rhombohedra (rBN) [10].

Aluminium nitride (AlN) is a material with unique electrical and thermal conductivity properties, similar to diamond. It is commonly obtained through frittage and is used as a

diffusion barrier. AlN polycristallin is a large gap semi-conductor, ideal for optoelectronics and HEMT applications. However, there is currently no large-scale monocrystalline substrates available. The High Temperature Chemical Vapor Deposition (HTCVD) method from is an alternative method that allows for the growth of high-quality single crystal.develops autoportant AlN monocrystalline substrates. AlN is also a pyzoelectric material due to its high propagation speed and compatibility with silicium filière fabrication. It is used in acoustic filter components for filtering applications. The thickness of AlN films is typically around 500 nm for optimal properties. This thickness range limits filter operating frequencies to a few GHz [11].

Gallium nitride (GaN), discovered in the 1960s, is gaining popularity in optoelectronics and electronics due to its high p-type doping efficiency and excellent material quality. Its wide direct bandgap allows for light emission across a wide spectrum, making it ideal for applications like LEDs and lasers. GaN's crystalline wurtzite structure offers high capacitance and polarization effects, making it ideal for high-power applications. Its potential extends to high-mobility electronic transistors (HEMTs) [12].

## I.2.2. Ternary nitride semiconductors

Ternary nitride semiconductors are composed of three elements: one from group III of the periodic table (e.g., aluminum, gallium, and indium), the secondelement from group V (nitrogen), and a third one, typically a metal or a metalloid. The addition of this third element can significantly alter the properties of the material compared to its binary nitride counterpart. numerous important consequences and several significant effects were observed[13]:

- ✓ Tunable band gap: The band gap, which determines the energy required to excite an electron from the valence band to the conduction band, can be controlled by adding a third element. This allows for tailoring the material for specific optoelectronic applications.
- ✓ Improved carrier mobility: Ternary nitride semiconductors can have higher electron mobility than Binary nitride semiconductors, which is beneficial for high-power electronic devices.
- ✓ Enhanced thermal conductivity: The addition of third element can improve the thermal conductivity of Binary nitride semiconductors, which is important for heat dissipation in devices.

## I.2.3. Quaternary nitride semiconductors

Quaternary nitride semiconductors are materials made from four elements, with nitrogen as the common component. These materials are used in optoelectronics and electronics due to their tunable band gaps, making them suitable for devices like LEDs, lasers, and solar cells [13]. Researchers are exploring doping techniques to improve efficiency, durability, and performance in these semiconductors.

## I.3. Presentation of the studied materials

The investigation of new ternary and quaternary nitrides have gained a significant importance during this last ten years [14-15]. In minutely, by using molten Na as a flux, many nitride compounds containing alkaline earths with novel structures and interesting properties have been synthesized [16-17]. Single crystals of many ternary and quaternary nitride compounds containing Si, Ge and Ga have been synthesized [18]. When obtaining these metal nitrides, alkaline earth metal was often added in the molten Na to improve the solubility of nitrogen, and finally incorporated into the nitride products. In most cases, the nitride products contained anions of nitride-metalloid whose charge was counterbalanced by alkaline-earth cations [17].

Interestingly, the large and heavy alkaline earth metals (Sr and Ba) are prevalent, and the Ca containing ternary nitride is rare.

In our work, we are interested to study the physical properties of ternary materials, based on nitrogen and alkaline earth (Ca and Sr) containing an element from the main group IV metalloid (Si, Ge). To the best of our knowledge and apart from the development and the determination of structural parameters of these ternary materials $Ca_5Si_2N_6$ and $Sr_5Ge_2N_6$ [19-20], their fundamental physical properties have not yet been studied experimentally or theoretically.

Silicon Calcium Nitride $Ca_5Si_2N_6$ and Germanium Strontium Nitride $Sr_5Ge_2N_6$ consist of:

- ✓ Calcium Ca: (Z= 20, [Ar] $4s^2$) was discovered by Davy in 1808. It belongs to the alkaline earth metals, which belong to group II of the periodic table of elements. This metal is characterized by its chemical activity, therefore it does not exist in its free form in nature, since a layer of oxide and nitride forms on its surface when exposed to air. This element is similar in its chemical and physical properties to the properties of its heavier peers in the group of alkali metals: strontium and barium. Calcium is the

fifth chemical element in terms of natural abundance in the earth's crust and the third metal in terms of order, after aluminum and iron. It is most often found in the form of a compound of calcium carbonate, which enters into the composition of limestone; it is also found as other compounds in the minerals gypsum, anhydrite, fluorite and apatite, which are also natural raw materials for calcium.

- ✓ Strontium Sr :( Z=38, [Kr] $5s^2$ is a silvery-white soft-yellow metallic element that is highly reactive chemically.

The outer shell of individual atoms in Group IV (Si, Ge) elements is exactly half filled, making them unique in the periodic table. A three-dimensional tetravalent crystal structure with no preferential direction can be realized by exchanging four outer shell electrons with another group IV atom.

- ✓ Silicon Si: (Z=14, [Ne] $3s^2$ $3p^2$) It is classified as a semiconductor and metalloid, and is found under standard conditions in the form of a brittle crystalline solid with a bluish-gray metallic luster.
- ✓ Germanium Ge: (Z=32, [Ar] $3d^{10}$ $4s^2$ $4p^2$) A semiconductor, metalloid chemical element in appearance, a greyish-white solid with a greenish-yellow color.
- ✓ Nitrogen N: (Z=7, [He] $2s^2$ $2p^3$) is a chemical element located in the group V in the periodic table and is classified among the nonmetals, and it is in normal conditions of pressure and temperature in the form of $N_2$. It is a diatomic gas, colorless, tasteless and odorless.

The title compounds ($Ca_5Si_2N_6$ and $Sr_5Ge_2N_6$) adopt a monoclinic crystal structure and belong to the space group C2/c (N°:15), with four unit formula per unit cell (Z=4) [19-20].

## I.4. Motivation and key objectives

Over the last few decades, a large variety of solid-state nitride materials were synthesized and exploited in many novel technologies. Including innovations revolving around photovoltaic solar cells, thermoelectric, high-temperature ceramics or optoelectronics [21-26]. With regard to reducing global energy consumption, different classes of nitrides exhibit luminescence properties upon doping with rare earth ions such as $Eu^{2+}$or $Ce^{3+}$, making them suitable as luminescent materials for light emitting diodes (LEDs) [27-33]. Herein, for example, two subclasses -nitridosilicates and nitridoaluminates- are widely used as host structures for luminescent materials (i.e. LED phosphors) due to their large structural

diversity, chemical and optical properties [31,34-37]. Especially, the $Eu^{2+}$doped $M_xSi_yN_z$ nitridosilicates phosphors (M = alkali, alkaline earth or rare earth) such as: $Sr_2Si_5N_8:Eu^{2+}$ [33], $(A)_2Si_5N_8$ (A= Ca, Sr, Ba) :$Eu^{2+}$[36,39],$(A)(R)Si_4N_7:Eu^{2+}$(A = Ca, Sr, Ba; R = Sc, Y, Lu)[40-44], $BaSi_7N_{10}:Eu^{2+}$[45]and $(A)SiN_2:Eu^{2+}$(A= Ca, Sr, Ba)[46-47]. Furthermore, the latter compositional range can be further extended by substituting Al and O for Si and N respectively [48], resulting in phosphors like $CaAlSiN_6:Eu^{2+}$[49], $Ba_3Si_6O_{12}N_2$: $Eu^{2+}$[50], $(A)Si_2O_2N_2:Eu^{2+}$(A= Ca, Sr, Ba) [51], $Sr[LiAl_3N_4]:Eu^{2+}$[37] and $A[Mg_2Al_2N_4]:Eu^{2+}$ (A= Ca, Sr, Ba) [52].

Recently, a new red phosphor, $Ca_5Si_2N_6$: $Eu^{2+}$, was discovered by J. Huang et. Al [53]. This phosphor has an excitation band that extends from 350 to 480 nm, which makes it attractive for application in phosphor-converted light-emitting diode [53]. Structurally, $Ca_5Si_2N_6$ contains pairs of edge-sharing tetrahedra of $[Si_2N_6]^{10-}$similar to the previously identified in other nitridosilicates like: $Ba_5Si_2N_6$ or $Ca_7NbSi_2N_9$ [19]. Comparable "bow-tie" units of $[Ge_2N_6]^{10-}$ were found in $Sr_5Ge_2N_6$, suggests the presence of structural relations between nitridosilicates and nitridogermanates [20].

Due to technological uses for these materials, we have decided to study the recently discovered nitridogermanate $Sr_5Ge_2N_6$ [20] and its nitridosilicate isotope, $Ca_5Si_2N_6$ [19]. Aside from their synthesis and structural characterization [19, 20], the fundamental physical properties of these nitrides have not yet been investigated, either experimentally or theoretically. These facts stimulate us to conduct a thorough investigation on their fundamental physical properties, which are crucial to identify the potential uses of these compounds. As a result, in this paper, we have the following:

- Exact determination of crystalline parameters, including lattice parameters and atomic positions, of the $Ca_5Si_2N_6$ and $Sr_5Ge_2N_6$ materials using the PP-PW method and GGA-PBEsol to model the exchange energy [54] as implemented in the CASTEP code [55]. The structural stability of the studied materials were also verified by calculating the formation enthalpy and cohesion energy.
- Prediction of the elastic properties of the studied compounds using the efficient stress-strain method as implemented in the CASTEP.
- Overview investigation of the electronic properties (including electronic band structure, total and partial density of states) and optical properties (including the dielectric function and important derived parameters such as absorption coefficient, refractive index, extinction coefficient, reflectance and electron energy loss function).

These investigations were conducted using FP-LAPW with GGA08 and TB-mBJ method [56] for modeling the exchange-correlation potential.

- Investigation of the thermoelectric properties, including Seebeck coefficient, electric conductivity, thermal conductivity, power factor and figure of merit, using the FP-LAPW method combined with the Boltzmann's semi-classical theory [57] as implemented in the BoltzTraP code [58].
- Investigation of the thermodynamic properties, including the module of compression B, coefficient of thermal expansion α, heat capacity at constant volume $C_V$, heat capacity at constant pressure $C_P$ and the Debye temperature $\Theta_D$, using the E-V data of the PP-PW and GIBBS program [59].

## I.5. Thesis outline

As part of this thesis, we represent four chapters.

**Chapter 1;** General introduction, bear a Preface, different classes of nitride semiconductors, presentation of materials and motivation and key objectives.

**Chapter 2;** We present in this chapter the theory on which our calculations are based, namely the density functional theory (DFT). The Schrödinger equation, the Born-Oppenheimer approximation, the generalized Kohn and Sham equations, the method used for solving the Kohn and Sham equations and exchange correlation energy approximations.

**Chapter 3;** This chapter is devoted to the details of classes of potentials such as; pseudo-potentials and the all-electron potentials: Muffin-tin type or Full Potential.

**Chapter 4;** This last chapter is dedicated to the results and discussions: we first performed a study on the structural and elastic properties using the PP-PW method. Next, we have investigated the electronic and optical properties, using the FP-LAPW and GGA08. TB-mBJ method for modeling the exchange-correlation potential. The study of the thermoelectric properties, including Seebeck coefficient, electric conductivity, thermal conductivity, power factor and figure of merit, using the FP-LAPW method combined with the Boltzmann's semi-classical theory as implemented in the BoltzTraP code. Finally, thermodynamic properties are also predicted via the combination of the Debye quasi-harmonic model as implemented in GIBBS program. We have ended this thesis by a general conclusion.

## References

[1] Hartree, D. R. (1928, January). The wave mechanics of an atom with a non-coulomb central field. Part II. Some results and discussion. In *Mathematical Proceedings of the Cambridge Philosophical Society* (Vol. 24, No. 1, pp. 111-132). Cambridge University Press.
[2] DR, H. F. (1947). The calculation of atomic structures.
[3] Lykos, P., & Pratt, G. W. (1963). Discussion on the Hartree-Fock approximation. *Reviews of Modern Physics*, *35*(3), 496.
[4] Dreizler, R. M., & Gross, E. K. (2012). *Density functional theory: an approach to the quantum many-body problem*. Springer Science & Business Media.
[5] Parr, R. G., & Yang, W. (1989). Density-functional theory of atoms and molecules Oxford Univ. Press. *ed: Oxford*.
[6] Hohenberg, P., & Kohn, W. (1964). Inhomogeneous electron gas. *Physical review*, *136*(3B), B864.
[7] Hamann, D. R., Schlüter, M., & Chiang, C. (1979). Norm-conserving pseudopotentials. *Physical Review Letters*, *43*(20), 1494.
[8] Mattheiss, L. F., & Hamann, D. R. (1986). Linear augmented-plane-wave calculation of the structural properties of bulk Cr, Mo, and W. *Physical Review B*, *33*(2), 823.
[9] Moustakas, T. D., and Paiella, R. (2017). Optoelectronic device physics and technology of nitride semiconductors from the UV to the terahertz. *Reports on Progress in Physics*, *80*(10), 106501
[10] Weng, Q., Wang, X., Wang, X., Bando, Y., & Golberg, D. (2016). Functionalized hexagonal boron nitride nanomaterials: emerging properties and applications. *Chemical Society Reviews*, *45*(14), 3989-4012.
[11] Akasaki, I. (1998). Progress in crystal growth and future prospects of group III nitrides by metalorganic vapor-phase epitaxy. *Journal of crystal growth*, *195*(1-4), 248-251.
[12] Strite, S., Lin, M. E., & Morkoc, H. (1993). Progress and prospects for GaN and the III–V nitride semiconductors. *Thin Solid Films*, *231*(1-2), 197-210.
[13] Chen, F., Ji, X., & Lau, S. P. (2020). Recent progress in group III-nitride nanostructures: From materials to applications. *Materials Science and Engineering: R: Reports*, *142*, 100578.
[14] Luo, H., Wang, H., Zou, G., Bauer, E., McCleskey, T. M., Burrell, A. K., & Jia, Q. (2010). A review of epitaxial metal-nitride films by polymer-assisted deposition. *Transactions on Electrical and Electronic Materials*, *11*(2), 54-60.
[15] Hintze, F., Hummel, F., Schmidt, P. J., Wiechert, D., & Schnick, W. (2012). $Ba_3Ga_3N_5$ A Novel Host Lattice for Eu2+-Doped Luminescent Materials with Unexpected Nitridogallate Substructure. *Chemistry of Materials*, *24*(2), 402-407.
[16] Yamane, H., & DiSalvo, F. J. (1996). A barium germanium nitride, $Ba_3Ge_2N_2$, containingx1| Ge2− and GeN24− anions. *Journal of alloys and compounds*, *241*(1-2), 69-74.
[17] Park, D. G., Gal, Z. A., & DiSalvo, F. J. (2005). Synthesis and Structure of $Sr_6Ge_5N_2$ and $Ba_6Ge_5$ $N_2$. *Bulletin of the Korean Chemical Society*, *26*(10), 1543-1548.
[18] Niewa, R., & Jacobs, H. (1996). Group V and VI alkali nitridometalates: a growing class of compounds with structures related to silicate chemistry. *Chemical reviews*, *96*(6), 2053-2062.
[19] Ottinger, F., & Nesper, R. (2005). Synthesis and crystal structure of the nitridosilicates $Ca_5[Si_2N_6]$ and $Ca_7$ $[NbSi_2N_9]$. *Zeitschrift für anorganische und allgemeine Chemie*, *631*(9), 1597-1602.
[20] Junggeburth, S. C., Oeckler, O., & Schnick, W. (2008). $Sr_5Ge_2N_6$–A Nitridogermanate with Edge-sharing Double Tetrahedra. *Zeitschrift für anorganische und allgemeine Chemie*, *634*(8), 1309-1311.

[21] Chatterjee, U., Park, J. H., Um, D. Y., & Lee, C. R. (2017). III-nitride nanowires for solar light harvesting: A review. *Renewable and Sustainable Energy Reviews*, *79*, 1002-1015.
[22] Lu, N., & Ferguson, I. (2013). III-nitrides for energy production: photovoltaic and thermoelectric applications. *Semiconductor Science and Technology*, *28*(7), 074023.
[23] Sharma, V., Kagdada, H. L., Jha, P. K., Śpiewak, P., & Kurzydłowski, K. J. (2020). Thermal transport properties of boron nitride based materials: A review. *Renewable and Sustainable Energy Reviews*, *120*, 109622.
[24] Shibata, N., Pennycook, S. J., Gosnell, T. R., Painter, G. S., Shelton, W. A., & Becher, P. F. (2004). Observation of rare-earth segregation in silicon nitride ceramics at subnanometre dimensions. *Nature*, *428*(6984), 730-733.
[25] Zeuner, M., Pagano, S., & Schnick, W. (2013). Nitridosilicates and oxonitridosilicates: from ceramic materials to structural and functional diversity. *Ceramics Science and Technology*, 373-413.
[26] Moustakas, T. D., & Paiella, R. (2017). Optoelectronic device physics and technology of nitride semiconductors from the UV to the terahertz. *Reports on Progress in Physics*, *80*(10), 106501.
[27] Pust, P., Schmidt, P. J., & Schnick, W. (2015). A revolution in lighting. *Nature materials*, *14*(5), 454-458..
[28] He, X. H., Lian, N., Sun, J. H., & Guan, M. Y. (2009). Dependence of luminescence properties on composition of rare-earth activated (oxy) nitrides phosphors for white-LEDs applications. *Journal of materials science*, *44*(18), 4763-4775.
[29] Qin, X., Liu, X., Huang, W., Bettinelli, M., & Liu, X. (2017). Lanthanide-activated phosphors based on 4f-5d optical transitions: theoretical and experimental aspects. *Chemical reviews*, *117*(5), 4488-4527.
[30] Wang, L., Xie, R. J., Suehiro, T., Takeda, T., & Hirosaki, N. (2018). Down-conversion nitride materials for solid state lighting: recent advances and perspectives. *Chemical reviews*, *118*(4), 1951-2009.
[31] Schmiechen, S., Schneider, H., Wagatha, P., Hecht, C., Schmidt, P. J., & Schnick, W. (2014). Toward new phosphors for application in illumination-grade white pc-LEDs: the nitridomagnesosilicates Ca $[Mg_3SiN_4]$: Ce3+, Sr [Mg3SiN4]: Eu2+, and Eu $[Mg_3SiN_4]$. *Chemistry of Materials*, *26*(8), 2712-2719.
[32] Uheda, K., Hirosaki, N., & Yamamoto, H. J. P. S. S. (2006). Host lattice materials in the system $Ca_3N_2$–AlN–Si3N4 for white light emitting diode. *physica status solidi (a)*, *203*(11), 2712-2717.
[33] Zeuner, M., Schmidt, P. J., & Schnick, W. (2009). One-pot synthesis of single-source precursors for nanocrystalline LED phosphors M2Si5N8: Eu2+ (M= Sr, Ba). *Chemistry of materials*, *21*(12), 2467-2473.
[34] Xie, R. J., & Hirosaki, N. (2007). Silicon-based oxynitride and nitride phosphors for white LEDs—A review. *Science and technology of Advanced Materials*, *8*(7-8), 588.
[35] Xie, R. J., & Hintzen, H. T. (2013). Optical properties of (oxy) nitride materials: a review. *Journal of the American Ceramic Society*, *96*(3), 665-687.
[36] Höppe, H. A., Lutz, H., Morys, P., Schnick, W., & Seilmeier, A. (2000). Luminescence in $Eu^{+2}$-doped $Ba_2Si_5N_8$: fluorescence, thermoluminescence, and upconversion. *Journal of Physics and Chemistry of Solids*, *61*(12), 2001-2006.
[37] Pust, P., Weiler, V., Hecht, C., Tücks, A., Wochnik, A. S., Henß, A. K., ... & Schnick, W. (2014). Narrow-band red-emitting Sr [LiAl3N4]: $Eu^{+2}$ as a next-generation LED-phosphor material. *Nature materials*, *13*(9), 891-896.
[38] Van Krevel, J. W. H. (2000). On new rare-earth doped M-Si-Al-ON materials: Luminescence properties and oxidation resistance.

[39] Li, Y. Q., Van Steen, J. E. J., Van Krevel, J. W. H., Botty, G., Delsing, A. C. A., DiSalvo, F. J., ... & Hintzen, H. T. (2006). Luminescence properties of red-emitting $M_2Si_5N_8$: $Eu^{+2}$ (M= Ca, Sr, Ba) LED conversion phosphors. *Journal of alloys and compounds*, *417*(1-2), 273-279.
[40] Cho, I. H., Anoop, G., Suh, D. W., Lee, S. J., & Yoo, J. S. (2012). On the stability and reliability of $Sr_{1-x}Ba_xSi_2O_2N_2$: $Eu^{+2}$ phosphors for white LED applications. *Optical Materials Express*, *2*(9), 1292-1305.
[41] Li, Y. Q., de With, G., & Hintzen, H. T. (2004). Synthesis, structure, and luminescence properties of $Eu^{+2}$ and $Ce^{+3}$ activated $BaYSi_4N_7$. *Journal of alloys and compounds*, *385*(1-2), 1-11.
[42] Kurushima, T., Gundiah, G., Shimomura, Y., Mikami, M., Kijima, N., & Cheetham, A. K. (2010). Synthesis of Eu2+-Activated MYSi4N7 (M= Ca, Sr, Ba) and SrYSi4− x Al x N7− x O x (x= 0–1) Green Phosphors by Carbothermal Reduction and Nitridation. *Journal of the Electrochemical Society*, *157*(3), J64.
[43] Park, W. B., Son, K. H., Singh, S. P., & Sohn, K. S. (2012). Solid-State Combinatorial Screening of $ARSi_4N_7$: $Eu^{+2}$ (A= Sr, Ba, Ca; R= Y, La, Lu) Phosphors. *ACS Combinatorial Science*, *14*(10), 537-544.
[44] Wang, X., Seto, T., Zhao, Z., Li, Y., Wu, Q., Li, H., & Wang, Y. (2014). Preparation of $Sr_{1-x}Ca_xYSi_4N_7$: $Eu^{+2}$ solid solutions and their luminescence properties. *Journal of Materials Chemistry C*, *2*(22), 4476-4481.
[45] Li, Y. Q., Delsing, A. C. A., Metslaar, R., de With, G., & Hintzen, H. T. (2009). Photoluminescence properties of rare-earth activated BaSi7N10. *Journal of Alloys and Compounds*, *487*(1-2), 28-33.
[46] Duan, C. J., Wang, X. J., Otten, W. M., Delsing, A. C., Zhao, J. T., & Hintzen, H. T. (2008). Preparation, electronic structure, and photoluminescence properties of Eu2+-and $Ce^{+3}Li^{+}$-activated alkaline earth silicon nitride $MSiN^2$ (M=Sr,Ba). *Chemistry of materials*, *20*(4), 1597-1605.
[47] Xie, R. J., Li, Y. Q., Hirosaki, N., & Yamamoto, H. (2011). *Nitride phosphors and solid-state lighting*. Boca Raton, FL: Taylor & Francis.
[48] Liu, R. S. (Ed.). (2017). *Phosphors, up conversion nano particles, quantum dots and their applications* (Vol. 1). Berlin/Heidelberg, Germany: Springer.
[49] Uheda, K., Hirosaki, N., Yamamoto, Y., Naito, A., Nakajima, T., & Yamamoto, H. (2006). Luminescence properties of a red phosphor, $CaAlSiN_3$: $Eu^{+2}$, for white light-emitting diodes. *Electrochemical and solid-state letters*, *9*(4), H22.
[50] Mikami, M., Shimooka, S., Uheda, K., Imura, H., & Kijima, N. (2009). New green phosphor $Ba_3Si_6O_{12}N_2$: Eu for white LED: crystal structure and optical properties. In *Key Engineering Materials* (Vol. 403, pp. 11-14). Trans Tech Publications Ltd.
[51] Li, Y. Q., & Delsing, A. C. A. (2005). G. de With and HT Hintzen. *Chem. Mater*, *17*(12), 3242-3248.
[52] Pust, P., Hintze, F., Hecht, C., Weiler, V., Locher, A., Zitnanska, D.& Schnick, W. (2014). Group (III) Nitrides M $[Mg_2Al_2N_4]$(M= Ca,Sr,Ba,Eu) and Ba $[Mg_2Ga_2N_4]$ Structural Relation and Nontypical Luminescence Properties of $Eu^{+2}$ Doped Samples. *Chemistry of Materials*, *26*(21), 6113-6119.
[53] HUANG, J., JIANG, T., YAO, N., LI, H., & XU, X. (2015). Synthesis and Characterization of Novel Nitride Phosphors $Ca_5Si_2N_6$:$Eu^{+2}Ce^{3+}$. *Asian Journal of Chemistry*, *27*(3).
[54] Perdew, J. P., Ruzsinszky, A., Csonka, G. I., Vydrov, O. A., Scuseria, G. E., Constantin, L. A., ... & Burke, K. (2008). Restoring the density-gradient expansion for exchange in solids and surfaces. *Physical review letters*, *100*(13), 136406.

[55] Clark, S. J., Segall, M. D., Pickard, C. J., Hasnip, P. J., Probert, M. I., Refson, K., & Payne, M. C. (2005). First principles methods using CASTEP. *Zeitschrift für kristallographie-crystalline materials*, *220*(5-6), 567-570.
[56] Koller, D., Tran, F., & Blaha, P. (2012). Improving the modified Becke-Johnson exchange potential. *Physical Review B*, *85*(15), 155109.
[57] Kireev, P. S. (1975). Physics of semiconductors. *Vysshaya Shkola, Moscow*, *584*.
[58] Madsen, G. K., & Singh, D. J. (2006). BoltzTraP. A code for calculating band-structure dependent quantities. *Computer Physics Communications*, *175*(1), 67-71.
[59] Blanco, M. A., Francisco, E., & Luana, V. (2004). GIBBS: isothermal-isobaric thermodynamics of solids from energy curves using a quasi-harmonic Debye model. *Computer Physics Communications*, *158*(1), 57-72.

# CHAPTER II

# THEORETICAL BACKGROUND OF THE DENSITY FUNCTIONAL THEORY (DFT)

.

**Chapter II: Theoretical Background of the Density Functional Theory (DFT)**



## II.1. Preface

The physics of condensed materials is the branch of physics which studies the microscopic properties of matter and is interested in understanding and exploring the interactions of electrons with each other and with nuclei. In principle, all material properties can be addressed if one has efficient computational tools to solve this quantum mechanical problem. Calculating the ground state properties of N-electron in crystal is very difficult, because every particle interacts with every other particle. The Schrödinger equation therefore becomes mathematically insoluble. Several approximations have been made to solve this difficult situation. One of the methods used is density functional theory (DFT), developed by Hohenberg and Kohn [1].

.

## II.2. Schrödinger Equation

If we consider a crystal system consisting of two types of particles: nuclei and electrons in mutual interaction. To study all these interactions, Schrödinger proposed an equation:

$$H\Psi = E\Psi \qquad \text{(II.1)}$$

Where;

Ψ is the wave function of the system, a function of the coordinates of the nuclei, of the electrons, it contains all information of the system.

E is the total energy.

H is The corresponding total Hamiltonian of the system, it describes all the interactions occurring in the system. It is expressed in its exact following form:

$$H = (T_e + T_n + V_{ee} + V_{ne} + V_{nn}) \qquad \text{(II.2)}$$

with:

$T_e = \sum_i T_i = \sum_i \left( -\frac{-\hbar^2}{2m_e} \Delta_i \right)$ is the electron's kinetic energy operator,

$T_n = \sum_\alpha T_\alpha = \sum_\alpha \left( \frac{-\hbar^2 \Delta_\alpha}{2M} \right)$ is the nuclei's kinetic energy operator,

$V_{ee} = \frac{1}{2} \sum_{i \neq j} \frac{e^2}{|r_i - r_j|} = \frac{1}{2} \sum_{i \neq j} V_{ij}$ is the electron/electron interaction energy operator,

$V_{ne} = -\sum_i \sum_\alpha \frac{Z_\alpha e^2}{|r_i - R_\alpha|} = \sum_i \sum_\alpha V_{i\alpha}$ is the nuclei/electron interaction energy operator,

$V_{nn} = \frac{1}{2} \sum_{\alpha \neq \beta} \frac{Z_\alpha Z_\beta e^2}{|R_\alpha - R_\beta|} = \frac{1}{2} \sum_{\alpha \neq \beta} V_{\alpha\beta}$ is the nucleus/nucleus interaction energy operator.

$r_i$ and $R_\alpha$ respectively designating the electronic and nuclear position vectors serving for the localization of each of the i electrons of the system and of each of its α nuclei, centered on its atomic sites. The indices i (= 1...N) and α = (1...Z) are thus adopted in order to distinguish electronic quantities from nuclear quantities.

The Schrödinger equation can be therefore represented in the form:

$$(T_e + T_n + V_{ee} + V_{ne} + V_{nn})\, \Psi(r_1, r_2 ... R_1, R_2 ...) = E\, \Psi(r_1, r_2 ... R_1, R_2 ...) \qquad \text{(II.3)}$$

.

Due to the high number of degrees of freedom 3N(Z+1) and the involved interactions in this type of problem, their exact treatment has proven to be an impossible task [2]. One of the recommended solutions is the use of appropriate and simplifying approximations. First, find **the Born-Oppenheimer approximation.**

## II.2.1. Born-Oppenheimer Approximation

The Born-Oppenheimer approximation proposed to simplify the resolution of the Schrödinger equation (II.1) by separating the electronic part from the nuclear part in the wave function. This approximation is based on the fact that nuclei are much heavier and therefore much slower than electrons. Therefore only electrons are kept as actors of our many bodily problems. The nuclei is deprived of this mode, and are reduced to a specific source of positive charge, and become "external" with respect to the cloud. After applying this approximation, we are left with a group of N negative particles interacting and moving in the potential of the nuclei.

By adopting this approximation, if we consider that the nuclei are fixed, the Hamiltonian $H= (T_e + T_n + V_{ee} + V_{ne} + V_{nn})$ Will be simplified since the kinetic energy of the nuclei becomes zero and the interaction energy between the nuclei becomes constant which we can choose as the origin of the energies $(T_n = 0, V_{nn} = cste)$ Taking this simplification into account, the Hamiltonian system becomes [3-4]:

$$H= (T_e + + V_{ee} + V_{ne}) \qquad \text{(II.4)}$$

## II.2.2. Hartree approximation

The Hartree approximation consists in seeking the eigenfunctions of H in the approximate form:

$$\Psi_{\text{approchée}} = \Psi(r_1)\, \Psi(r_2) \ldots\ldots\ldots\ldots \Psi(r_N) \qquad \text{(II.5)}$$

This approximation is based on the assumption of free electrons, which amounts to not holding Spin count [5].

## II.2.3. Hartree–Fock approximation

A so-called Hartree-Fock approximation has been introduced to take into account the spin of the electrons for the resolution of the Schrödinger equation. The wave function ψ is expressed using a Slater determinant. The exchange energy is processed exactly and the correlation energy is only introduced in the most advanced versions [6].

.

## II.3. Density functional theory

The energy of an electronic system can be expressed as a function of its density. It is on this idea that the density functional theory was founded. It's actually an old idea that originated in the work of Thomas and Fermi [7-8] in the late 1920s, but it wasn't until the mid-1960s that the contributions of Hohenberg and Kohn [9] on the one hand and Kohn and Sham [10] on the other hand make it possible to establish the theoretical formalism on which rests the DFT. Fundamental variable to describe the properties of the system has existed since the first approaches to the electronic structure of matter but it only obtained tangible results. Through the demonstration of the two theorems known as Hohenberg and Kohn.

### II.3.1. Hohenberg-Kohn theorems

The Hohenberg-Kohn theorem is based on the determination of the set of properties of the ground state of a system composed of a number of electrons, in Coulomb interaction with point nuclei, using the single knowledge of electron density. The two authors Hohenberg and Kohn proved two fundamental theorems whose statements are as follows [9]:

**Theorem 1: The total ground state energy E of a multi-electron system is a unique functional of the electron density $\rho(\mathrm{r})$ for an external potential $V_{ex}$**

We can write:

$$E\left[\rho(\mathrm{r})\right]=\int V_{ex}(r)\rho(\mathrm{r})dr+F\left[\rho(\mathrm{r})\right] \qquad (\mathrm{II}.6)$$

With

$$F\left[\rho(\mathrm{r})\right]=T\left[\rho(\mathrm{r})\right]+E_{ee}\left[\rho(\mathrm{r})\right] \qquad (\mathrm{II}.7)$$

and ;

$\rho(\mathrm{r})$ is the electron density and $F\left[\rho(\mathrm{r})\right]$ is a universal functional of ρ that contains the kinetic and Coulomb contributions to the energy.

The term $\int V_{ex}(r)\rho(\mathrm{r})dr$ stands for nucleus-electron interaction.

**Theorem 2: The total energy functional of any many-particle system has a minimum which corresponds to the ground state and the ground state particle density.**

The second theorem is based on the variation principle: Hohenberg and Kohn proved that any energy E(Ψ), satisfying the necessary limits $\rho(\mathrm{r})\geq 0$ and $\int\rho(\mathrm{r})dr=N$ and which

.

is associated with an external potential $V_{ex}(\mathrm{r})$, is always greater than or equal to that of the ground state E [ρ(r)]. In this case, the ground state energy will be written as:

$$E\left[\rho(\mathrm{r})\right]=\int V_{ex}(r)\rho(\mathrm{r})dr+T\left[\rho(\mathrm{r})\right]+E_{ee}\left[\rho(\mathrm{r})\right] \qquad (\mathrm{II}.8)$$

$T\left[\rho(\mathrm{r})\right]$ is the kinetic energy of the electronic system and $E_{ee}\left[\rho(\mathrm{r})\right]$ is the repulsive electron-electron interaction functional. It breaks down into two functions .

$$E_{ee}\left[\rho(\mathrm{r})\right]=J\left[\rho(\mathrm{r})\right]+E_{XC}\left[\rho(\mathrm{r})\right] \qquad (\mathrm{II}.9)$$

and ;

$J\left[\rho(\mathrm{r})\right]$ is the Coulomb functional of classical electron-electron interactions:

$$J\left[\rho(\mathrm{r})\right]=\frac{1}{2}\iint\frac{\rho(\mathrm{r}_1)\rho(\mathrm{r}_2)}{\mathrm{r}_1-\mathrm{r}_2}d\mathrm{r}_1d\mathrm{r}_2 \qquad (\mathrm{II}.10)$$

and $E_{XC}\left[\rho(\mathrm{r})\right]$ is the exchange-correlation functional which contains all the non-classical electron-electron interactions [11].

## II.3.2. The Kohn-Sham equations

A year later, after Hohenberg and Kohn [9] had published their work on density functional theory, Kohn and Sham proposed a practical approach to further simplify Hohenberg and Kohn's theory. They introduced an auxiliary system of electrons without interaction where the distribution of the charge density in the ground state is written;

$$\rho(\mathrm{r})=\sum_{i=1}^{N}\left|\Phi_i(r)\right|^2 \qquad (\mathrm{II}.11)$$

The wave functions that minimize the density functional are solutions of these eigenvalue equations. The wave functions are determined from an equation similar to the Schrödinger equation in a self-consistent way.

The equation is given with an effective potential:

$$\left[-\frac{\hbar^2}{2m}\Delta_i+V_{eff}(r)\right]\Psi_i(r)=E_i\Psi_i(r) \qquad (\mathrm{II}.12)$$

Knowing that the effective potential is given by:

.

$$V_{eff}(r)=V_{ext}(r)+V_{H}(r)+V_{xc}(r) \qquad (II.13)$$

$V_{ext}(r)$ is the term due to the external potential coming from the nuclei;

$$V_{ext}(r)=\frac{\partial E_{ext}[\rho(r)]}{\partial\rho(r)} \qquad (II.14)$$

$V_{H}(r)$ is Hartree's potential;

$$V_{H}(r)=\frac{\partial E_{H}[\rho(r)]}{\partial\rho(r)}=\iint\frac{\rho(r)\rho(r')}{r-r'}drdr' \qquad (II.15)$$

$V_{xc}(r)$ is the exchange-correlation potential defined as a functional derivative of the exchange-correlation energy $E_{XC}$

$$V_{xc}(r)=\frac{\partial E_{xc}[\rho(r)]}{\partial\rho(r)} \qquad (II.16)$$

The single-particle wave functions $\Phi_{i}(r)$ are the N lowest-energy solutions of the Schrödinger equation written within the framework of Kohn-Sham theory as follows:

$$H_{KS}\Phi(r)=\varepsilon_{i}\Phi_{i}(r) \qquad (II.17)$$

## II.4. Solving the Kohn–Sham equation

To solve the Kohn-Sham equation we need to define the Hartree potential and the exchange-correlation potential. It is therefore necessary to determine the electron density which is itself dependent on the wave function [12]. This self-consistent problem is solved using the following algorithm:

1. Define an initial test for the electron density $\rho(r)$
2. Build potential
3. Solve the Kohn-Sham equation, to find the wave function of a single particle $\Phi(r)$

.

4. Calculate the new electron density $\rho_{KS}(\mathrm{r})$ using the wave function obtained in the previous step.

5. Compare the electron density $\rho_{KS}(\mathrm{r})$ with the test density $\rho(\mathrm{r})$, if they are equal then the density $\rho_{KS}(\mathrm{r})$ is the ground state electron density so can calculate the total energy, otherwise start again with step 2.

So this process is a repetitive self-consistent method which allows to solve the Kohn-Sham equations [12].

## II.5. Exchange-Correlation potential

The only ambiguity in the approach of Kohn and Sham (KS) is the term of exchange-correlation, the complexity of the latter makes the resolution of the KS equations difficult. Nevertheless. This functional can be subject to approximations of the local or near local order of the density, that said the energy $E_{xc}$ can be written in the form:

$$E_{xc} = \rho(r)\varepsilon_{xc}[\rho(r)]dr \qquad (\text{II.18})$$

$\varepsilon_{xc}[\rho(r)]$ is the exchange and correlation energy per electron at point r, it depends on ρ(r) in the vicinity of r. These approximations have aroused the interest of several scientists and recorded enormous progress in this area [13].

### II.5.1. Local Density Approximation (LDA)

The local density approximation (LDA: Local Density Approximation) is based on the assumption that the electron density varies slowly in space and therefore the terms of exchange-correlation depend only on the local value of $\rho(r)$ ; that is, it treats an inhomogeneous system as locally homogeneous.

The exchange-correlation functional $\varepsilon_{xc}[\rho(r)]$ is thus replaced by that of a homogeneous gas of electrons of density ρ(r):

$$E_{xc}^{LDA} = \int \rho(r)\varepsilon_{xc}[\rho(r)]dr \qquad (\text{II.19})$$

The exchange and correlation functional can be divided into an exchange-related term and a correlation-related term.

$$E_{xc}^{LDA}[\rho(r)] = E_{x}^{LDA}[\rho(r)] + E_{c}^{LDA}[\rho(r)] \qquad (\text{II.20})$$

With

.

$$E_x^{LDA}[\rho(r)] = -\frac{3}{4}\left(\frac{3}{4}\rho(r)\right)^{3/4} \qquad (II.21)$$

According to the Dirac exchange functional [14]

Quantum Monte Carlo calculations by Ceperley and Alder [15] have also provided accurate values of $E_x^{LDA}[\rho(r)]$ These values were then interpolated by Vosko, Wilk and Nusair (VWN) [16] and Perdew and Zunger [17] to an analytical form of $E_x^{LDA}[\rho(r)]$.

So; LDA is defined from a homogeneous gas of electrons, one would expect that it gives good results only for systems having an electronic density which varies slowly. However, the applicability of LDA goes beyond that, and it has produced good results for systems with inhomogeneous density. Experience has shown that the LDA performs better than the Hartree-Fock approximation [18].

Typically, calculations using LDA lead to excessively high binding energies. This results in too short lengths of connections, too small mesh parameters, too large incompressibility moduli.

## II.5.2. Generalized Gradient Approximation (GGA)

The generalized gradient approximation (GGA: Generalized Gradient Approximations) provides an improvement over the LDA. In the local approximation, the exchange and correlation potential only depends on the density whereas in the GGA approximation, the potential is expressed as a function of the local electron density and its gradient $\nabla\rho(r)$

$$E_{xc}^{GGA}[\rho(r)] = \int \rho(r) f[\rho(r), \nabla\rho(r)] d\rho(r) \qquad (II.22)$$

$f[\rho(r), \nabla\rho(r)]$ being the exchange and correlation function dependent on the electron density and its gradient.

Unlike the LDA, there are several versions of the GGA most frequently used;

- ✓ PBE "Perdew-Burke-Ernzerhof " [19-20].
- ✓ PBEsol "Perdew-Burke-Ernzerhof GGA reparametrized for solids" [21],
- ✓ WC "by Wu and Cohen" [22],
- ✓ AM05 functional "by Armiento and Mattsson" [23]
- ✓ HTBS functional "by Haas, Tran, Blaha, and Schwarz" [24]

So, In many cases, the GGA approximation provides better results than the LDA for total energies, cohesion energies, equilibrium volumes and incompressibility moduli. However, the

band gap widths of insulators and semiconductors remain far too low. Systems with strong correlations (bands d or narrow f) are poorly described.

### II.5.3. TB-mBJ approach

Tran and Blaha have recently published a new version of the exchange potential [25], which was proposed for the first time by Becke and Johnson [26]. It is the potential mBJ modified Becke Johnson Potentiel (also known as the potential TB: Tran-Blaha) that has been identified and implemented in the most recent version of the Wien2k code[27].

Tran and Blaha [28] tested the exchange potential proposed by Becke and Johnson (BJ) [26] which was designed to reproduce the shape of the exact exchange potential i.e. the optimized effective potential (OEP). They found that the use of the BJ potential combined with the LDA correlation potential, always gives underestimated gap energies. In order to improve these results, Tran and Blaha [25] introduced a simple modification of the original BJ potential and obtained good agreement with other more expensive approaches, because of their high self-consistency, such as the hybrid functionals (see the next section) [29] and the GW method [30-31] .The modified BJ potential (mBJ) proposed by Tran and Blaha [25] has the following form:

$$V_X^{TB-mBJ}(\vec{r}) = cV_X^{BR}(\vec{r}) + (3c-2)\frac{1}{\pi}\sqrt{\frac{5}{12}}\sqrt{\frac{2t(\vec{r})}{\rho(\vec{r})}} \qquad (II.23)$$

c was chosen to depend linearly on the square root of the average of $|\nabla\rho|/\rho$ [32]

$$c = \alpha + \beta\left(\frac{1}{V_{cell}}\int\frac{\nabla\rho(r')}{\rho(r')}d^3r'\right)^{\frac{1}{2}} \qquad (II.24)$$

$V_{cell}$ Is the unit cell volume and $\alpha$ and $\beta$ are two free parameters whose values are $\alpha$ = -0.012 and $\beta$ =1.023 bohr$^{1/2}$ according to a fit to experimental results [25].

Equation $(II.23)$ was chosen to restore the exchange potential of the LDA $V_X^{LDA}[\rho(r)] = -\left(\frac{3}{\pi}\right)^{\frac{1}{3}}(2\rho(r))^{\frac{1}{3}}$ (whatever the value of c) for a constant electron density. In addition, the Becke-Roussel (BR) potential $V_X^{BR}(r)$

$$V_x^{BR} = -\frac{1}{\left[x^3e^{-x}/(8\pi\rho)\right]^{1/3}}\left(1-e^{-x(\vec{r})}-\frac{1}{2}x(\vec{r})e^{-x(\vec{r})}\right) \qquad (II.25)$$

$x$ is determined from a nonlinear equation involving $\rho, \nabla\rho, \nabla^2\rho$.

.

$V_X^{BR}(r)$ is taken equal to the Slater potential $V_X^{Slater}(r)$ which represents the average of the Hartree-Fock potential [33] ($V_X^{BR}(r) \approx V_X^{Slater}(r)$). As a result, the BR potential reduces to 3/2 of the potential $V_X^{LDA}$ and the second term of equation (II.23) (without (3c-2)) reduces to $\frac{1}{2}V_X^{LDA}$ since to $t(r) = \left(\frac{3}{20}\right)\left(3\pi^2\right)^{\frac{2}{3}} \times \left(2\rho(r)\right)^{\frac{5}{3}}$ for a constant density.

For c=1, the original BJ potential is reproduced. By varying c for a given material, it has been found [25] that for many solids, the gap energy increases monotonically with respect to c. specifically, for solids with small gaps, and also for c.

## II.5.4. Hybrid Functional

The "hybrid" functional is based on the adiabatic connection formalism. The principle emerges from the question asking whether it is possible to use the Hartree-Fock exchange in the Kohn-Sham formalism. The formula for the adiabatic connection theoretically justifies the determination of the Hartree-Fock exchange energy from the energy of the Kohn-Sham orbital's. The use of the Hartree-Fock exchange part associated with GGA functional provides results comparable to those of the generalized gradient approximation. The first functional of this type was proposed by Becke (1993), and contains 50% of Hartree-Fock exchange; it is the "half and half"[34] functional. It had the disadvantage of containing too high a proportion of HF exchange, and the most widely used functional of this type today is the one known by the acronym B3LYP[35]. This is a three-parameter functional combining the local exchange, Becke exchange and Hartree-Fock exchange functions, with the local correlation functional of Vosko, Wilk, and Nusair (VWN) and gradient-corrected functional of Lee, Yang and Parr.

## II.5.5. The Heyd-Scuseria-Ernzerhof (HSE) functional

HSE functional are exchange-correlation functional used in density functional theory (DFT) to improve the accuracy of describing properties like band gaps and charge transfer excitations. HSE functional combine the Hartree-Fock exchange and DFT exchange-correlation functional, provides more accurate results for a variety of systems. They improve the description of short-range and long-range electron-electron interactions, but are computationally more demanding than pure DFT methods. Researchers often choose HSE functional for high accuracy in predicting electronic and structural properties, but their choice depends on specific applications and available computational resources.

.

**References**

[1] Hohenberg.P & Kohn, W. (1964). Inhomogeneous electron gas. *Physical review*, *136*(3B), B864.

[2] Thirring, W., & Urban, P. (Eds.). (2012). *The Schrödinger Equation: Proceedings of the International Symposium "50 Years Schrödinger Equation" in Vienna, 10th–12th June 1976* (Vol. 17). Springer Science & Business Media.

[3] Bethe, H. A. (1999). Quantum theory. *Reviews of Modern Physics*, *71*(2), S1.

[4] Pisana, S., Lazzeri, M., Casiraghi, C., Novoselov, K. S., Geim, A. K., Ferrari, A. C., & Mauri, F. (2007). Breakdown of the adiabatic Born–Oppenheimer approximation in graphene. *Nature materials*, *6*(3), 198-201.

[5] Hartree, D. R. (1928, January). The wave mechanics of an atom with a non-Coulomb central field. Part I. Theory and methods. In *Mathematical Proceedings of the Cambridge Philosophical Society* (Vol. 24, No. 1, pp. 89-110). Cambridge university press.

[6] Fock, V. (1930). Selfconsistent field "mit Austausch für Natrium. *Zeitschrift für Physik*, *62*, 795-805.

[7] Ludeña, E. V. (1983). Thomas–Fermi term as the simplest correction to the Weizsacker term. *International Journal of Quantum Chemistry*, *23*(1), 127-133.

[8] Fermi, E. (1928). Eine statistische Methode zur Bestimmung einiger Eigenschaften des Atoms und ihre Anwendung auf die Theorie des periodischen Systems der Elemente. *Zeitschrift für Physik*, *48*(1-2), 73-79.

[9] Hohenberg, P., & Kohn, W. (1964). Inhomogeneous electron gas. *Physical review*, *136*(3B), B864.

[10] Baerends, E. J. (2001). Perspective on "Self-consistent equations including exchange and correlation effects" Kohn W, Sham LJ (1965) Phys Rev A 140: 133–1138. *Theoretical Chemistry Accounts: New Century Issue*, 265-269.

[11] Kohn, W., & Mermin, N. D. (1965). in "Strongly Coupled Coulomb Systems," ed. by GJ Kalman, JM Rommel, and K. Blagoev, Plenum, New York, 1998, pg. 9. *Phys. Rev.*, *137*, 1441.

[12] Yang, X., Stein, E. W., Ashkenazi, S., & Wang, L. V. (2009). Nanoparticles for photoacoustic imaging. *Wiley interdisciplinary reviews: nanomedicine and nanobiotechnology*, *1*(4), 360-368

[13] Labidi.M, (2011). Etude des propriétés structurales, électroniques des quaternaires, Doctoral thesis, Badji Mokhtar University.

.

[14] Dirac, P. A. M. (1929). Quantum mechanics of many-electron systems. *Proceedings of the Royal Society of London. Series A, Containing Papers of a Mathematical and Physical Character*, *123*(792), 714-733.

[15] Ceperley, D. M., & Alder, B. J. (1980). Ground state of the electron gas by a stochastic method. *Physical review letters*, *45*(7), 566.

[16] Vosko, S. H., Wilk, L., & Nusair, M. (1980). Accurate spin-dependent electron liquid correlation energies for local spin density calculations: a critical analysis. *Canadian Journal of physics*, *58*(8), 1200-1211.

[17] Perdew, J. P., & Zunger, A. (1981). Self-interaction correction to density-functional approximations for many-electron systems. *Physical Review B*, *23*(10), 5048.

[18] Koch, W., & Holthausen, M. C. (2000). A chemist's guide to density functional theory. wileyvch, verlag gmbh.

[19] Perdew, J. P., Chevary, J. A., Vosko, S. H., Jackson, K. A., Pederson, M. R., Singh, D. J., & Fiolhais, C. (1992). Atoms, molecules, solids, and surfaces: Applications of the generalized gradient approximation for exchange and correlation. *Physical review B*, *46*(11), 6671.

[20] Perdew, J. P., Burke, K., & Ernzerhof, M. (1996). Generalized gradient approximation made simple. *Physical review letters*, *77*(18), 3865.

[21] Perdew, J. P., Ruzsinszky, A., Csonka, G. I., Vydrov, O. A., Scuseria, G. E., Constantin, L. A.& Burke, K. (2008). Restoring the density-gradient expansion for exchange in solids and surfaces. *Physical review letters*, *100*(13), 136406.

[22] Wu, Z., & Cohen, R. E. (2006). More accurate generalized gradient approximation for solids. Physical Review B, 73(23), 235116.

[23] Armiento, R., & Mattsson, A. E. (2005). Functional designed to include surface effects in self-consistent density functional theory. *Physical Review B*, *72*(8), 085108.

[24] P, Tran, F. Blaha, P., & Schwarz, K. (2011). Construction of an optimal GGA functional for molecules and solids. *Physical Review B*, *83*(20), 205117.

[25] Tran, F., & Blaha, P. (2009). Accurate band gaps of semiconductors and insulators with a semilocal exchange-correlation potential. *Physical review letters*, *102*(22), 226401.

[26] Becke, A. D., & Johnson, E. R. (2006). A simple effective potential for exchange. The Journal of chemical physics, 124(22), 221101.

[27] Blaha, P., Schwarz, K., Madsen, G. K., Kvasnicka, D., & Luitz, J. (2001). wien2k. An augmented plane wave+ local orbitals program for calculating crystal properties, 60, 1-302.

.

[28] Tran, F., Blaha, P., & Schwarz, K. (2007). Band gap calculations with Becke–Johnson exchange potential. *Journal of Physics: Condensed Matter*, *19*(19), 196208.

[29] Heyd, J., Peralta, J. E., Scuseria, G. E., & Martin, R. L. (2005). Energy band gaps and lattice parameters evaluated with the Heyd-Scuseria-Ernzerhof screened hybrid functional. *The Journal of chemical physics*, *123*(17), 174101.

[30] Aulbur, W. G., Städele, M., & Görling, A. (2000). Exact-exchange-based quasiparticle calculations. *Physical Review B*, *62*(11), 7121.

[31] Shishkin, M., Marsman, M., & Kresse, G. (2007). Accurate quasiparticle spectra from self-consistent GW calculations with vertex corrections. *Physical review letters*, *99*(24), 246403.

[32] Becke, A. D., & Roussel, M. R. (1989). Exchange holes in inhomogeneous systems: A coordinate-space model. *Physical Review A*, *39*(8), 3761.

[33] Slater, J. C. (1951). A simplification of the Hartree-Fock method. *Physical review*, *81*(3), 385.

[34] Reed, A. E., Weinstock, R. B., & Weinhold, F. (1985). Natural population analysis. The Journal of Chemical Physics, 83(2), 735-746.

[35] Adamo, C., & Barone, V. (1999). Toward reliable density functional methods without adjustable parameters: The PBE0 model. *The Journal of chemical physics*, *110*(13), 6158-6170.

# CHAPTER III

# CLASSES OF POTENTIALS

## Chapter III: Classes of Potentials



There are two major classes of potentials:

- ✓ Pseudo potentials.
- ✓ All-electron potentials: Muffin-tin or Full Potential.

## III.1. Planes waves and pseudopotential method

### III.1.1.Bloch's theorem and plane waves

For an assumed infinite periodic solid, the chosen plane wave basis must satisfy the periodicity conditions of the crystal. The electron wave function can be written in the form of a Bloch function as the product of a plane wave and a function of the reciprocal lattice $u_n$ (***k***, ***r***) according to the equation [1-2]:

$$\Psi_{n,K_i}(r) = e^{iK_i r} u_{n,K_i}(r) \qquad (III.1)$$

With:

r : vector in real space

k: wave vector of the reciprocal lattice

Ω: volume of the elementary mesh in reciprocal space.

n: index of the energy band.

The function $u_k(r)$ must satisfy Bloch's theorem, hence it must be periodic and have the same period of the crystal lattice.

$$u_k(r+R_l) = u_k(r) \qquad (III.2)$$

$R_l$ ; is the direct mesh vector.

To deal with an infinite number of electrons one must then express the wave function in terms of an infinite number of reciprocal vectors k in the first Brillouin zone [3-4]. The electron wave functions of the k points in the Brillouin zone are expressed in terms of a discrete basis of plane waves described by an infinite Fourier series according to the equation:

$$\Psi_{n,K}(r) = \frac{1}{\sqrt{\Omega}} \sum C_{n,K}(G) e^{i\left(\vec{K}+\vec{G}\right)\vec{r}} \qquad (III.3)$$

Where G is the vector of the reciprocal network.

For practical reasons, the plane wave basis must be finite to contain a finite number of plane waves, this is done by a cut-off energy threshold (Energy Cut-off ) Ecut which represents the maximum kinetic energy of cut-off limiting the development order of the electronic wave function.

A constraint is placed by this parameter (Ecut-off) on the plane waves. The plane waves belonging to the sphere of radius $r_c = E_{cut}$ must obey the following condition:

$$\frac{\hbar^2}{2m}|K+G| \leq E_{cutoff} \qquad (III.4)$$

The kinetic energy cut-off depends on the system studied and particularly on the choice of the pseudo-potential describing the potential felt by the valence electrons. If the energy cut-off is low, the number of plane waves is not sufficient to represent well the wave functions and the charge density, which induces an error on the estimation of the total energy

of the system. We will therefore need to increase the cutoff radius until the convergence is achieved [5].

The choice of a plane wave base has some advantages such as:

- It simplifies the evaluation of derivatives and integrals, leading to an easy calculation of the elements of the Hamiltonian matrix.
- The passage between the direct space and the reciprocal space or conversely is done by taking advantage of the fast Fourier transform FFT.
- The plane waves form a complete and orthonormal set, independent of the atomic positions. [6].

The most widely used sampling method is the one proposed by Monkhorst and Pack [7] which provides a uniform k-point grid of chosen dimension.

## III.1.2.Pseudopotential method

The pseudo potential approximation is very useful in the study of the physical properties of condensed matter. The method consists in replacing the core electrons of an atom by a fictitious potential that represents as well as possible the atom near its nucleus. It is very good, since the electronic states very close to the atomic nuclei have little effect on the electrons of the neighboring atoms, since they do not contribute to the chemical and physical interactions between atoms [8.9]. Only the valence electrons play a significant role in the physical properties of materials. This method is also compatible with the DFT formalism and the plane wave basis.

Pseudopotentials are divided into two categories according to the basis used to develop the pseudo-functions:

- norm-conserving methods (norm-conserving pseudopotentials introduced by Hamman et al. [10] ).
- The methods of non conservation of the norm (the ultra-soft pseudopotentials introduced by Vanderbilt [11]).

## III.1.2.a. Pseudopotentials with conserved norms

Pseudopotentials with conserved norms are pseudopotentials that promote transferability. These conditions were formulated by Hammann, $chlùter and Chiang (1979) and then reformulated by Bachelet, Hammann and Schifiter BHS (1982) [10] Another method was proposed by Trouiller-Martins. This method is a norm-conserving BHS method where additional constraints are imposed on the pseudo wave function. The radial part of the pseudo wave function (associated with the pseudopotential) verifies the following equalities;

$$R^{ps}(r) = r^{L+l} e^{p(r)} \qquad r \leq r_c$$

$$R^{ps}(r) = R(r) \qquad r \geq r_c \qquad (III.5)$$

Where P(r) is a polynomial of order 6 in $r^2$ of the form:

$$P(r) = c_0 + c_2 r^2 + c_4 r^4 + c_6 r^6 + c_8 r^8 + c_{12} r^{12} \qquad (III.6)$$

The pseudo wave function is the solution of the Schrödinger equation. It verifies the condition of the conservation of the norm which determines the coefficients $c_n$ of the equation, the equality of the valence wave functions and of the pseudo wave functions at the point $r= r_c$, as well as their four first derivatives, and finally the cancellation of the first derivative of the pseudo wave functions for r=0.

The Trouiller-Martins method gives very similar results to the BHS method. The main difference is that in the Hammann method the cut-off radii are smaller and the pseudo-wave function approaches the valence wave function exponentially beyond r; on the other hand the equality is strict in the Trouiller-Martins method [12]. For this reason, the Trouiller-Martins approach allows to obtain smoother pseudopotentials for 2p, 3d, 4d, 5d electrons, which gives it an advantage for the study of elements with localized orbitals.

**III.1.2.b. Ultra-soft pseudo-potential.**

The ultra-soft pseudo-potential means that the development of valence wave pseudo-functions must be done using few plane waves. The pseudo-potential was proposed by Vanderbilt [11], their main advantages, compared to those with conserved norms, are a much faster convergence with a lower number of plane waves and thus a lower energy of cutoff equation $(III.4)$. On the other hand, their construction is more complex and their use in a numerical computation code requires additional routines and thus an increased programming time and complexity.

## III.1.3. Generation of pseudo-potential

The generation of a pseudo potential is done in two steps:

- Firstly an "all-electron" calculation of the atom alone in a reference atomic configuration, usually the ground state.

- Secondly the pseudization of the "all-electron" wave functions obtained, in order to generate the parameters of the pseudopotential. During this last process, a number of conditions are verified :

-The energies of the "all-electron" and "pseudo-electron" eigenstates are equal;

-The "all-electron" and "pseudo-electron" wave functions are identical beyond the cut-off radius $r_c$ ;

-The logarithmic derivatives of the "all-electron" and "pseudo-electron" wave functions calculated in rc are equal for the state energies.

**Procedure of calculation**

The "all-electron" calculation is performed in the DFT formalism, using an exchange-correlation functional (LDA or GGA), and in a relativistic way [13] or not. The calculation being centrally symmetric, the resolution is done on a radial grid. It is therefore necessary to specify several parameters for this part:

- The atomic number of the atom.
- The exchange-correlation functional must be in agreement with the calculation made afterwards.
- The relativistic effects on the core electrons can be taken into account, and this is done when generating the pseudo-potential.
- The accuracy of the radial grid, gives the accuracy of the calculation, but has little impact on the speed of the pseudopotential.
- The electronic configuration reference is in general the unpolarized ground state.

In summary, this method introduces as the only approximation that the atomic environment does not influence the core electrons. This is called the frozen core approximation. This approximation can cause significant errors in the case of energy calculations with extraction of a core electron. Even if it is possible from the APW formalism to take into account the relaxation of core electrons, as shown by M. Marsman in 2006 [14].

## III.1.4. Presentation of the CASTEP code

The CASTEP software (Cambridge Serial Total Energy Package) developed by the Condensed Matter Group at the University of Cambridge U.K. in 1988 by Payne et al [15-2]. It is a program that uses density functional theory (DFT) to simulate properties, interfaces and surfaces for a wide range of material classes. Based on the Pseudo-potential, plane wave, total energy methods, CASTEP uses the number and type of atoms in the system and the

periodic properties to predict lattice constants, molecular geometry, structural properties, band structure, density of state, charge density, wave functions and optical properties [16]……. etc.

## III.2. Full Potential-Linearized Augmented Plane Wave (FP-LAPW) method

### III.2.1. Introduction

Among the various methods for calculating the electronic band structure of materials, we find the linearized augmented plane wave method (FP-LAPW). The augmented plane wave (APW) method, developed in 1937 by Slater [17-18], and after several modifications established by Anderson [20], becomes the linearly augmented plane wave method (FP-LAPW)). To describe the crystal potential, Slater introduces the Muffin-tin potential approximation Figure III.1. Inside the spheres, spherical shaped potentials are used against a flat (constant) potential outside, in the outer (interstitial) region Figure III.2: Thus the potential is written as:

$$U(r)=\begin{cases} U(r) & \text{for } r \le r_s \\ 0 & \text{for } r > r_s \end{cases} \text{ With } r=|\vec{r}| \qquad (III.7)$$

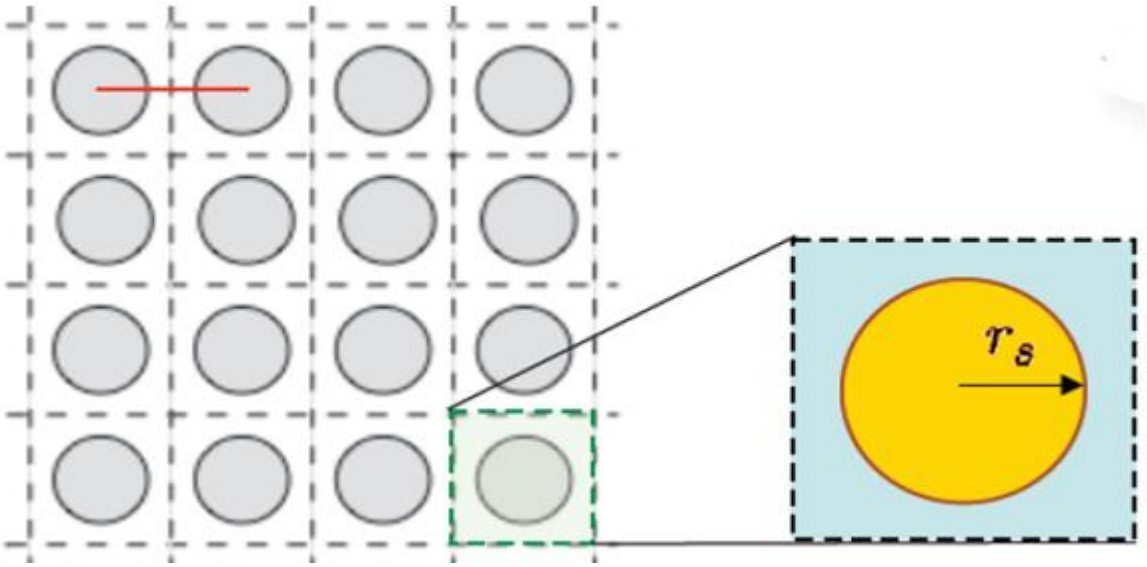


**Figure III.1**: The Muffin-tin potential approximation.

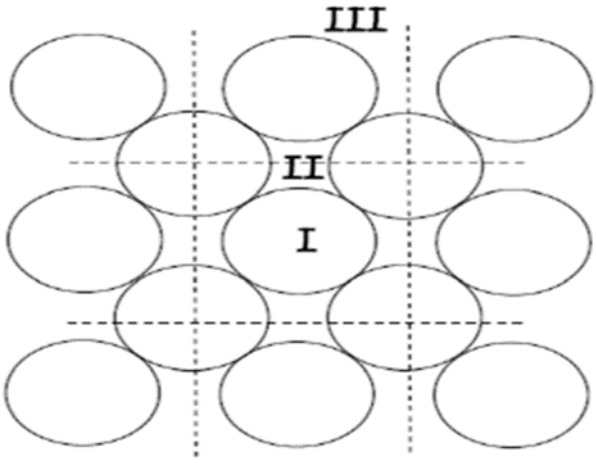


I: Region of the spheres
II: Interstitial region
III : Region of the void

**Figure III.2:** Computational regions of the Muffin-tin potential approximation.

## III.2.2. The APW method

The APW method was developed by Slater in 1937 [17-18]. Near an atomic nucleus, the potential and wave functions are similar to those of an atom they vary strongly but almost spherically. Conversely, in the interstitial space between atoms, the potential and wave functions are more fluid. Consequently, the space is divided into two regions and different basic extensions are used in these regions:

- Radial solutions of Schrodinger equation inside centered spheres of non-overlapping atoms.
- Planar waves in the other interstitial regions Figure III.3.

The previous paragraph can be translated by the following mathematical formula:

$$\Phi\left(\vec{\mathrm{r}}\right)=\begin{cases}\frac{1}{\sqrt{\Omega}}\sum_G C_G e^{i\left(\vec{G}+\vec{K}\right)\vec{r}} & r>r_0\\ \sum_{lm}\mathrm{A}_{lm}U_l\left(\vec{r}\right)Y_{lm}\left(\vec{r}\right) & r<r_0\end{cases} \qquad (\text{III.8})$$

Where $\Omega$ presents the volume of the cell, $Y_{lm}$ the spherical harmonics and $C_G$ presents the coefficients of its development.

The function $U_l\left(\vec{r}\right)$ is a regular solution of the Schrödinger equation for the radial part which is written in the form:

$$\left\{-\frac{d^2}{dr^2}+\frac{l(l+1)}{r^2}+V\left(\vec{r}\right)-E_l\right\}rU_l\left(\vec{r}\right)=0 \qquad (\text{III.9})$$

Where $E_l$ are the linearization energy and $V(\vec{r})$ the spherical component of the Muffin potential in the sphere.

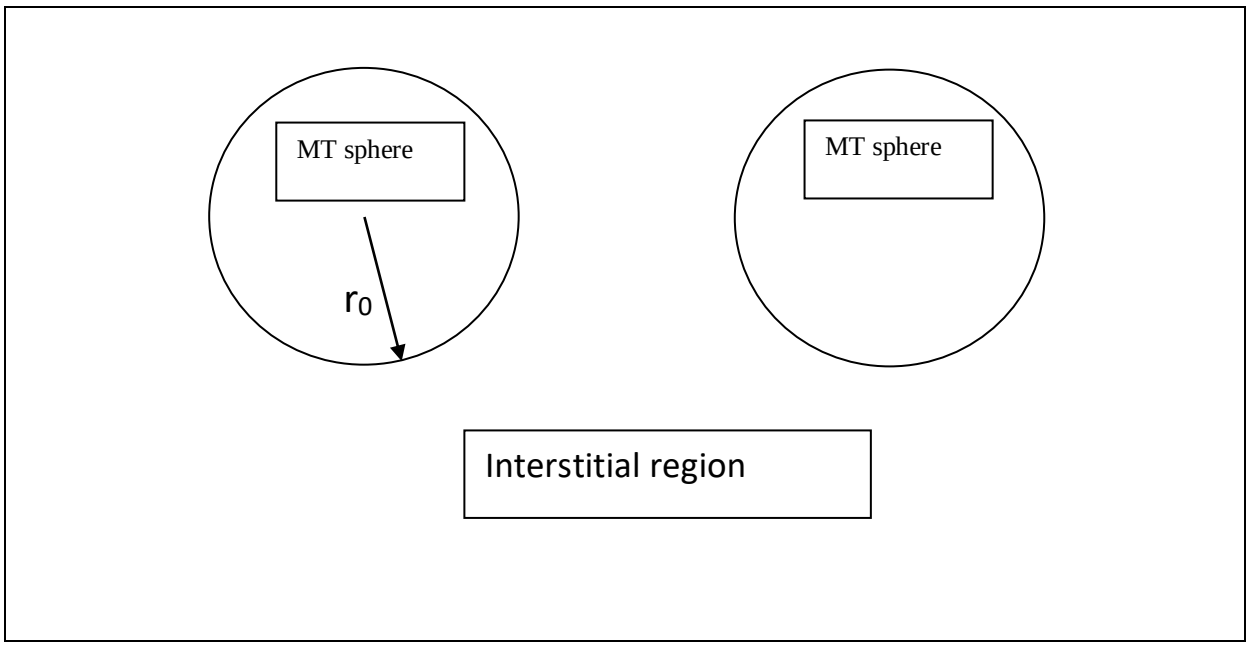


**Figure III.3:** Diagram of the distribution of the elementary mesh into atomic spheres and interstitial region.

$$A_{lm} = \frac{4\pi i^l}{\frac{1}{\Omega^2} U_l(r)} \sum_G C_G j_l\left(\left|\vec{K}+\vec{G}\right| r_0\right) Y_{lm}^*\left(\vec{K}+\vec{G}\right) \qquad (\text{III.10})$$

Where $j_l$ is the Bessel function.

The function $U_l(\vec{r})$ in equation $(\text{III.9})$ is dependent on the linearization energy, and can become zero at the surface of the MT sphere. So this observation leads to the separation between radial and plane wave functions. This remark is considered as a complication. To overcome this problem, several modifications have been made to the APW method, including those proposed by Andersen and by Koelling [19-20]. The rectification consists in representing the wave function $\Phi(\vec{r})$ inside the sphere by a linear combination of radial function $U_l(\vec{r})Y_{lm}(\vec{r})$ and their derivative $\dot{U}_l(\vec{r})Y_{lm}(\vec{r})$ with respect to the energy [20]. This was mentioned earlier, and leds to the FP-LAPW method.

## III.2.3.The FP-LAPW method

For a crystal, the space is divided into two regions:

- The Muffin- Tin spherical region
- The remaining space, which represents the interstitial region.

The basic function of the method (FP-LAPW) has plane waves in the interstitial region and harmonic spherical in the spheres. The basic functions inside the sphere are linear combinations of the radial functions $U_l\left(\vec{r}\right)Y_{lm}\left(\vec{r}\right)$ and their derivatives $\dot{U}_l\left(\vec{r}\right)Y_{lm}\left(\vec{r}\right)$ with respect relative to energy.

The function satisfies the following equation:

$$\left(-\frac{\hbar^2}{2m}\frac{d^2}{dr^2}+\frac{\hbar^2}{2m}\frac{l(l+1)}{r^2}+V\left(\vec{r}\right)-E_l\right)r\dot{U}_l\left(\vec{r}\right)=rU_l\left(\vec{r}\right) \qquad \text{(III.11)}$$

So ; Les fonctions sont définies exactement comme dans la méthode APW mais avec un fixe

where the combination of radial functions $U_l$ and $\dot{U}_l$ ensures continuity with the wave plane of the interstitial region on the surface of the MT sphere.

The augmented wave functions are then used as the basis functions of the FP-LAPW method [22], so we have:

$$\Phi\left(\vec{\mathrm{r}}\right)=\begin{cases}\dfrac{1}{\Omega^{1/2}}\sum_G C_G e^{i\left(\vec{G}+\vec{K}\right)\vec{r}} & r>r_0\\ \sum_{lm}\left[\mathrm{A}_{lm}U_l\left(\vec{r}\right)Y_{lm}\left(\vec{r}\right)+B_{lm}\dot{U}_l\left(\vec{r}\right)\right]Y_{lm}\left(\vec{r}\right) & r<r_0\end{cases} \qquad \text{(III.12)}$$

where: $\mathrm{A}_{lm}$ are coefficients corresponding to the function $U_l\left(\vec{r}\right)$ .

where: $B_{lm}$ are coefficients corresponding to the function $\dot{U}_l\left(\vec{r}\right)$ .

## III.2.4. The LAPW method

The linearized augmented plane wave (LAPW) method is an improvement of the APW method. This method uses a mixed basis, which is more efficient than a plane wave basis. However, it brings additional complications that make the calculation of the elements of the coefficient matrix more difficult.

Inside the spheres, the LAPW functions are a better fit than the APW functions, in fact if $E_l$ differs a bit from the band energy E, the obtained results of the linear combination of the reproduce radial function are better than the APW functions taken alone:

$$U_l\left(E,\vec{r}\right)=U_l\left(E_l,\vec{r}\right)+\left(E-E_l\right)\dot{U}_l\left(E_l,\vec{r}\right)+O\left(\left(E-E_l\right)^2\right) \qquad \text{(III.13)}$$

Where $O\left(\left(E-E_l\right)^2\right)$ is the squared error in energy.

In this method, the calculations lose some accuracy compared to the APW method whose wave functions are more correct. The FP-LAPW method causes an error $O\left(E-E_l\right)^2$ on the wave functions and another on the band energy of order $O\left(E-E_l\right)^4$. Despite these minor drawbacks, the LAPW functions are a good basis -with a single $E_l$- to obtain all the valence bands in a rather large energy range. However, it is possible to divide the energy range into several energy windows, each corresponding to an $E_l$-energy where the solution will be obtained separately [21].

## III.2.5. The LAPW+LO method

The development of the LAPW method in local orbitals (**LO**) consists in modifying the orbitals of its basis to avoid the use of several windows, by using a third category of basic functions. The principle is to treat all the bands from a single energy window [22-23]. Singh [24] gave these orbitals, as a linear combination of two radial functions corresponding to two different functions.

$$\Phi\left(r\right)=\begin{cases}0 & r>r_0\\ \left[A_{lm}U\left(r,E_l\right)+B_{lm}U_l\left(r,E_l\right)+ClmU_l\left(r,E_l\right)\right]Y_{lm}\left(r\right) & r<r_0\end{cases} \qquad \text{(III.14)}$$

Where the coefficients *Clm* are of the same nature as the coefficients $A_{lm}$ and $B_{lm}$ defined previously. A local orbital is defined for a given *l*, m and for a given atom (in the unit cell, all atoms being considered and not only the in equivalent atoms). This improvement of the LAPW method is at the origin of the success of the linearization method based on the LAPW method insofar as it allows the extension of this original method to a much larger class of compounds.

## III.2.6. The APW+lo method

The problem encountered in the APW method consists in the energy dependence of the set of basic functions. This dependence could be eliminated in the LAPW+LO method but at the cost of a larger basis size, and thus both APW and LAPW+LO methods acquire a significant limitation. Sjösted, Nordström and Singh [24-25] made an improvement by realizing a basis that combines the advantages of the APW method with those of the LAPW+LO method. This method is called "APW+lo" and corresponds to an energy-independent basis (as was the LAPW+LO method) that requires only a very small amount of plane-wave cutoff energy compared to that required in the APW method. It consists in using a standard APW basis but considering U(r) for a fixed energy $E_l$ in order to keep the advantage brought by the linearization of the eigenvalue problem. However, a fixed energy basis does not provide a satisfactory description of the eigenfunctions, local orbitals are also added to ensure variation flexibility in the radial basis functions. An "APW+lo" basis is defined by combining the following two types of wave functions:

- APW plane waves with a set of energies $E_l$.
- Local orbitals differ from those in the LAPW+LO method defined by:

$$\Phi(r)=\begin{cases}0 & r>r_0\\ \sum lm\left[A_{lm}U(r,E_l)+B_{lm}U_l(r,E_l)\right]Y_{lm}(r) & r<r_0\end{cases}$$

(III.15)

## III.2.7. The mixed base LAPW/APW+lo

In the calculation, a mixed LAPW and APW+lo basis can be used for different atoms and even for different values of the *l* number. In general, slowly converging orbitals (like the 3d states of transition metals), or atoms with a small sphere size are described with the APW+lo basis and the rest with a LAPW [25].

## III.2.8. Presentation of the Wien2k code

In this work, we used the FP-LAPW method, as implemented in the Wien2k code. The Wien2k code [26] consists of a set of programs developed by Blaha and his collaborators at the Institute of Materials Chemistry at the Technical University of Vienna [27]. It consists of different independent programs (see figure III.4) which are linked by a C script. Shell:

**NN**: This is a program that gives the distances between nearest neighbors, which helps to determine the atomic radius of the sphere.

**SGROUP**: calculates the symmetry points and the space group of the introduced structure.

**SYMMETRY**: It generates the space group symmetry operations, determines the point group of individual atomic sites, generates the LM expansion for the lattice harmonics and determines the local rotation matrices.

**INSTGEN LAPW**: allows to define the spin polarization of each atom is very important for polarized spin calculations and in particular for antiferromagnetic cases; where it is required to invert the spin of AFM atoms and/or to fix the spin of non-magnetic atoms.

**LSTART**: A program that generates atomic densities and determines how different orbitals are treated in the band structure calculation, such as valence or core states with or without local orbital's

**KGEN:** It generates a k mesh in the Brillouin zone.

**DSTART**: It generates a starting density for the SCF cycle by superimposing the atomic densities generated in **LSTART**.

- ✓ Then a consistent self cycle is initialized and repeated until the convergence criterion is verified. This cycle consists of the following steps:

**LAPW0**: Generates the potential for density.

**LAPW1**: Compute valence bands, eigenvalues and eigenvectors.

**LAPW2**: Compute the valence densities for the eigenvectors.

**LCORE**: Calculates core states and densities.

**MIXER**: Mixes the input and output densities.

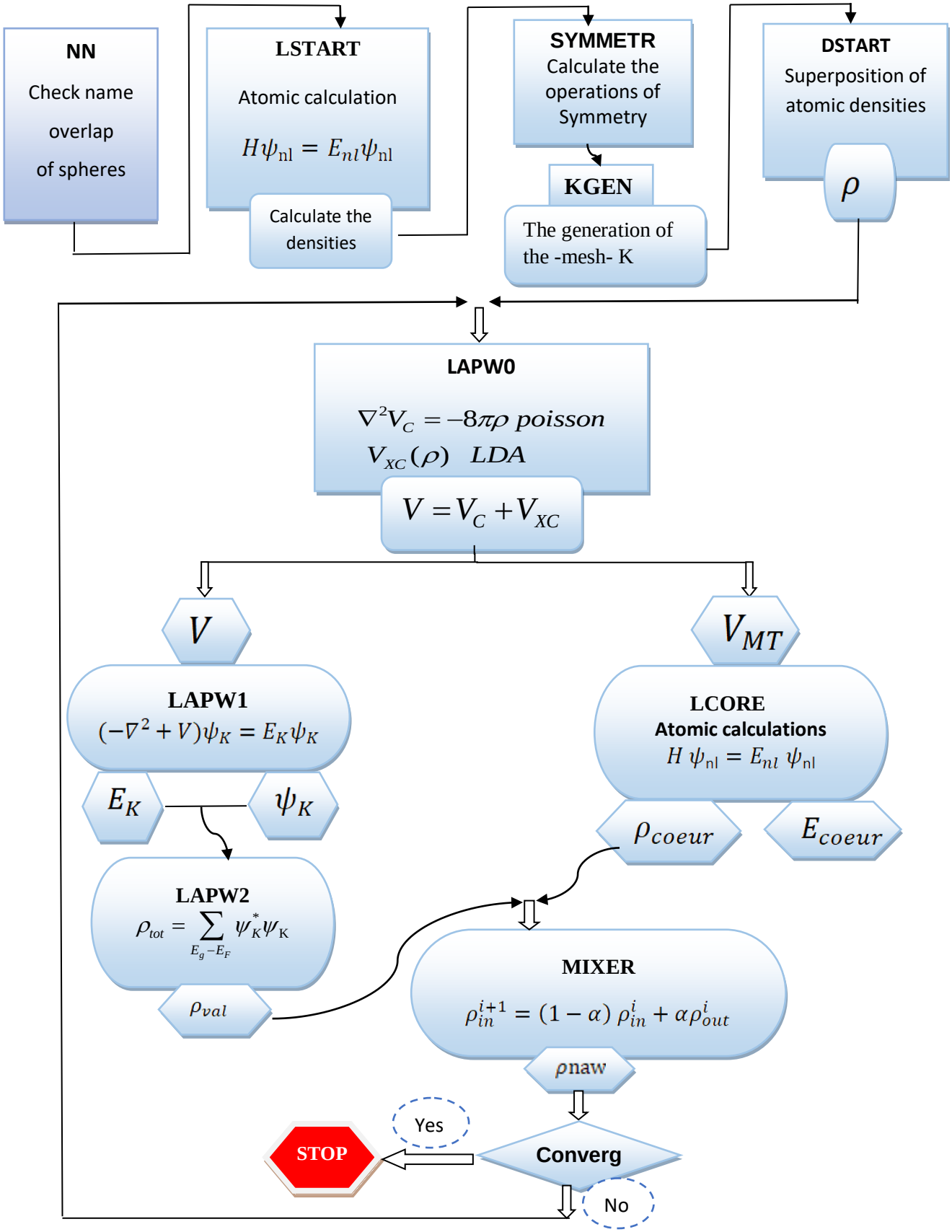


**Figure III.4:** The flowchart of the Wien2k code programs.

**References**

[1] Bloch, F. (1929). Über die quantenmechanik der elektronen in kristallgittern. Zeitschrift für physik, 52(7-8), 555-600.
[2] Payne, M. C., Teter, M. P., Allan, D. C., Arias, T. A., & Joannopoulos, A. J. (1992). Iterative minimization techniques for ab initio total-energy calculations: molecular dynamics and conjugate gradients. Reviews of modern physics, 64(4), 1045.
[3] Bouckaert, L. P., Smoluchowski, R., & Wigner, E. (1936). Theory of Brillouin zones and symmetry properties of wave functions in crystals. Physical Review, 50(1), 58.
[4] Chadi, D. J., & Cohen, M. L. (1973). Special points in the Brillouin zone. Physical Review B, 8(12), 5747.
[5] Sholl, D. S., & Steckel, J. A. (2009). Density functional theory: a practical introduction. John Wiley & Sons.
[6] Engel, G. E., & Pickett, W. E. (1998). Density Functionals for Energies and Eigenvalues: Local Mass Approximation. Electronic Density Functional Theory: Recent Progress and New Directions, 299-309.
[7] Monkhorst, H. J., & Pack, J. D. (1976). Special points for Brillouin-zone integrations. Physical review B, 13(12), 5188.
[8] Martin, R. M. (2020). Electronic structure: basic theory and practical methods. Cambridge university press.
[9] Pickett, W. E. (1989). Pseudopotential methods in condensed matter applications. Computer Physics Reports, 9(3), 115-197.
[10] Hamann, D. R., Schlüter, M., & Chiang, C. (1979). Norm-conserving pseudopotentials. Physical Review Letters, 43(20), 1494
[11] Vanderbilt, D. (1990). Soft self-consistent pseudopotentials in a generalized eigenvalue formalism. Physical review B, 41(11), 7892.
[12] Troullier, N., & Martins, J. L. (1991). Efficient pseudopotentials for plane-wave calculations. Physical review B, 43(3), 1993.
[13] Sürgers, C., Potzger, K., Strache, T., Möller, W., Fischer, G., Joshi, N., & v. Löhneysen, H. (2008). Magnetic order by C-ion implantation into $Mn_5Si_3$ and $Mn_5Ge_3$ and its lateral modification. Applied Physics Letters, 93(6), 062503.
[14] Marsman, M., & Kresse, G. (2006). Relaxed core projector-augmented-wave method. The Journal of chemical physics, 125(10), 104101.
[15] Clark, S. J., Segall, M. D., Pickard, C. J., Hasnip, P. J., Probert, M. I., Refson, K., & Payne, M. C. (2005). First principles methods using CASTEP. Zeitschrift für kristallographie-crystalline materials, 220 (5-6), 567-570..
[16] Badaut, V. (2010). Approche Couplée Chimique, Spectroscopique Et De Modélisation Ab Initio À La Réactivité De Surface : Application À La Rétention Des Anions Par La Sidérite [Doctoral dissertation].
[17] Slater, J. C. (1937). Wave functions in a periodic potential. *Physical Review*, *51*(10), 846.
[18] Slater, J. C. (1953). An augmented plane wave method for the periodic potential problem. *Physical Review*, *92*(3), 603.
[19] Andersen, O. K. (1975). Linear methods in band theory. *Physical Review B*, *12*(8), 3060.
[20] Koelling, D. D., & Arbman, G. O. (1975). Use of energy derivative of the radial solution in an augmented plane wave method: application to copper. *Journal of Physics F: Metal Physics*, *5*(11), 2041.
[21] Mattheiss, L. F., & Hamann, D. R. (1986). Linear augmented-plane-wave calculation of the structural properties of bulk Cr, Mo, and W. *Physical Review B*, *33*(2), 823.
[22] Takeda, T., & Kubler, J. (1979). Linear augmented plane wave method for self-consistent calculations. *Journal of Physics F: Metal Physics*, *9*(4), 661.

[23] Petrů, J., & Smrčka, L. (1985). Quadratic augmented plane wave method for self-consistent band structure calculations. *Czechoslovak Journal of Physics B*, *35*(1), 62-71.
[24] Singh, D. (1991). Ground-state properties of lanthanum: Treatment of extended-core states. *Physical Review B*, *43*(8), 6388.
[25] Sjöstedt, E., Nordström, L., & Singh, D. J. (2000). An alternative way of linearizing the augmented plane-wave method. Solid state communications, 114(1), 15-20.
[26] Blaha, P., Schwarz, K., Madsen, G. K., Kvasnicka, D., & Luitz, J. (2001). wien2k. *An augmented plane wave+ local orbitals program for calculating crystal properties*, *60*, 1-302.
[27] Blaha, P., Schwarz, K., & Luitz, J. (1997). WIEN97 Technical University of Vienna. Improved and updated UNIX version of the original copyright WIEN code.

# CHAPTER IV

# RESULTS AND DISCUSSIONS

## Chapter IV: Results and Discussions

## IV.1. Methodology

All ab initio computations were executed employing two complementary codes within density functional theory (DFT). Structural optimization and elastic constants are proceeded through the pseudo-potential plane-wave (PP-PW) process as incorporated in the Cambridge Serial Total Energy Package (CASTEP) of Materials Studio [1]. The generalized gradient approximation in the scheme of Perdew et al., also recognized as GGA-PBEsol [2] are adopted to estimate the exchange–correlation effects. The GGA-PBEsol functional has been specially developed to enhance the exchange-correlation potential accuracy in solids. Vanderbilt-type ultra-soft pseudo-potential [3] was used to simulate the potential visible by the electrons of valence due to the frozen-core electrons and the nucleus. The following electron states: Sr -$4s^2$ $4p^6$ $5s^2$, Ca- $3s^2$ $3p^6$ $4s^2$, Ge-$4s^2$ $4p^2$, Si-$3s^3$ $3p^2$ and N-$2s^2$ $2p^3$ are delighted as valence states. A plane-wave cut-off energy of 450 eV and Monkhorst-Pack scheme [4] with 9 × 9 × 3 k-point mesh to specimen the Brillouin zone (BZ) are chosen to guarantee a total energy convergence of $5 \times 10^{-6}$ eV/atom.

## IV.2. Structural properties

The title compounds adopt a monoclinic crystal structure and belong to space group *C*2/*c* (N◦:15), which has four unit formula per unit cell (Z = 4) [5-6]. These materials' crystal structure have the ability to be characterized as two edge-sharing $(Si/Ge)_2N_6$ tetrahedron surrounded by (Ca/Sr) atoms. A ball-and-stick representation of $Ca_5Si_2N_6$ and $Sr_5Ge_2N_6$ conventional unit cell is displayed in Fig. 1. Full geometry optimization were obtained via the Broyden–Fletcher– Goldfarb–Shanno (BFGS) algorithm [7] that is known as the faster path to detect the low-energy structure. Geometrical relaxations are executed with the convergence criteria: (i) overall energy tolerance of $5 \times 10^{-7}$ eV/atom, (ii) extreme ionic Hellmann–Feynman force, of 0.01 eV/Å, (iii) maximum atomic displacement of $5 \times 10^{-4}$Å and (iv) higher allowed stress of 0.02. GPa.

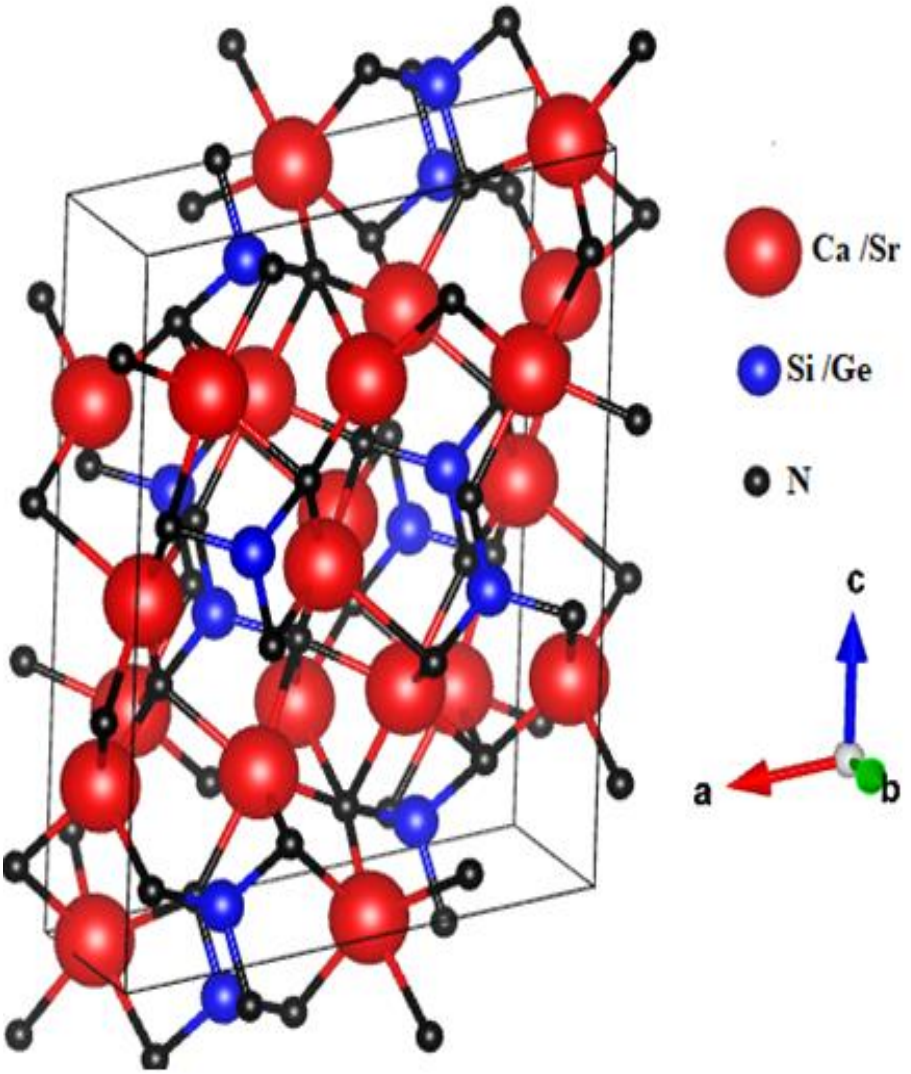


**Figure IV.1**: Conventional unit cell of $Ca_5Si_2N_6$ and $Sr_5Ge_2N_6$.

### IV.2.1. Structural parameters of the ground state

As a first step towards the prediction of the physical properties of the $Ca_5Si_2N_6$ and $Sr_5Ge_2N_6$ materials, the structural parameters were optimized at ambient pressure using the parameters mentioned previously. The initial structural data were taken from the reference [5-6]. The calculated structural parameters (a, b, c, β ° and V) of $Ca_5Si_2N_6$ and $Sr_5Ge_2N_6$ are summarized in Table IV.1, along with the available experimental data for comparison. For both compounds, it is found that the calculated and experimental lattice parameters coincide very well. The maximum deviation was calculated using the following formula:

$$d(\%)=\left(\left|\text{Calculated value-Measured value}\right|*100\right)/(\text{ Measured value})$$

The calculated lattice parameters deviate from experimental ones by about 0.8%. However, it should be noted that the equilibrium volumes of $Ca_5Si_2N_6$ and $Sr_5Ge_2N_6$ were underestimated

by about 2.3% and 1% respectively. Substitution of Ca and Si by heavier atoms (Sr and Ge respectively) leads to an increase in the equilibrium volume of about 18% from 729.83 Å$^3$ for $Ca_5Si_2N_6$ to 896.33 Å$^3$ for $Sr_5Ge_2N_6$, the latter being due to the larger ionic radii. The trend of increasing cell volume V in the examined crystals is consistent with the corresponding lattice expansion (a, b and c).

**Table IV.1:** Calculated lattice constants (*a*, *b* and *c* in Å), angle between *a* and *c* axes ($\beta$ in °), unit-cell volume V (in Å$^3$) compared with existing work, for the ternary nitrides $Ca_5Si_2N_6$ and $Sr_5Ge_2N_6$.

| | | ***a*** | **b** | ***c*** | ***β*** | **V** |
|---|---|---|---|---|---|---|
| **$Ca_5Si_2N_6$** | Present work | 9.759 | 6.004 | 12.657 | 100.27 | 729.83 |
| | Expt.[21] | 9.836 | 6.052 | 12.757 | 100.20 | 747.40 |
| **$Sr_5Ge_2N_6$** | Present work | 10.342 | 6.530 | 13.486 | 100.27 | 896.33 |
| | Expt.[22] | 10.408 | 6.521 | 13.565 | 100.29 | 905.80 |

### IV.2.2. Equation of state of $Ca_5Si_2N_6$ and $Sr_5Ge_2N_6$

The variations of the total energy of $Ca_5Si_2N_6$ and $Sr_5Ge_2N_6$ as a function of their volumes are shown in Figure IV.2. In order to determine the bulk modulus $B_0$ and its first pressure derivative $B_0^{'}$ of the two compounds at equilibrium, the E(V) diagrams were fitted by the third order of Birch-Murnaghan equation of state (EOS) given by the following expressions:

$$E(V) = E_0 + \frac{9V_0B_0}{16}\left\{\left[\left(\frac{V_0}{V}\right)^{\frac{2}{3}} - 1\right]^3 B_0^{'} + \left[\left(\frac{V_0}{V}\right)^{\frac{2}{3}} - 1\right]^2\left[6 - 4\left(\frac{V_0}{V}\right)^{\frac{2}{3}}\right]\right\} \qquad (IV.1)$$

The values of $E_0, V_0, B_0$ and $B_0^{'}$, obtained by the GGA -PBEsol approximation, are given in Table IV.2. We found that the bulk modulus $B_0$ of $Ca_5Si_2N_6$ is higher than that of $Sr_5Ge_2N_6$ confirming that the bulk modulus is inversely proportional to the volume $\left[B_0(Ca_5Si_2N_6) > B_0(Sr_5Ge_2N_6)\right.$ and $\left. V_0(Ca_5Si_2N_6) < V_0(Sr_5Ge_2N_6)\right]$.

The calculated bulk moduli using the EOS are used to check the consistency and reliability of the present calculations by comparing them with their corresponding ones, which will be calculated later from the elastic constants.

**Table IV.2:** Total equilibrium energy $E_0$, equilibrium volume $V_0$, bulk modulus $B_0$ and its first pressure derivative $B_0'$ for $Ca_5Si_2N_6$ and $Sr_5Ge_2N_6$ obtained from the Birch-Murnaghan equations of state E(V).

| | **$Ca_5Si_2N_6$** | **$Sr_5Ge_2N_6$** |
|---|---|---|
| $E_0$ (eV) | -13699,23057 | -12036,42472 |
| $V_0$ (Å$^3$) | 364,84018 | 448,18414 |
| $B_0$ (GPa) | 100,42378 | 78,07899 |
| $B_0'$ | 4,33834 | 5,08142 |

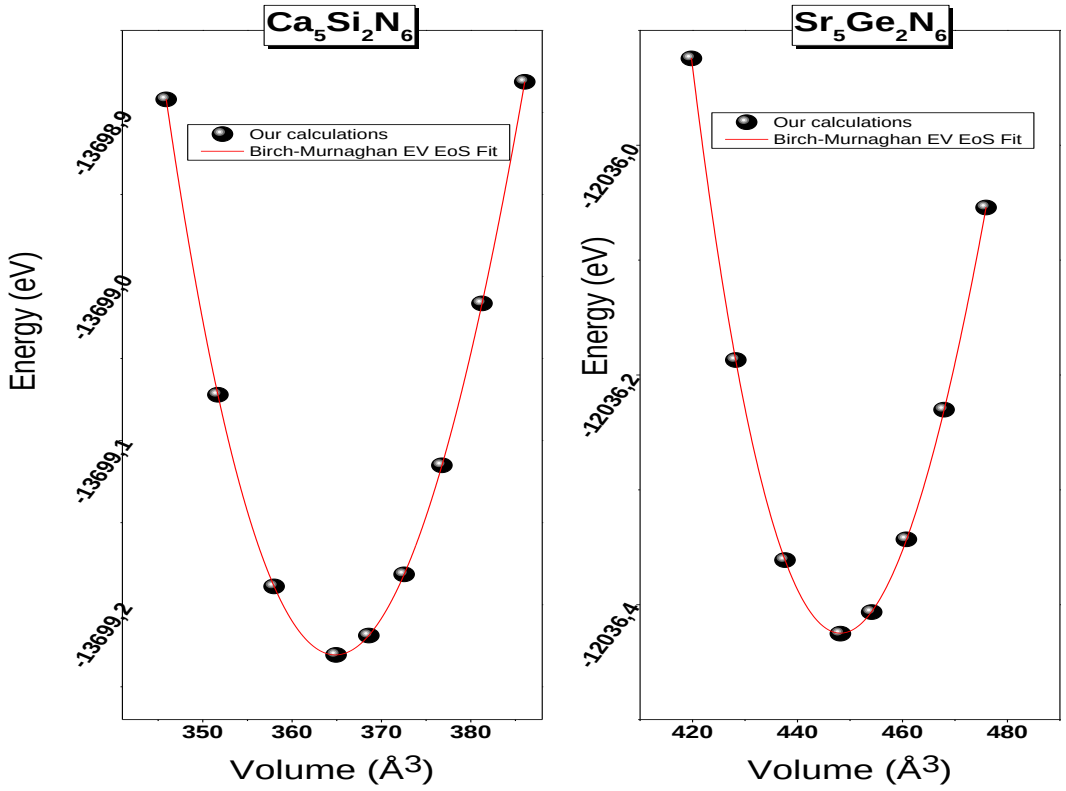


**Figure IV.2:** Variation of total energy as a function of unit cell volume of $Ca_5Si_2N_6$and $Sr_5Ge_2N_6$, obtained with GGA -PBEsol.

### IV.2.3. Thermodynamic stability

To investigate the chemical and structural stability of the studied compounds, the cohesive energy $E_{coh}$ and the formation enthalpy $\Delta H_f$ were estimated according to the following equations [8]:

$$E_{coh} = \frac{1}{N_{Ca}+N_{Si}+N_N}\left[E_{Tot}(Ca_5Si_2N_6) - \left(N_{Ca}E^{Ca}_{atom} + N_{Si}E^{Si}_{atom} + N_NE^N_{atom}\right)\right] \quad \text{(IV.2)}$$

$$\Delta H_f = \frac{1}{N_{Ca}+N_{Si}+N_N}\left[E_{Tot}(Ca_5Si_2N_6) - (N_{Ca}E_{Ca} + N_{Si}E_{si} + N_NE_N)\right] \quad \text{( IV.3)}$$

Here, $N_{Ca}$, $N_{Si}$ and $N_N$ are the number of Ca, Si and N atoms in the primitive cell of Ca5Si2N6 and $E_{Tot}(Ca_5Si_2N_6)$ its total energy; $E^{Ca}_{atom}$ , $E^{Si}_{atom}$ and $E^N_{atom}$ denote the total energies of isolated Ca, Si and N atoms, respectively; $E_{Ca}$,$E_{si}$ and $E_N$ represent the total energies per atom of the pure element Ca ,Si and N in bulk form. The two energy definitions for the other material ($Sr_5Ge_2N_6$) are identical. As shown in Table IV.3, the obtained cohesive energy and formation enthalpy values are negative, indicating the thermodynamic stability of the examined crystals at normal conditions of pressure and temperature. Further, $Ca_5Si_2N_6$ is more stable than $Sr_5Ge_2N_6$ at zero pressure and temperature due to lower negative cohesive energy and formation enthalpy.

**Table IV.3:** Calculated cohesive energy and enthalpy of formation values (eV/atom) (for the ternary nitrides $Ca_5Si_2N_6$ and $Sr_5Ge_2N_6$.

| | $E_{coh}$ | $\Delta H_f$ |
|---|---|---|
| **$Ca_5Si_2N_6$** | -6.96 | -1.54 |
| **$Sr_5Ge_2N_6$** | -6.19 | -1.03 |

For further confirmation of the dynamic stability of the title compounds, the phonon-dispersion curves along the high symmetry lines in the Brillouin zone were calculated for both compounds. As seen from the phonon-dispersion curve of $Ca_5Si_2N_6$ and $Sr_5Ge_2N_6$ represented in Figure IV.3, the dispersion branches have positive frequencies at any vector, implying that the compounds of interest are dynamically stable.

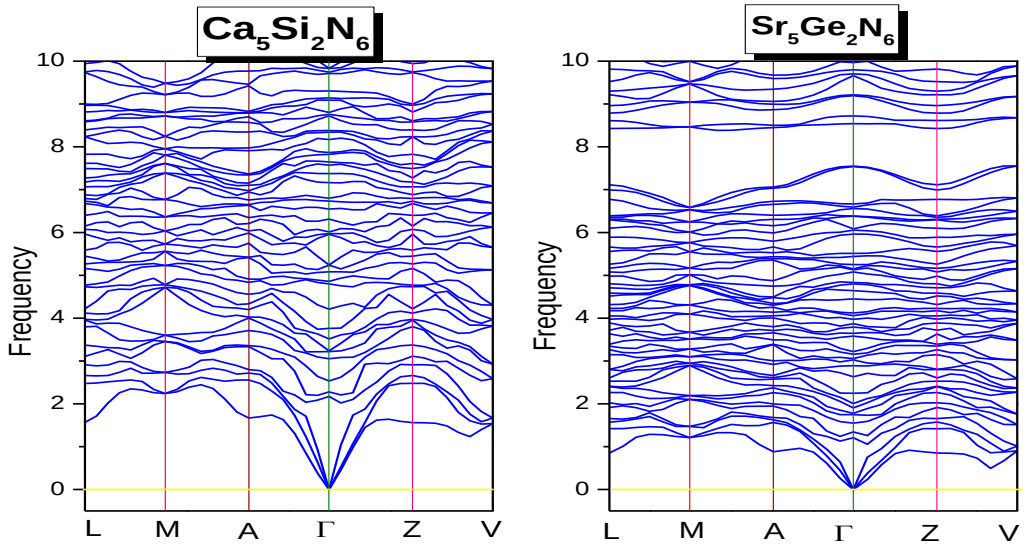


**Figure IV.3:** Calculated phonon dispersion along the high symmetry lines in the Brillouin zone for $Ca_5Si_2N_6$ and $Sr_5Ge_2N_6$ .

### IV.2.4. Pressure effect on the structural parameters of $Ca_5Si_2N_6$ and $Sr_5Ge_2N_6$

We calculated the pressure-dependent of the lattice parameters (a, b, c) , volume and the β-angle of the compounds $Ca_5Si_2N_6$ and $Sr_5Ge_2N_6$ in the pressure range from 0 to16 GPa with a step of 2 GPa. The performed calculations show that a, b and c for $Ca_5Si_2N_6$ and ($Sr_5Ge_2N_6$) decrease by 3.74% (4.2%), 4.75% (6.66%) and 3.25% (3.12%), respectively ( see Figures: IV.4, IV.5 and IV.6). However, the change in the angle β is small by 1.08% and 1.25% for $Ca_5Si_2N_6$ and $Sr_5Ge_2N_6$ respectively. However, all the structural parameters, the angle and the volume can be approximated fairly well by second order polynomials as following:

$$X / X_0 = 1 + A \times P + B \times P^2 \qquad \text{(IV.4)}$$

Where X represents the lattice constants a, b, c and the volume V and β-angle at a pressure P, and $X_0$ is the corresponding values at zero pressure. We can see from the Figures: IV.4 and IV.5 that $a/a_0$, $b/b_0$ and $c/c_0$ and $V/V_0$ decrease with increasing pressure according to the following expressions:

$$a/a_0^{Ca_5Si_2N_6} = 1 - 0.00283P + 3.18815\times10^{-5}P^2$$
$$a/a_0^{Sr_5Ge_2N_6} = 1 - 0.00307P + 2.78865\times10^{-5}P^2$$
$$b/b_0^{Ca_5Si_2N_6} = 1 - 0.00366P + 4.4142\times10^{-5}P^2$$
$$b/b_0^{Sr_5Ge_2N_6} = 1 - 0.00561P + 9.46088\times10^{-5}P^2$$
$$c/c_0^{Ca_5Si_2N_6} = 1 - 0.00266P + 4.00133\times10^{-5}P^2$$
$$c/c_0^{Sr_5Ge_2N_6} = 1 - 0.00261P + 4.18367\times10^{-5}P^2$$
$$V/V_0^{Ca_5Si_2N_6} = 1 - 0.00936P + 1.34682\times10^{-4}P^2$$
$$V/V_0^{Sr_5Ge_2N_6} = 1 - 0.01147P + 1.85791\times10^{-4}P^2$$

While, the $\beta/\beta_0$ increases slightly with increasing pressure according to the following expressions (see Figure: IV.6);

$$\beta/\beta_0^{Ca_5Si_2N_6} = 1 + 9.3166\times10^{-4}P - 1.68518\times10^{-5}P^2$$
$$\beta/\beta_0^{Sr_5Ge_2N_6} = 1 + 0.001P - 1.38634\times10^{-5}P^2$$

From Figure IV.4, it can be observed that $b/b_0$ decreases faster than $a/a_0$ and $c/c_0$, indicating that the considered compounds are less compressible along the [001] and [100] crystallographic directions than along the [010 ] directions, i.e. the greatest compressibility is observed along the crystallographic b axis. These materials are slightly less compressible along the [001] direction than along the [100] direction, i.e., the least compression occurs along the c axis. This result suggests that the chemical bonds along the b-axis are less strong than those along the a- and c-axes.

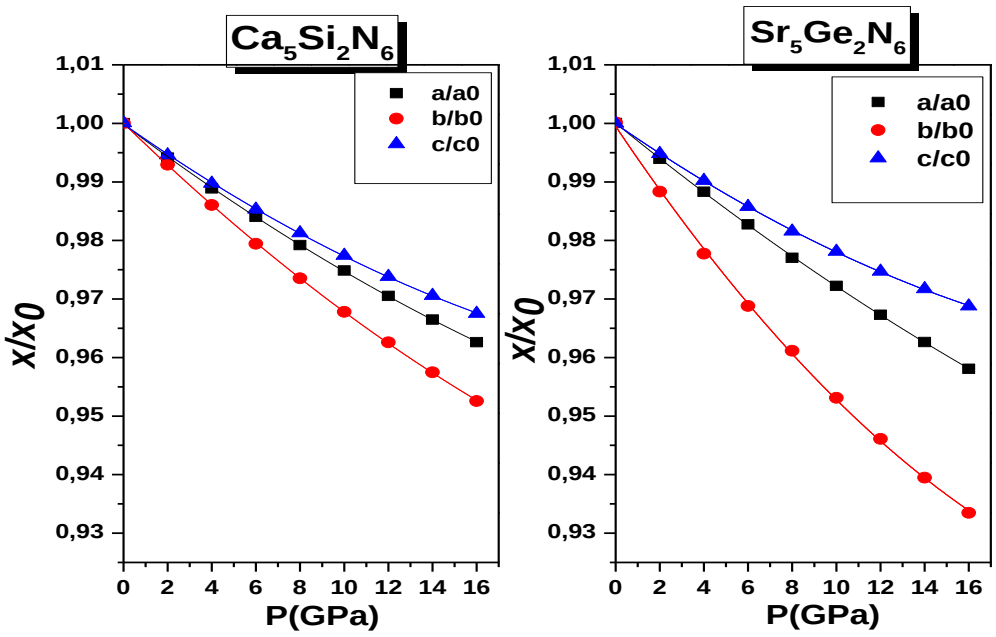


**Fi**

**gure IV.4**: Calculated pressure dependence of the normalized lattice parameters ratio, $a/a_0$, $b/b_0$ and $c/c_0$ for the $Ca_5Si_2N_6$ and $Sr_5Ge_2N_6$ compounds. Solid lines are least squares second-order polynomial fits of the data points.

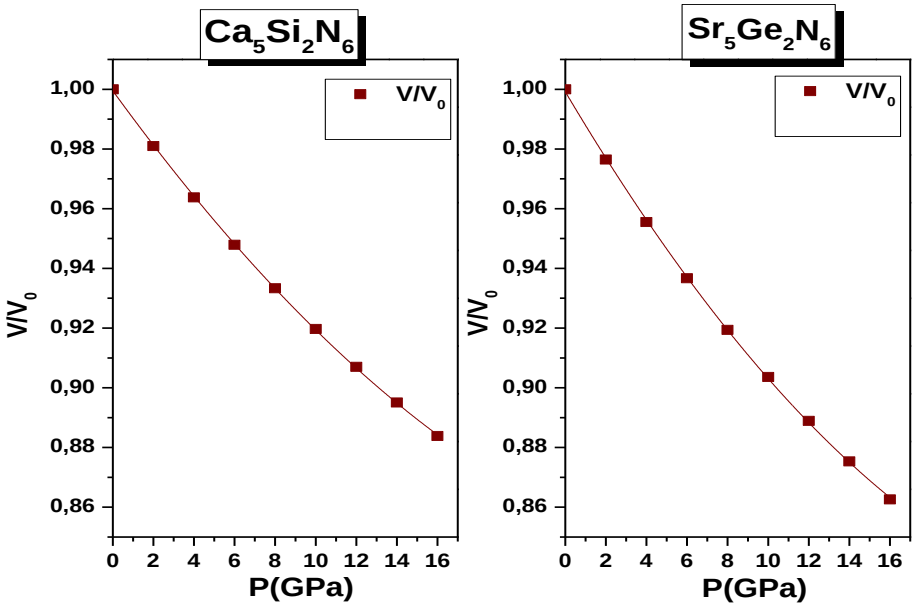


**Figure IV.5**: Calculated pressure dependence of the normalized unit-cell volume, $V/V_0$ for the $Ca_5Si_2N_6$ and $Sr_5Ge_2N_6$ compounds. Solid red lines are least squares second-order polynomial fits of the data points.

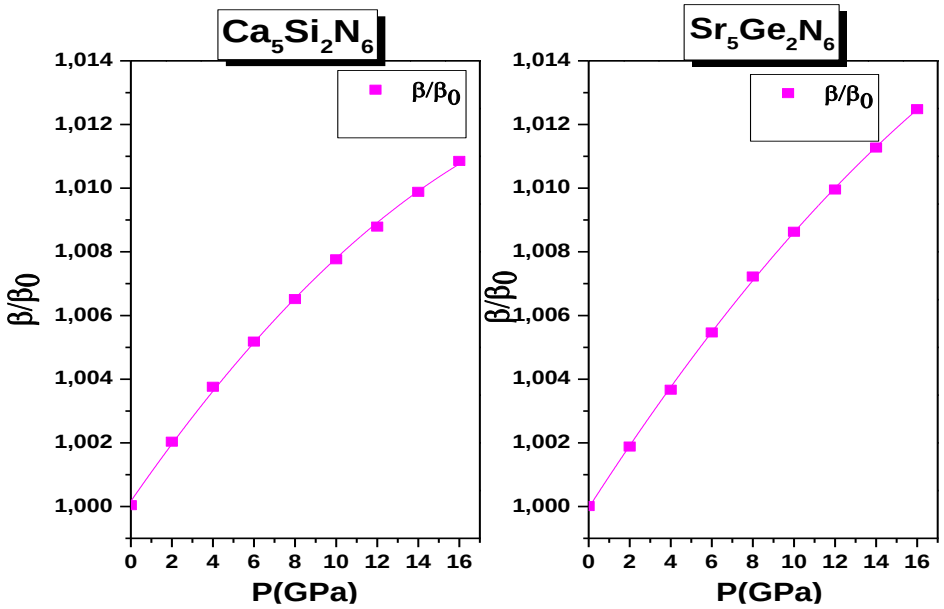


**Figure IV.6**: Calculated pressure dependence of the normalized angles ratio, β / β0 for the $Ca_5Si_2N_6$ and $Sr_5Ge_2N_6$ compounds. Solid lines are least squares second-order polynomial fits of the data points.

## IV.3. Elastic properties

The reciprocal relation between elastic properties and many other fundamental physical properties, from microscopic level (electronic properties, bond stiffness, etc.) to macroscopic level (dislocation, compressibility, etc.) gives the investigation of elastic properties a crucial importance in many fields of materials research [9-11]. Recently, DFT approaches allow us to predict reliable results for the elastic properties of a large scale of materials [12-14].

The elastic constants (Cijs) of $Ca_5Si_2N_6$ and $Sr_5Ge_2N_6$ were evaluated by employing the well-known finite strain method [1]. This technique encompasses enforcing a combination of similar deformations with a restricted worth and calculating the resulting stress with regard to optimizing the structure of the crystal, as implemented by Milman and Warren [15]. The polycrystalline elastic aggregate moduli and attached properties were obtained via the single-crystal elastic constants Cij over the Voigt-Reuss-Hill approximations [16–18].

### IV.3.1. Single-crystal elastic constants

The calculated elastic properties of the monoclinic systems for $Ca_5Si_2N_6$ and $Sr_5Ge_2N_6$ materials at zero pressure and for the optimized crystal are characterized by thirteen 13 independent elastic constants [19], namely, $C_{11}$, $C_{22}$, $C_{33}$, $C_{44}$, $C_{55}$, $C_{66}$, $C_{12}$, $C_{13}$, $C_{15}$, $C_{23}$, $C_{25}$, $C_{35}$ and $C_{46}$ are summarized in Table IV.4. There are no experimental or theoretical data for the elastic constants of $Ca_5Si_2N_6$ and $Sr_5Ge_2N_6$ in the scientific literature to compare with our findings.

**Table IV.4**: Calculated independent single-crystal elastic constants (*C*ij, in GPa) for the $Ca_5Si_2N_6$ and $Sr_5Ge_2N_6$ compounds.

| | **$C_{11}$** | **$C_{22}$** | **$C_{33}$** | **$C_{44}$** | **$C_{55}$** | **$C_{66}$** | **$C_{12}$** | **$C_{13}$** | **$C_{15}$** | **$C_{23}$** |
|---|---|---|---|---|---|---|---|---|---|---|
| **$Ca_5Si_2N_6$** | 181 | 128 | 213 | 58 | 55 | 53 | 84 | 36 | -14 | 80 |
| **$Sr_5Ge_2N_6$** | 147 | 95 | 158 | 41 | 40 | 35 | 61 | 38 | -4.84 | 69 |

| | **$C_{25}$** | **$C_{35}$** | **$C_{46}$** |
|---|---|---|---|
| **$Ca_5Si_2N_6$** | -0.30 | -18 | -10 |
| **$Sr_5Ge_2N_6$** | -5.57 | -8.57 | -7.82 |

From Table IV.4 we can depict the following conclusions:

1. The calculated elastic constants $C_{ij}$ for both considered materials satisfy the mechanical stability criteria for monoclinic structures [19].

$$C_{ii} > 0;\ i = 1;\ 2;\ 3;\ 4;\ 5;\ 6 \qquad \text{(IV.5)}$$

$$\left[C_{11} + C_{22} + C_{33} + 2\left(C_{12} + C_{13} + C_{22}\right)\right] \succ 0 \qquad \text{(IV.6)}$$

$$\left(C_{33}C_{55} - C_{35}^2\right) \succ 0,\ \left(C_{44}C_{66} - C_{46}^2\right) \succ 0,\ \left(C_{22} + C_{33} - 2C_{23}\right) \succ 0 \qquad \text{(IV.7)}$$

$$\left[C_{22}\left(C_{33}C_{55} - C_{35}^2\right) + 2C_{23}C_{25}C_{35} - C_{23}^2C_{55} - C_{25}^2C_{33}\right] \succ 0 \qquad \text{(IV.8)}$$

$$\left\{\begin{array}{l} 2\left[C_{15}C_{25}\left(C_{33}C_{12} - C_{13}C_{23}\right) + C_{15}C_{35}\left(C_{22}C_{13} - C_{12}C_{23}\right) + C_{25}C_{35}\left(C_{11}C_{23} - C_{12}C_{13}\right)\right] \\ -\left[C_{15}^2\left(C_{22}C_{33} - C_{23}^2\right) + C_{25}^2\left(C_{11}C_{33} - C_{13}^2\right) + C_{35}^2\left(C_{11}C_{22} - C_{12}^2\right)\right] + C_{55}g \end{array}\right\} \succ 0 \qquad \text{(IV.9)}$$

$$g = C_{11}C_{22}C_{33} - C_{11}C_{23}^2 - C_{22}C_{13}^2 - C_{33}C_{12}^2 + C_{12}C_{13}C_{23}\,. \qquad \text{(IV.10)}$$

Thus, we can assert that the monoclinic $Ca_5Si_2N_6$ and $Sr_5Ge_2N_6$ materials are in a mechanically stable state.

2. The elastic constants $C_{11}$, $C_{22}$ and $C_{33}$ reflect the stiffness to uniaxial strains along the crystallographic a-axes ([100]), b-axes ([010]) and c-axes ([001]). So that $C_{33} > C_{11} > C_{22}$, suggesting that the crystal structures of $Ca_5Si_2N_6$ and $Sr_5Ge_2N_6$ should be more easily compressible along the b axis than along a and c axes.
3. The values $C_{44}$, $C_{55}$ and $C_{66}$ (which reflects the stiffness to shear deformation) are lower than the stiffness to uniaxial strain (i.e.: $C_{11}$, $C_{22}$ and $C_{33}$) by about 60%, suggesting that $Ca_5Si_2N_6$ and $Sr_5Ge_2N_6$ are more resistive to unidirectional compression than to shear deformation. Additionally, it is important to mention here that $Ca_5Si_2N_6$ has a higher stiffness compared to $Sr_5Ge_2N_6$.

### IV.3.2. Polycrystalline elastic properties

Large single crystals are often difficult to get at the moment, making it impossible to quantify the individual elastic constants. Instead of measuring Cij, the bulk modulus B and shear modulus G can be evaluated experimentally on the polycrystalline samples, and then used to define the mechanical properties of the material. These two macroscopically measurable quantities (B and G) can be theoretically calculated by a special averaging of the independent elastic constants Cij of the monocrystalline phase. The Voigt–Reuss–Hill homogenization methods were used to estimate the B and G moduli [16-18]. Voigt and Reuss approximations are known to give respectively higher and lower values for B and G, while Hill approximation take the arithmetic mean of these two limits. Hill's values give as effective moduli in practice for polycrystalline samples [16-18]. Therefore, we have adopted here the Hill's approximation [18] to evaluate the polycrystalline elastic module for the titled compounds, which is defined as follows:

$$B_H = \frac{B_V + B_R}{2} \qquad \text{(IV.11)}$$

$$G_H = \frac{G_V + G_R}{2} \qquad \text{(IV.12)}$$

The definitions of the $B_V$, $B_R$, $G_V$ and $G_R$ bounds for a monoclinic structure:

$$\begin{cases} B_R = \Omega\left[\begin{matrix}\alpha+(C_{11}+C_{22}-2C_{12})+b(2C_{12}-2C_{11}-C_{23})+c(C_{15}-C_{25})+\\ d(2C_{12}+2C_{23}-C_{13}-2C_{22})+2e(C_{25}-C_{15})+f\end{matrix}\right]^{-1} \\ B_v = \frac{1}{9}\left[C_{11}+C_{22}+C_{33}+2(C_{12}+C_{13}+C_{23})\right] \\ G_v = \frac{1}{15}\left[C_{11}+C_{22}+C_{33}+3(C_{44}+C_{55}+C_{66})-(C_{12}+C_{13}+C_{23})\right] \\ G_R = 15\left\{\frac{4\left[\alpha(C_{11}+C_{22}+C_{12})+b(C_{11}-C_{12}-C_{23})+c(C_{15}+C_{25})+d(C_{22}-C_{12}-C_{23}-C_{13})+e(C_{15}-C_{25})+f\right]}{\Omega+3\left[\frac{g}{\Omega}+\left(\frac{C_{44}+C_{66}}{C_{44}C_{66}-C_{46}^2}\right)\right]}\right\}^{-1} \\ \alpha = C_{33}C_{55}-C_{35}^2 \\ b = C_{23}C_{55}-C_{25}C_{35} \\ c = C_{12}C_{35}-C_{15}C_{33} \\ d = C_{13}C_{55}-C_{15}C_{35} \\ e = C_{13}C_{25}-C_{15}C_{23} \\ f = C_{11}(C_{22}C_{33}-C_{25}^2)-C_{12}(C_{12}C_{55}-C_{15}C_{25})+C_{15}(C_{12}C_{25}-C_{15}C_{22})+C_{25}(C_{23}C_{35}-C_{25}C_{33}) \\ g = C_{11}C_{22}C_{33}-C_{11}C_{23}^2-C_{22}C_{13}^2-C_{33}C_{12}^2+2C_{12}C_{13}C_{23} \\ \Omega = \left\{\begin{matrix}2\left[C_{15}C_{25}(C_{33}C_{12}-C_{13}C_{23})+C_{15}C_{35}(C_{22}C_{13}-C_{12}C_{23})+C_{25}C_{35}(C_{11}C_{23}-C_{12}C_{23})\right]-\\ \left[C_{15}^2(C_{22}C_{33}-C_{23}^2)+C_{25}^2(C_{11}C_{33}-C_{13}^2)+C_{35}^2(C_{11}C_{22}-C_{12}^2)\right]+gC_{55}\end{matrix}\right\} \end{cases} \quad \text{(IV.13)}$$

The computed values of bulk and shear moduli were used to evaluate the Young's modulus E and Poisson's ratio by using the following relations:

$$E = 9BG(3B+G)^{-1} \quad \text{(IV.14)}$$

$$\nu = (1/2)(3B-2G)(3B+G)^{-1} \quad \text{(IV.15)}$$

The obtained values of the above-mentioned parameters for the herein considered materials are summarized in Table IV.5. It is well known that a material's stiffness can be assessed by looking at its bulk modulus, which measures the resistance to volume change under hydrostatic pressures, shear modulus G, which represents the resistance to reversible deformation under shear stress, and Young's modulus E, which measures the ratio of linear stress to linear strain in the case of tensile forces.

**Table IV.5**: Calculated Bulk modulus (*B*, in GPa), shear modulus (*G*, in GPa), Young's modulus (*E*, in GPa), B/*G* ratio and Poisson's ratio ($\nu$, dimensionless) for $Ca_5Si_2N_6$ and $Sr_5Ge_2N_6$ compounds.

| | $B_V$ | $B_R$ | $B_H$ | $G_V$ | $G_R$ | $G_H$ | E | B/G | $\nu$ |
|---|---|---|---|---|---|---|---|---|---|
| **$Ca_5Si_2N_6$** | 102 | 100 | 101 | 55 | 45 | 50 | 129 | 2.02 | 0.29 |
| **$Sr_5Ge_2N_6$** | 82 | 79 | 80.5 | 39 | 33 | 36 | 95 | 2.2 | 0.3 |

According to the values in the Table IV.5, we can obtain the following conclusions:

1. The bulk modulus (B) values obtained the calculated single-crystal elastic constants are in good agreement with those calculated from the EOS fitting.
2. The bulk modulus B decreases with increasing atomic number Z of the atoms in the compounds $Sr_5Ge_2N_6$ and $Ca_5Si_2N_6$; it means that the $Sr_5Ge_2N_6$ compound is more compressible than the other compound ($Ca_5Si_2N_6$).
3. The isotropic elastic moduli B, G and Young's modulus (E) has relatively large values, reflecting the relatively high stiffness of the considered materials. The calculated hardness is about 4.7 GPa for $Sr_5Ge_2N_6$ and 6.6 GPa for $Ca_5Si_2N_6$ materials.
4. The B value is practically twice the value of G; this implies that the parameter limiting the mechanical stability of these materials is the shear modulus.
5. Additionally, Bulk and shear module provide information regarding the malleability of materials through Pugh's empirical criterion B/G [20]. According to this criterion, if B/G smaller than 1.75, a brittle behavior is predicted; otherwise, the material behaves in a ductile manner. The examined compounds have Pugh's ratios greater than 1.75, indicating that these materials are ductile and will be resistant to thermal shocks.
6. In this context, the failure mode (ductility/brittleness) can also be predicted via the Poisson's ratio with a critical value of $\upsilon$=0.26 [21-22]. If $\upsilon$ is greater (less) than 0.26, a material undergoes ductile (brittle) failure. The $\upsilon$ values of $Ca_5Si_2N_6$ and $Sr_5Ge_2N_6$ are equal to 0.29 and 0.30, implying again their ductile nature. This good agreement confirms the reliability and accuracy of the current calculations. Poisson's ratio appears as an effective tool to assess the nature of chemical bonding in crystals [23]. The value of the Poisson's ratio $\upsilon$ is equal to 0.33 for completely metallic materials, whereas for purely ionic compounds, a typical value of $\upsilon$ is 0.25. Based on these conditions, the stability of the studied materials are maintained by a mixture of metallic and ionic bonds.

### IV.3.3. Debye temperature and acoustic wave velocities

To provide a thorough description of the mechanical properties, the Debye temperature $\theta_D$ of the tested materials were estimated from the isotropic average sound velocity $V_m$ via the following expression [24]:

$$\theta_D = \frac{h}{K_B}\left[\frac{3n\rho N_A}{4\pi M}\right]^{1/3} V_m \qquad \text{(IV.16)}$$

Where h is Plank's constant, $k_B$ is Boltzmann's constant, n is the number of atoms in the molecule, $N_A$ is Avogadro's number, $\rho$ is the density and $M$ is the molar mass. In a polycrystalline material, $V_m$ can be computed using the longitudinal and transversal sound wave velocities ($V_l$ and $V_t$) [24-25] as follows :

$$V_m = \left[\frac{1}{3}\left(2V_t^{-3} + V_l^{-3}\right)\right]^{-1/3} \quad \text{(IV.17)}$$

$$V_l = \left(\frac{3B + 4G}{3\rho}\right)^{1/2} \quad \text{(IV.18)}$$

$$V_t = \left(\frac{G}{\rho}\right)^{1/2} \quad \text{(IV.19)}$$

Where $B$ and $G$ are the DFT calculated bulk and shear moduli. Recently, the material's Debye temperature $T_D$ is considered as the most reliable proxy for phosphor materials, due to its proportionality to the structural rigidity, it is often connected to thermal quenching mechanisms and quantum yield [26-29]. As a result, this has even been included into machine learning algorithms to seek for new promising phosphor materials [30-31]. According to Table IV.6, $Ca_5Si_2N_6$ has the highest Debye temperature (> 500K), confirming that it is suitable for use as a phosphor material [26, 30-31]. In contrast, the nitridogermanate has a lower Debye temperature value (360K) due to its substitution with heavier cations, resulting in lower the overall phononic contributions.

**Table IV.6:** Calculated density (ρ in g/cm3), longitudinal, transverse and average sound velocities ($V_l$, $V_t$ and $V_m$, respectively in m/s) and Debye temperature ($\theta_D$ in K) for the monoclinic of $Sr_5Ge_2N_6$ and $Ca_5Si_2N_6$ materials.

| | $\rho$ | $V_l$ | $V_t$ | $V_m$ | $\theta_D$ |
|---|---|---|---|---|---|
| **$Ca_5Si_2N_6$** | 3.09 | 7371 | 4032 | 4443 | 548 |
| **$Sr_5Ge_2N_6$** | 4.9 | 5116 | 2716 | 3003 | 346 |

### IV.3.4. Elastic anisotropy

Another intriguing physical parameter related to the elastic properties of solids is the elastic anisotropy, which reflects different bonding natures in different crystallographic

directions. The crystal anisotropy plays an important role in many mechanical properties of solids, such as elastic instability, phase transformations, dislocation dynamics, etc.. Moreover, micro cracks can be easily induced in materials with significant elastic anisotropy; thus to improve their mechanical durability, it is important to evaluate their elastic anisotropy [32]. At present, to accurately quantify the elastic anisotropy for the investigated materials, we have used three different;

1. The percentage of elastic anisotropy in compression $A_B$ and shear $A_G$ proposed by Chung and Buessem [33]: , which is commonly used to estimate crystal elastic anisotropy, is defined by the following formulas :

$$A_B = \frac{B_v - B_R}{B_v + B_R} \times 100 \qquad \text{(IV.20)}$$

$$A_G = \frac{G_V - G_R}{G_V + G_R} \times 100 \qquad \text{(IV.21)}$$

The higher the percentage, the greater the anisotropy in the crystal.

Zero value for $A_B$ and $A_G$ corresponds to elastic isotropy, while a value of 100% is associated with the largest possible anisotropy. According to Table IV.7 data, both materials exhibit a large anisotropy in shear and compression.

2. A truest representative of the elastic anisotropy is the universal anisotropic index $A^U$ proposed by Ranganathan et al. [34] defined as:

$$A^U = 5\frac{G_V}{G_R} + \frac{B_v}{B_R} - 6 \qquad \text{(IV.22)}$$

For perfect isotropic crystals, $A^U$ is equal to zero ($A^U = 0$); the deviations of $A^U$ from zero define the anisotropy level of a crystal. The estimated values of $A^U$ are found to be 1.03 for $Ca_5Si_2N_6$ and 0.785 for $Sr_5Ge_2N_6$, revealing a significant elastic anisotropy for both compounds.

**Table IV.7:** Calculated anisotropy in compression ($A_B$), anisotropy in shear ($A_G$) and the anisotropy universal index $A^U$ for the $Ca_5Si_2N_6$ and $Sr_5Ge_2N_6$ compounds.

| | $A_B$ (%) | $A_G$ (%) | $A^U$ |
|---|---|---|---|
| **$Ca_5Si_2N_6$** | 1.2962 | 9.13 | 1.03 |
| **$Sr_5Ge_2N_6$** | 1.8468 | 6.97 | 0.785 |

3. The representation in three dimensions (3D) of the surface representing the variation of an elastic modulus with the crystallographic directions is a very effective method for the visualization of the elastic anisotropy of a crystal. In an isotropic crystal, this closed surface has exactly a spherical shape. Any deviation from the spherical shape of this surface indicates the presence of elastic anisotropy and its magnitude is proportional to the degree of deviation from the spherical shape of this surface. The dependence of Young's modulus E and linear compressibility β on crystal directions for a monoclinic system is given by the following relationships [35]:

$$\frac{1}{E} = l_1^4 s_{11} + 2l_1^2 l_2^2 s_{12} + 2l_1^2 l_3^2 s_{13} + 2l_1^3 l_2 s_{15} + l_2^4 s_{22} + 2l_2^2 l_2^3 s_{23} + 2l_1 l_2^2 l_3 s_{25} + l_3^4 s_{33} + l_2^2 l_3^3 s_{44} + 2l_1 l_2^2 l_3 s_{46} + l_1^2 l_2^3 s_{55} + l_1^2 l_2^3 s_{66} \quad \text{(IV.23)}$$

$$\beta = \left(s_{11} + s_{12} + s_{13}\right) l_1^2 + \left(s_{12} + s_{22} + s_{23}\right) l_2^2 + \left(s_{13} + s_{23} + s_{33}\right) l_3^2 + \left(s_{15} + s_{25} + s_{35}\right) l_3 l_1 \quad \text{(IV.24)}$$

Here, $l_1$, $l_2$ and $l_3$ are the directional cosines with respect to the *x*-, *y*- and *z*-axes, respectively, and the $S_{ij}$ refer to the compliance constants.

Fig. IV.7 and Fig. IV.8 Illustrates three-dimensional representation of the directional dependence of the Young's modulus E and linear compressibility β together with its cross section in the (X= Y) Z, XY, XZ and YZ crystallographic planes for $Ca_5Si_2N_6$ and $Sr_5Ge_2N_6$ materials respectively. from Fig. IV.7 (Fig. IV.8), one can note the appreciable deviation of the 3D representation of the Young's modulus and linear compressibility from the spherical shape in both studied materials, we can therefore conclude that the materials studied exhibit a pronounced elastic anisotropy. To better understand the origin of the changes in Young's modulus and compressibility modulus along different directions, we also visualize them along the (X= Y) Z, XY, XZ and YZ planes of Figs. IV.7 and IV.8 From these cross-sectional sections, we can see that Young's modulus linear compressibility β shows less anisotropy in the YZ plane compared to the other planes for $Ca_5Si_2N_6$. We can see clearly from Figs. IV.7 and IV.8 that $Sr_5Ge_2N_6$ is more anisotropic in compression than $Ca_5Si_2N_6$

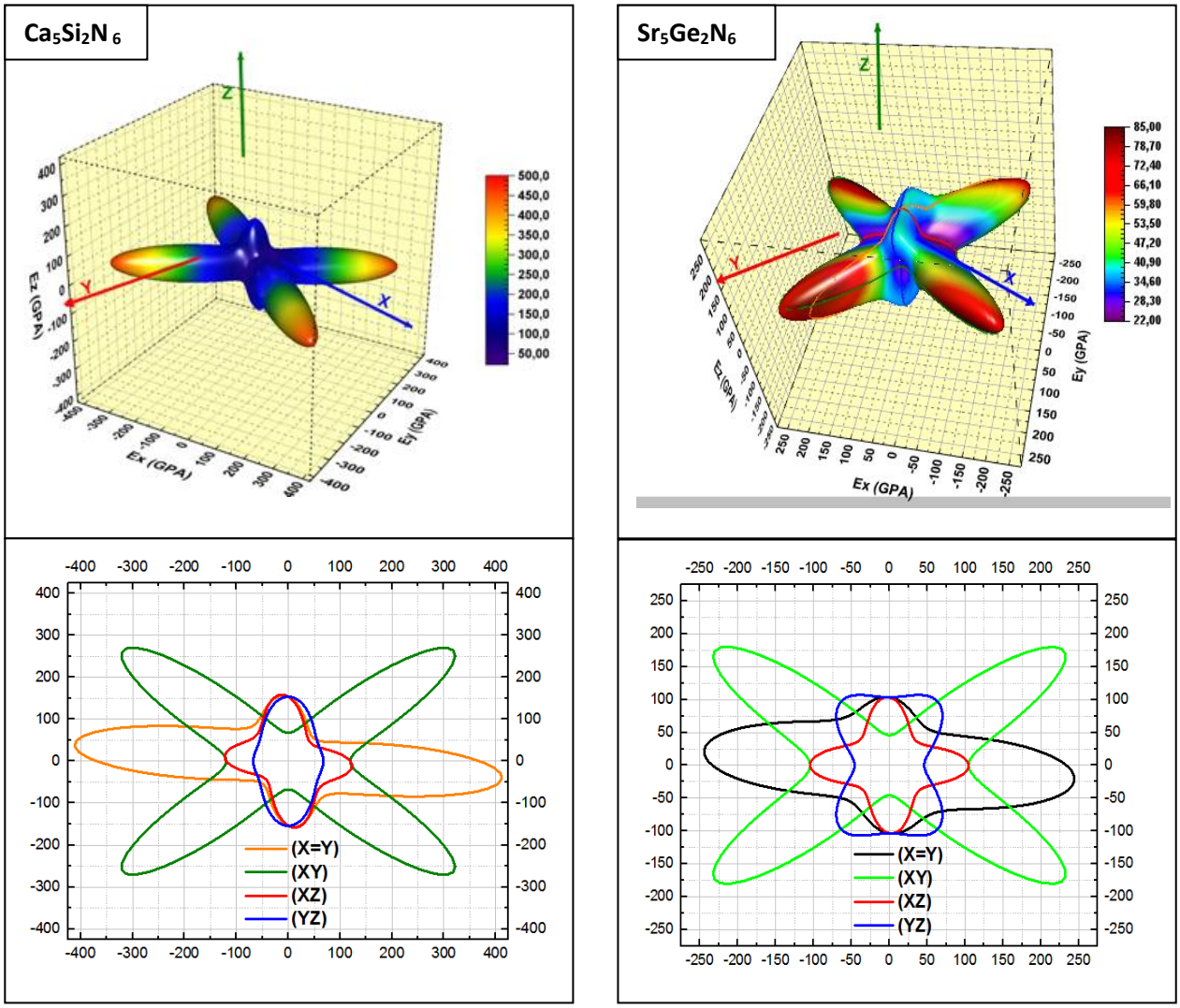


**Figure IV.7**: Illustration of the directional dependence of Young's modulus E and their cross sections in various planes for the $Ca_5Si_2N_6$ and $Sr_5Ge_2N_6$ materials.

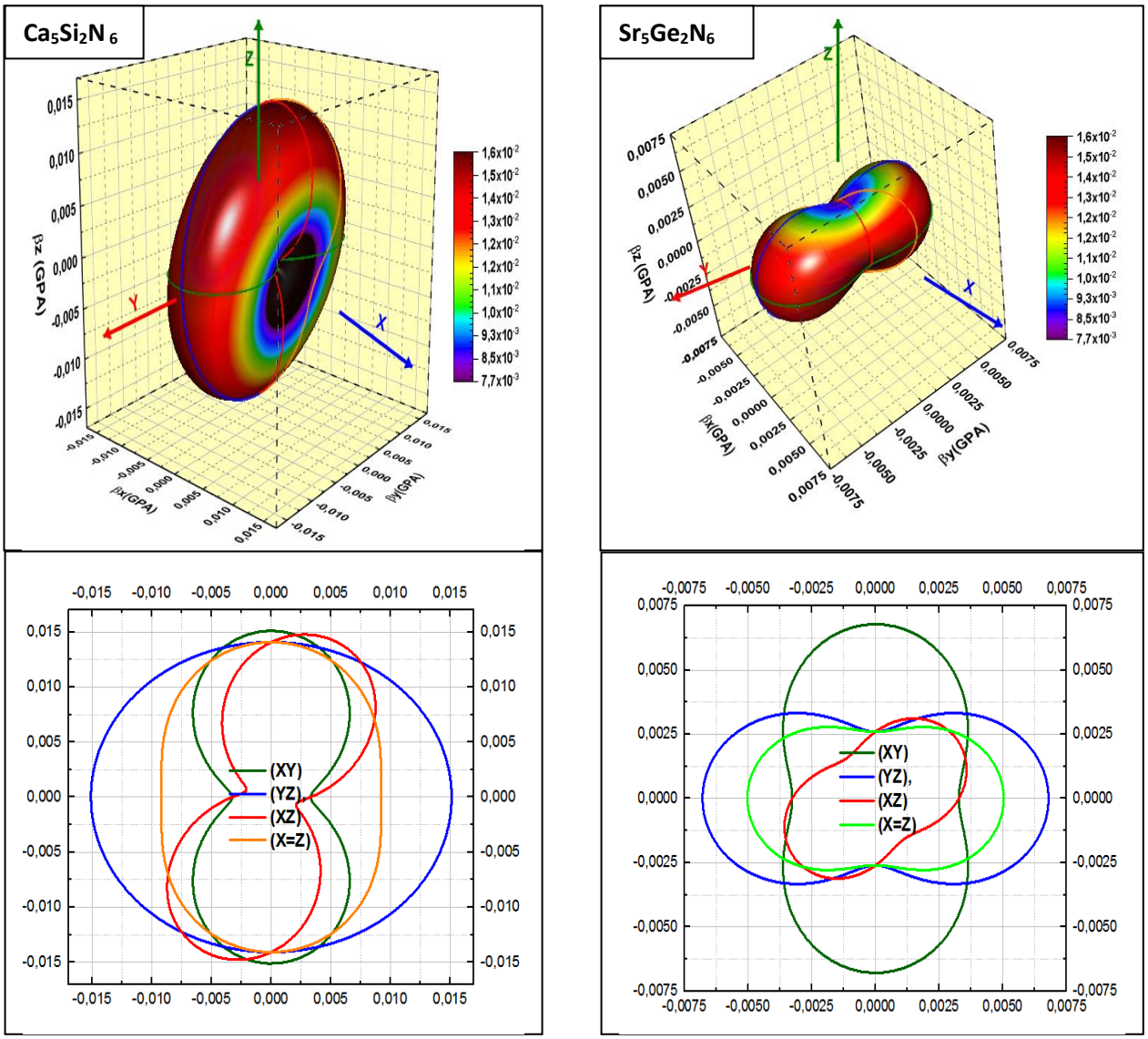


**Figure IV.8:** Illustration of the directional dependence of the linear bulk modulus and their cross sections in various planes for the$Ca_5Si_2N_6$ and $Sr_5Ge_2N_6$ materials.

## IV.4. Electronic properties

Knowing the Debye temperature of a crystal structure alone is insufficient to assess the potential suitability of $Ca_5Si_2N_6$ and $Sr_5Ge_2N_6$ as luminescent materials. A wide band gap (Eg) is also essential when screening for new phosphors [30-31,36]. Therefore, the electronic properties of the herein studied compounds were investigated through their band structure, total and partial density of state (TDOS and PDOS). Various first–principles approaches have been used to examine electronic properties and highlight the atomic contribution to the band structure curves.

It is well established that the common generalized gradient approximation calculation (we used the PBEsol [2] flavor of GGA) consistently underestimates the energy-gaps of semiconductors and insulators by about 30–50% [37–39] compared to the experimental ones. This band-gap problem arises because conventional approaches such as GGA and LDA cannot characterize precisely the agitated electronic states. To address this deficiency and acquire credible energy-gap amounts for semiconductors and insulators in comparison to a experimental ones, some advanced XC functionals have been developed, including hybrid functionals [40], the GW approximation [41], and the Tran-Blaha altered Becke-Johnson (TB-mBJ) potential [42-43]. Compared to the other approaches stated above, the TB-mBJ planner is computationally less expensive and provides energy band gaps that are nearly equal to the experimental ones with an extremely lower counting time [42-43]. For this reason and in addition to the GGA-PBEsol, the optoelectronic and thermoelectric properties of the examined materials have been studied by employing the TB-mBJ functional as embedded in the WIEN2k code [44]. The schedule bundle WIEN2k [44] is an accomplishment of the full potential linearized augmented plane wave (FP-LAPW) formalism within the DFT framework. In the FP-LAPW approach, the unit cell is split into non-overlapping muffin-tin spheres (MTS) separated by a space known as the interstitial region (IR). In the MTS, the wave functions have been expanded using a linear collection of radial atomic functions with spherical harmonics, whereas in the IR, a plane wave foundation collection is employed. A plane-wave cutoff parameter RMT*Kmax is set to be equal to 7. RMT denoted the slightest radius of the muffin-tin sphere and Kmax denoted the biggest k-vector in the plane wave extension. The k-integration over the Brillouin zone is computed employing a mesh of 1000 k-points in the irreducible Brillouin zone, according to the Monkhorst–Pack scheme [4].

### IV.4.1. Electronic band structure

Figure IV.7 illustrates the calculated energy band structure of $Ca_5Si_2N_6$ and $Sr_5Ge_2N_6$ along the high symmetry directions L(0.5,-0.5,0),M(0.5,-0.5,0.5), A(0.5,0,0), Γ(0,0,0), Z(0,-0.5,0.5), V(0.5,0,0.5) in the first Brillouin zone (BZ) (shows fig IV.9 ) using the GGA-PBE sol and the TB- mBJ methods, respectively. The results show a clear separation between the valence band and the conduction band curves, making these compounds as semiconductor in nature. Our ab initio calculation within the GGA-PBE so yielded an indirect band gap of 2.29eV and 1.47eVfor both $Ca_5Si_2N_6$ and $Sr_5Ge_2N_6$ respectively. For both compounds, the valence band maximum occurs at the V-point and the conduction band minimum occurs at the Γ point (see bottom panel of Fig. IV.10). As it is knowing, GGA approaches are usually

underestimate the band gap value by about 30% —50%, it follows that the actual band gaps of the examined materials should be wider. For the two nitrides, the band profiles calculated using the TB-mBJ exchange potential are nearly identical to those of the GGA-PBEsol ones, with a distinct variation in their band gap values. As shown in the upper panel of Fig. IV.10, the band gap energy shifted from indirect to direct (V→V) for $Ca_5Si_2N_6$ at a value of 3.55 eV. Unlike $Sr_5Ge_2N_6$, the band gap remains indirect but with a value of 3.15 eV. There is no data on the band gap value in the literature to be compared with our findings. Another indication that nitridosilicate can be employed as activator induced luminescence (e.g. from $Eu^{2+}$ or $Ce^{3+}$) is that the band width of the compound is within 3.5-3.8eV [36,45]. This has already been proven by J. Huang et al., in their study of the $Eu^{2+}$ doped $Ca_5Si_2N_6$ material [46]. Contrary to $Sr_5Ge_2N_6$, when Sr and Ge atoms replace Ca and Si atoms respectively, leads to narrowing the Eg value. However, this nitridogermanate may still be appropriate for potential optical applications. It is worth to note here that the calculated Eg-mBJ values can be improved by partially substituting Li and Mg in $Sr_5Ge_2N_6$ for the discovery of new nitride germinates that may be used as phosphor materials or wide-gap semiconductors [36].

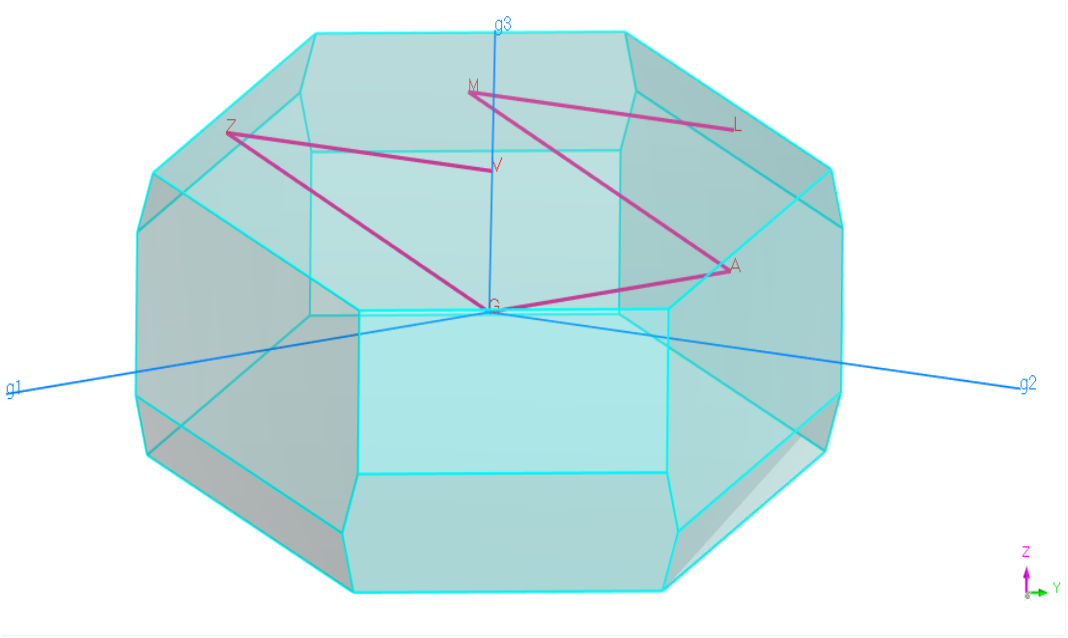


**Figure IV.9:** Brillouin zone of the monoclinic $Sr_5Ge_2N_6$ and $Ca_5Si_2N_6$ materials. The red line corresponds to the path of the band structure diagram

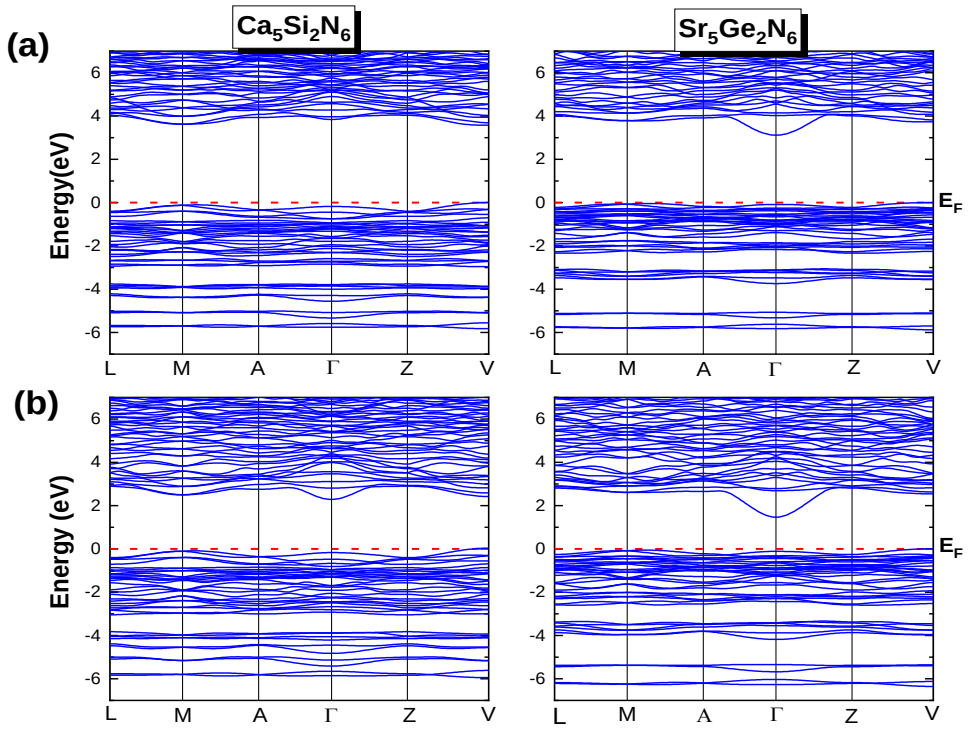


**Figure IV.10:** Electronic band structure of $Ca_5Si_2N_6$ and $Sr_5Ge_2N_6$ using

**(a)** TB-mBJ, and **(b)** GGA-PBEsol method.

### IV.4.2. Density of electronic states (Total and partial)

To shed light on the nature of the electronic band structure, the diagrams of total and atomic site projected densities of states (TDOS and PDOS, respectively) are plotted in Figure IV.11. For both crystals, there are three blocks V1,V2 and C1: the first block located around -4 (-3.25) eV for $Ca_5Si_2N_6$ ($Sr_5Ge_2N_6$) is mainly composed of N-p and (Si/Ge)-p states with a negligible contribution from (Ca/Sr)-sp states. The second block V2 extending from –3 eV and -2.2 eV up to Fermi level for $Ca_5Si_2N_6$ and $Sr_5Ge_2N_6$ respectively, originate mainly from the N-2p states with a small participation from the (Ca/Sr)-*p* and (Si/Ge)-*p*states. The third block C1 above the Fermi level of $Ca_5Si_2N_6$, comes principally from the unoccupied N(*s*, *p*) states with few contributions (*s*, *p*) states of Si and Ca atoms. The situation is not so different in the case of $Sr_5Ge_2N_6$, where the Sr atoms show a small contribution to the C1 block, and the N-2p and Ge-4s states dominate the conduction band followed by the N-2s and Ge-4p states. In other words, most electronic transitions should occur between the dominant N states

at the edge of the valence band and the unoccupied Ca, Sr, Ge, and N states in the conduction band.

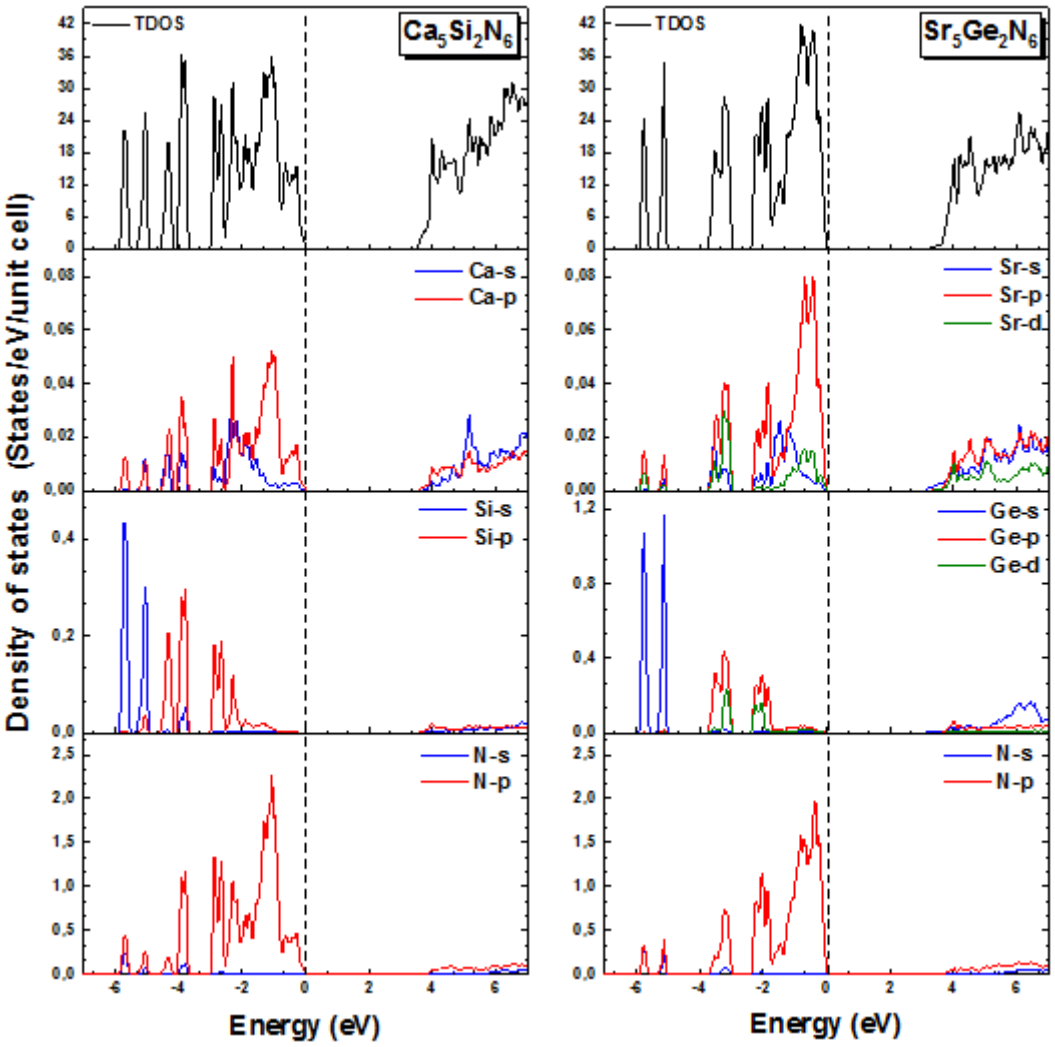


**Figure IV.11:** Total (TDOS) and partial (PDOS) density of state for of $Ca_5Si_2N_6$ and $Sr_5Ge_2N_6$ using the TB-mBJ functional.

## IV.5. Optical properties

It's crucial to understand the various ways in which light interacts with matter solid state physics, such as absorption, transmission, reflection, and scattering emission. Studying these properties provide significant information about the internal structure of these compounds.

The optical properties of a material can be accessed through the complex dielectric function $\varepsilon(\omega) = \varepsilon_1(\omega) + i\varepsilon_2(\omega)$, which is directly related to the linear response of matter to incident radiation. The second term $\varepsilon_2(\omega)$ of the complex dielectric function, which describes the absorption of the incident radiation by the material, can be evaluated by summing all

possible direct electronic transitions from occupied bands to vacant states [47]. The $\varepsilon_{1(\omega)}$ term, which characterizes how the material scatters or redirects the incoming light waves, can be derived from the $\varepsilon_2(\omega)$ via the Kramer–Kronig transformation [48]. All the frequency-dependent optical functions, such as the absorption coefficient $\alpha(\omega)$, optical reflectivity $R(\omega)$, extinction coefficient $k(\omega)$, refractive index $n(\omega)$, and energy-loss spectrum $L(\omega)$, can be calculated using the complex dielectric function $\varepsilon(\omega)$. To achieve more accurate calculations, a dense k-point mesh of 12000 is employed for determining the optical properties of $Ca_5Si_2N_6$ and $Sr_5Ge_2N_6$.

### IV.5.1. Dielectric function

The calculation of the dielectric function $\varepsilon(\omega)$ is necessary to describe the behavior of $Ca_5Si_2N_6$ and $Sr_5Ge_2N_6$ subjected to the influence of external electromagnetic wave. The dielectric function $\varepsilon(\omega)$ is a complex function which is directly related to the energy band structure of solids, while other optical properties are derived from this function. The dielectric function $\varepsilon(\omega)$ is defined as:

$$\varepsilon(\omega)=\varepsilon_1(\omega)+\varepsilon_2(\omega) \qquad \text{(IV.25)}$$

$\varepsilon_1(\omega)$The real part (called the dispersive part) characterizes the dispersion of electromagnetic radiation by the material.

$\varepsilon_2(\omega)$ The imaginary part characterizes the absorption of electromagnetic radiation by the material , it can be calculated from the energy bands by summing all possible direct transitions between occupied and unoccupied states, taking into account the transition probabilities and respecting the selection rules [49].

To characterize all the optical properties, it is sufficient to calculate the imaginary part of the dielectric function. We have [49]:

$$\begin{cases} \varepsilon_2(\omega)=\dfrac{Ve^2}{2\pi\hbar m^2\omega^2}\int d^3k\sum_{n,n'}\left|\langle kn|p|kn'\rangle\right|^2 f_{kn}\left(1-f_{kn'}\right)\delta\left(E_{kn}-E_{kn'}-\hbar\omega\right)\sum\left|\langle kn|p|kn'\rangle\right|^2 \\ f_{kn}\left(1-f_{kn'}\right)\left|\langle kn|p|kn'\rangle\right|^2 \; f_{kn}\left(1-f_{kn'}\right) \end{cases} \qquad \text{(IV.26)}$$

$$\varepsilon_2(\omega)=1+\frac{2}{\pi}T\int_0^{\infty}\frac{\omega'\varepsilon_2(\omega')}{\omega'^2-\omega^2}d\omega' \qquad \text{(IV.27)}$$

Where:

V is the unit cell volume, $e$ is the electronic charge, $k_n$ is the initial state and $k_{n'}$ is the final state, p is the momentum operator, $f_{kn}$ is the Fermi distribution function, The

product $\left|\left\langle kn\left|p\right|kn'\right\rangle\right|^2 f_{kn}\left(1-f_{kn'}\right)$: is the matrix element representing the probability of transition between the $k_n$ states of the valence band and the $k_{n'}$ states of the conduction band and $\hbar\omega$ is the energy of the incident photon.

The real part $\varepsilon_1(\omega)$ can be calculated from the imaginary part $\varepsilon_2(\omega)$ using the relation by Kramer-Kronig [50-51].

$$\varepsilon_1(\omega)=1+\frac{2}{\pi}T\int_0^{\infty}\frac{\omega'\varepsilon_2(\omega')}{\omega'^2-\omega^2}d\omega' \qquad \text{(IV.28)}$$

Where T is the principal value of the Cauchy integral.

Figure IV.12 illustrates the curves of the imaginary $\varepsilon_2(\omega)$ and real $\varepsilon_1(\omega)$ parts of the dielectric functions for both $Ca_5Si_2N_6$ and $Sr_5Ge_2N_6$, as a function of the photon energy in the range, 0-18eV, for three incident light polarizations along [100], [010] and [001] directions.

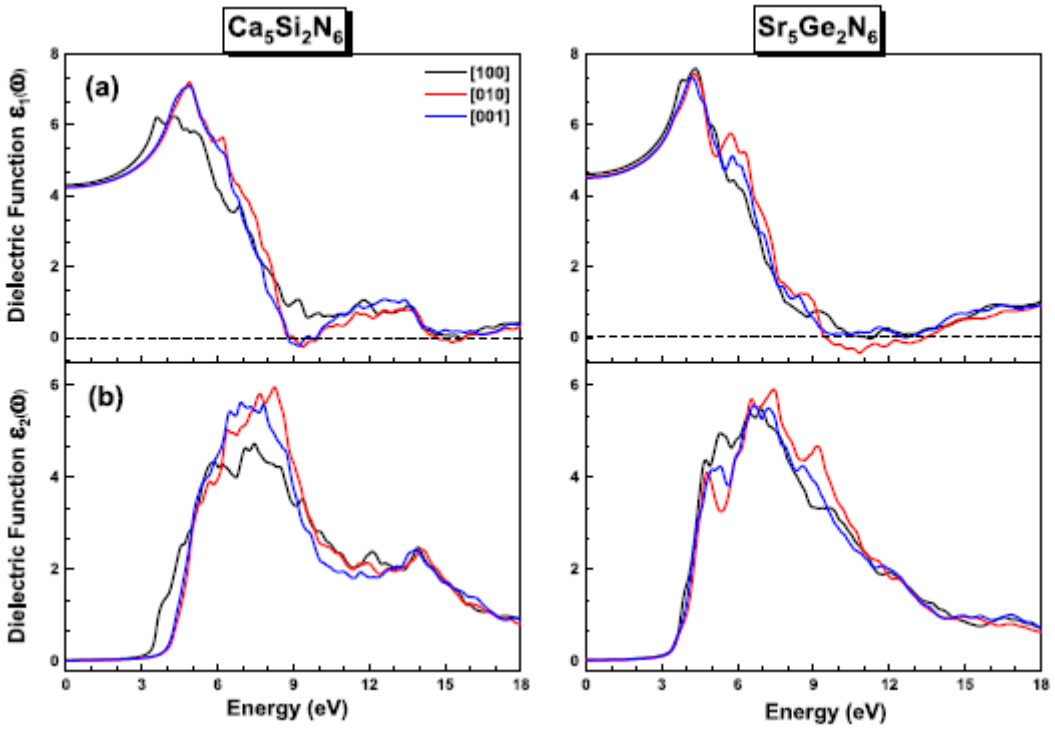


**Figure IV.12**: Calculated real $\varepsilon_1(\omega)$ and imaginary $\varepsilon_2(\omega)$ parts of the complex dielectric function for $Ca_5Si_2N_6$ and $Sr_5Ge_2N_6$ compounds for different polarizations of incident radiation.

From figure IV.12, it can be seen that the intensities and energy positions of the main peaks in $\varepsilon_2(\omega)$ and $\varepsilon_1(\omega)$ are clearly different in the three light polarizations and are smaller

for the [100] polarization. This is a clear indication that the complex dielectric functions exhibit a noticeable anisotropy for different polarizations [100], [010] and [001]. The compound $Ca_5Si_2N_6$ shows a more significant anisotropy than $Sr_5Ge_2N_6$, and even its absorption edge is slightly shifted towards low energies for the [100] polarization. Using the DOS diagrams (Fig. IV.11) and the fact that the imaginary part of the dielectric function, $\varepsilon_2(\omega)$, is proportional to the crystal absorption spectrum, it is possible to attribute the absorption peaks between 3.25 and 8 eV to the electronic transitions from the filled N-2*p* states to the empty p states of Ca/Sr, Ge/Si and N.

The static dielectric constant is the most important quantity to be studied in the dispersive $(\varepsilon_1(\omega))$ spectrum, which defined as the zero-energy value of the real part of the dielectric function: $\varepsilon_1(\omega)$: $\varepsilon_1(\omega \to 0)$. The calculated $\varepsilon_1(0)$ values for $Ca_5Si_2N_6$ ($Sr_5Ge_2N_6$) are found to be 4.31 (4.61) for the [100] polarization and 4.25 (4.53) for the other two polarizations, i.e. [010] and [001]. It should be noted that the $\varepsilon_1(0)$ values of Sr5Ge2N6 are slightly larger than those of $Ca_5Si_2N_6$. In other words, $\varepsilon_1(0)$ is inversely proportional to the band gap value, i.e. a smaller energy gap yields a larger $\varepsilon_1(0)$value. This agrees well with Penn's model [52]:

$$\varepsilon(0) \simeq 1 + \left(h\omega_p / E_g\right) \qquad \text{(IV.29)}$$

where $E_g$ and $\omega_p$ are the energy band gap and plasma frequency, respectively.

### IV.5.2. Absorption coefficient

The absorption coefficient $\alpha(\omega)$ is an important optical parameter, which evaluates the amount of energy of an electromagnetic wave of frequency ($\omega$), absorbed per unit length of a medium, where it spreads. The absorption spectrum gives useful information that can be used to evaluate certain optoelectronic devices such as sunlight converter. The absorption coefficient optical $\alpha(\omega)$ can be calculated from the dielectric function via the following expression[53]:

$$\alpha(\omega) = \frac{\sqrt{2}}{c}\omega\sqrt{-\varepsilon_1(\omega) + \sqrt{\varepsilon_1(\omega)^2 + \varepsilon_2(\omega)^2}} \qquad \text{(IV.30)}$$

Panel (a) of Fig IV.13 shows the calculated absorption spectrum of the studied compounds in an energy range up to 40 eV for three different polarizations. The absorption coefficient $\alpha(\omega)$ increases quickly when the photon energy is higher than the absorption edge, as seen in Fig. IV.13 (a). Note that absorption curves for the three different polarizations of the incident radiation start at the same absorption threshold for the $Sr_5Ge_2N_6$ compound,

which indicates that the band edge is isotropic. This is not the case for the $Ca_5Si_2N_6$ compound, where the absorption edge along the [100] starts earlier than in the other directions ([010] and [001]).

The absorption ranges from 3.6 to 35 eV, with three peaks occurring at around 8.7 eV,14.3 eV and 28.7 eV for $Ca_5Si_2N_6$, and from 3.2 to 35 eV, with also three peaks occurring at about 4.9 eV, 9.3 eV and 25.3 eV for $Sr_5Ge_2N_6$. The highest $\alpha(\omega)$ values are found in the [010] direction, reaching $2.91 \times 10^5 cm^{-1}$(25.2eV) for $Sr_5Ge_2N_6$and $4.16 \times 10^5 cm^{-1}$(28.7eV) for $Ca_5Si_2N_6$, demonstrating a significant anisotropy between [100], [010], and [001] for the two nitrides. The strong absorptive of electromagnetic waves in the ultraviolet range suggests that these compounds are suitable for UV-optoelectronic applications.

### IV.5.3. Reflectivity

Another very important parameter, is the optical reflectivity R ($\omega$), it is defined as the fraction (amount) of light reflected at an interface. The optical reflectivity R($\omega$) can be calculated from the dielectric function via the following relationship[54]:

$$R(\omega)=\left(\frac{\varepsilon_1(\omega)}{2}+\frac{\sqrt{\varepsilon_1(\omega)^2+\varepsilon_2(\omega)^2}}{2}\right)^2 \qquad \text{(IV.31)}$$

Photon energy dependency of the reflectivity $R(\omega)$ for $Ca_5Si_2N_6$ and $Sr_5Ge_2N_6$ crystals for three different light polarizations are displayed in Fig. IV.13 (b). One observes that there is clear anisotropy in the reflectivity spectra $R(\omega)$. The static reflectivity $R(0) = R(\omega \to 0)$ were about 15% and 13% for $Ca_5Si_2N_6$ and $Sr_5Ge_2N_6$, respectively. Then, the reflectivity increases with increasing photon energy to reach a maximum of $\sim 53\%$ at $\sim 29.5eV$ for$Ca_5Si_2N_6$in the [010] direction, and $\sim 37\%$ at $\sim 26.8eV$ for $Sr_5Ge_2N_6$ in the same direction. After that, the reflectivity decreases rapidly to its minimum level.

### IV.5.4. loss function

The energy-loss function L (ω) describes the energy lost by a fast electron as it passes through a homogeneous material. We have [55]:

$$L(\omega)=-\mathrm{Im}\left(\frac{1}{\varepsilon(\omega)}\right)=\frac{\varepsilon_2(\omega)}{\varepsilon_1(\omega)^2+\varepsilon_2(\omega)^2} \qquad \text{(IV.32)}$$

L (ω) =-Im(1/ ε(ω))= ε2(ω)/ ε1(ω)$^2$+ ε2(ω)$^2$

Fig. IV.13 (c) depicted the energy loss spectra dependency on the energy of incident electromagnetic radiation polarized parallel to the [100], [010] and [001] crystalline directions. Bulk plasma frequency$(\omega_p)$, which occurs when $\varepsilon_2(\omega) < 1$ and $\varepsilon_1(\omega)$ reaches the zero point, is generally considered to be the primary peak of the $L(\omega)$ spectrum [56].The energy loss function is clearly more pronounced along the [010] and [001] directions and is the weakest along the [100] direction. For radiation polarized in the [001] direction, the plasma frequency for $Ca_5Si_2N_6$ ($Sr_5Ge_2N_6$) is approximately equal to 32.52 eV (29.56eV),which is associated with the abrupt reduction in the reflectivity coefficient.

### IV.5.5. Refractive index and extinction coefficient

One of the most important optical constants is the refractive index, which in general depends on the electromagnetic wave length. In the case where an electromagnetic wave lose energy during propagation, the refractive index becomes complex. The real part of the refractive index n(ω) and the extinction coefficient k(ω) are calculated from $\varepsilon_1(\omega)$ and $\varepsilon_2(\omega)$ using the following equations [54,57]:

$$n(\omega)=\left(\frac{\varepsilon_1(\omega)}{2}+\frac{\sqrt{\varepsilon_1(\omega)^2+\varepsilon_2(\omega)^2}}{2}\right)^{\frac{1}{2}} \qquad \text{(IV.33)}$$

$$k(\omega)=\left(-\frac{\varepsilon_1(\omega)}{2}+\frac{\sqrt{\varepsilon_1(\omega)^2+\varepsilon_2(\omega)^2}}{2}\right)^{\frac{1}{2}} \qquad \text{(IV.34)}$$

Figure IV.13 (d) and (e) present the computed refractive index n(ω) and extinction coefficient k(ω) spectra for the investigated materials in the energy range from 0 to 40 eV for three polarizations of the incident electromagnetic radiation. It can be seen from Fig.5; panel (d) that $n(\omega)$ curves started from the static refractive index $n(0) = n(\omega \to 0)$, which are 2.07, 2.06 and 2.06 for $Ca_5Si_2N_6$, and 2.14, 2.12 and 2.12for $Sr_5Ge_2N_6$ along the [100], [010], and [001] directions, respectively. Then, $n(\omega)$increased with the increase of photon energy to reach a maximum value in the near-UV spectrum, which is equal to~2.72 at ~4.93 eV for $Ca_5Si_2N_6$ and ~2.80 at ~4.39 eV for $Sr_5Ge_2N_6$ for the [010] and [100] directions, respectively. It should be noted here that the more the refractive index increased in this energy range, the more the light beam was refracted. Afterwards, $n(\omega)$ decreased until it reach its minimum

value. The refractive index $n(\omega)$ spectrum has similar structures as the dispersive spectrum $\varepsilon_1(\omega)$.The attenuation of electromagnetic waves in a material is directly described by the extinction coefficient $k(\omega)$, which is also referred to as a damping constant attenuation coefficient. One notes that the zeroes of $\varepsilon_1(\omega)$ correspond to the local maximum of the extinction coefficient $k(\omega)$. By comparison, the spectra of the extinction coefficient $k(\omega)$ and the absorption $\alpha(\omega)$ are very similar.

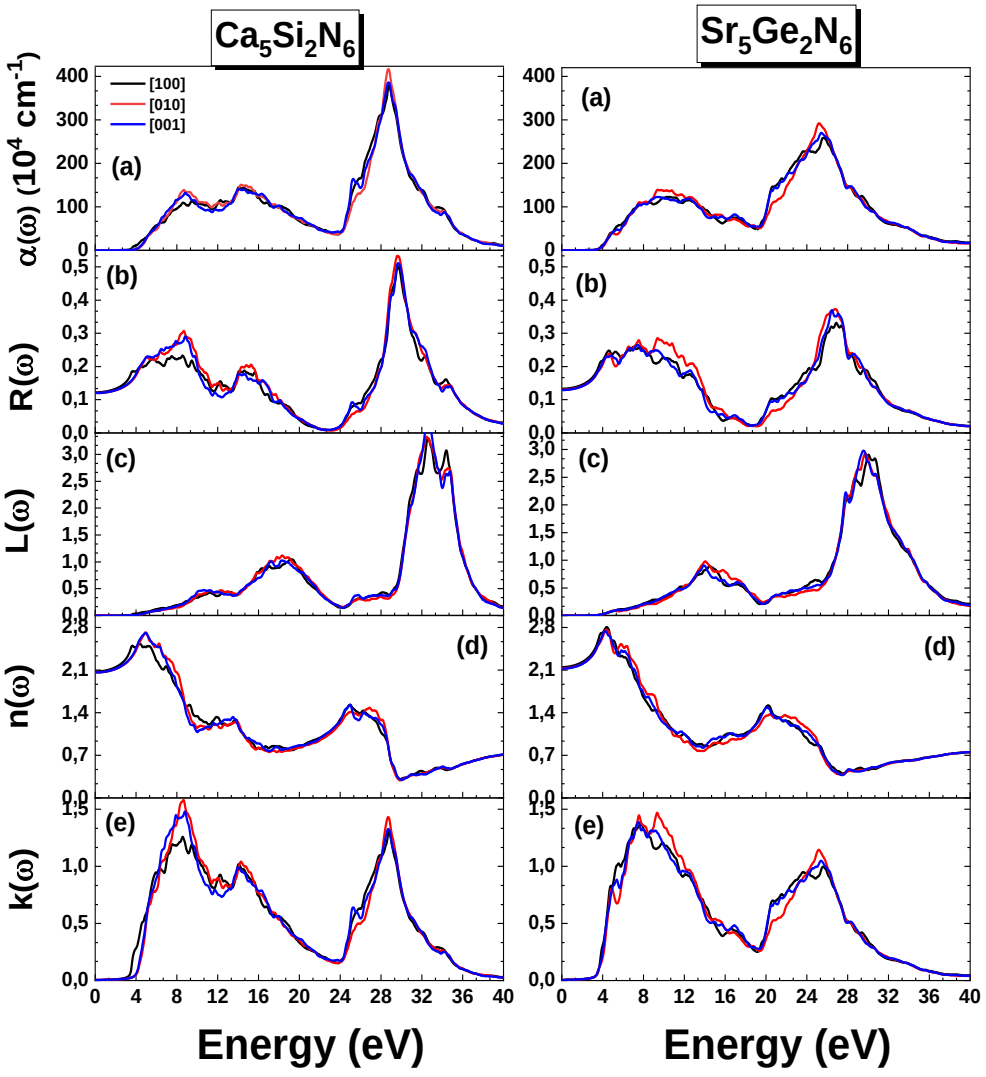


**Figure IV.13:** Calculated optical constants: Absorption coefficient $\alpha(\omega)$, reflectivity $R(\omega)$, energy loss function $L(\omega)$, refractive index $n(\omega)$ and extinction coefficient $k(\omega)$ for the $Ca_5Si_2N_6$ and $Sr_5Ge_2N_6$ nitrides for three different polarizations [100], [010] and [001].

## IV.6.Thermoelectric properties

Thermoelectric (TE) energy conversion, which includes waste heat recovery, is commonly recognized as a viable power generation technique. As a result, discovering and developing more efficient thermoelectric materials is an active area of research. The efficiency of a thermoelectric material in any power generator or cooler is assessed in terms of figure of merit ZT. The ZT value can be calculated using the formula:

$$ZT = S^2\sigma T/\kappa \qquad \text{(IV.35)}$$

where S stands for the Seebeck coefficient, $\sigma$ for electrical conductivity, T for absolute temperature and $\kappa$ for total thermal conductivity, which involves both electronic ($e$) and lattice ($l$) contributions i.e., [58-60].

$$\kappa = \kappa_e + \kappa_l \qquad \text{(IV.36)}$$

In fact, a good TE material must have a high electrical conductivity, a large Seebeck coefficient and a very low thermal conductivity at a given temperature [60]. The transport properties of the studied nitrides $Ca_5Si_2N_6$ and $Sr_5Ge_2N_6$ are explored using the BoltzTrap code along with the constant relaxation time approximation [61]. All thermoelectric parameters are estimated in this work at temperatures ranging from 200 to 900 K.

Furthermore, the band structure, carrier type, and effective mass are all factors that influence the magnitude of the thermoelectric characteristics. The carriers (holes and electrons) involved in the transport phenomenon are mainly determined by their band gap. It is observed that the application of the mBJ approach widens the band gap compared to GGA. Therefore, band gap tuning is crucial in determining the Seebeck coefficient. Metals exhibit the lowest Seebeck coefficient, whereas insulators exhibit the highest Seebeck coefficient [59]. Seebeck coefficient measures the thermoelectric voltage produced by the temperature gradient between two ends of a material [62]. The S variation with temperature is plotted in Fig IV.14. It is observed that Seebeck coefficient (S) decreases with increasing temperature for both crystals. As the temperature increases from 200 to 900 K, the value of S decreases from 1686/859 µV/K (200K) to 514/268µV/K (900 K) for $Ca_5Si_2N_6$ and $Sr_5Ge_2N_6$, respectively. For practical applications TE materials should have a Seebeck coefficient higher than $200\ \mu V/K$, which suggests the good TE behavior of the examined nitrides. Both compounds show a positive value of the Seebeck coefficient over the temperature range, indicating that the mobility of carriers is due to holes [63]. Moreover, the substitution of the Ca atom by the Sr atom has an impact on the Seebeck coefficient, for example at room

temperature, for $Ca_5Si_2N_6$ it was computed to be 1203 µV/K, while for $Sr_5Ge_2N_6$ it was evaluated to be 607 µV/K respectively.

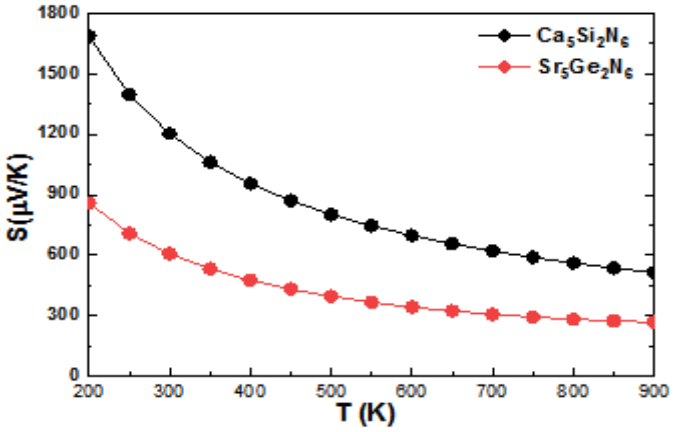


**Figure IV.14:** Calculated values of Seebeck coefficient (S), versus temperature for $Ca_5Si_2N_6$ and $Sr_5Ge_2N_6$.

The electrical conductivity $\sigma/\tau$ (where τ is the relaxation time) is an important thermoelectric factor, caused by the flow of free carriers (electrons or holes), and with increasing temperature it increases due to enhanced kinetic energy as shown in Fig. IV.15. The value of $\sigma/\tau$ for both crystals is $9.85 \times 10^{10}(\Omega ms)^{-1}$ at 200 K and becomes $1.37 \times 10^{18}(\Omega ms)^{-1}$($0{,}52 \times 10^{18}(\Omega ms)^{-1}$) for $Sr_5Ge_2N_6$ ($Ca_5Si_2N_6$) at 900K. It is clear that $Sr_5Ge_2N_6$ has a higher electrical conductivity than $Ca_5Si_2N_6$, revealing that electrons in $Sr_5Ge_2N_6$ are thermally more excited to the conduction bands than in $Ca_5Si_2N_6$. This can be attributed to the increase of ionic size from Ca to Sr, causing the bonds of the valence electrons to loosen and facilitating bond breaking with very little amount of energy. Because the band gap decreases from Ca to Sr, less excitation energy is required, and as a result, more free charge carriers are produced, which leads to an increase in electrical conductivity.

Likewise, by replacing Calcium atom with Strontium atom, S decreases because the potentials maintained across the sample edges can deteriorate as the band gap narrows, and free charge carriers increase at lower exciting energies [64-65].

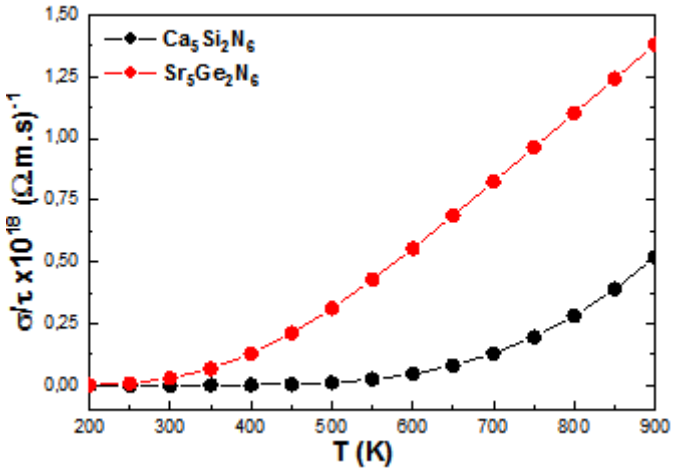


**Figure IV.15:** Calculated values of electrical conductivity ($\sigma/\tau$) versus temperature for $Ca_5Si_2N_6$ and $Sr_5Ge_2N_6$.

As mentioned above, total thermal conductivity $(\kappa/\tau)$ arises due to the contribution of electrons and phonons. Here, only the electronic contribution $(\kappa_e/\tau)$ was evaluated because of classical theory limitation [61]. Its trends as a function of T are elaborated in Fig. IV.16 which increases from 200 K and reaches to $1.29 \times 10^{14}$ W/m. K. s and $1.06 \times 10^{14}$ W/m. K. s at 900K for $Ca_5Si_2N_6$ and $Sr_5Ge_2N_6$, respectively. The Widemann-Franz law ($\kappa_e = L\sigma T$) establishes a link between electrical conductivity and thermal conductivity [65]. The ratio $\sigma/\kappa_e$ was noted to be in the order of $10^{-5}$, reflecting excellent electrical conductivity and reduced thermal conductivity [65].

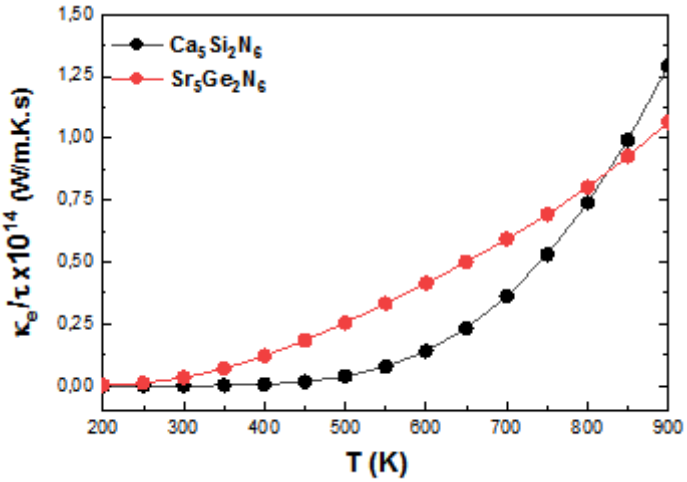


**Figure IV.16:** Calculated values of thermal conductivity ($\kappa_e/\tau$) versus temperature for $Ca_5Si_2N_6$ and $Sr_5Ge_2N_6$.

Power factor is a crucial parameter for assessing a material's efficiency for practical thermoelectric device applications. It is calculated as the product of electrical conductivity and the square of the Seebeck coefficient ($PF = S^2\sigma/\tau$) [59-60]. In Fig IV.17, the estimated PF per relaxation time for both $Ca_5Si_2N_6$ and $Sr_5Ge_2N_6$ are plotted versus temperature. The computed PF of the two nitrides under investigation improves with temperature, and at 900 is determined to be $1.37 \times 10^{11}\,W/m.K^2.s$ for $Ca_5Si_2N_6$ and $0.99 \times 10^{11}\,W/m.K^2.s$ for $Sr_5Ge_2N_6$. These compounds are useful for thermoelectric device applications because they have such a high power factor at high temperatures.

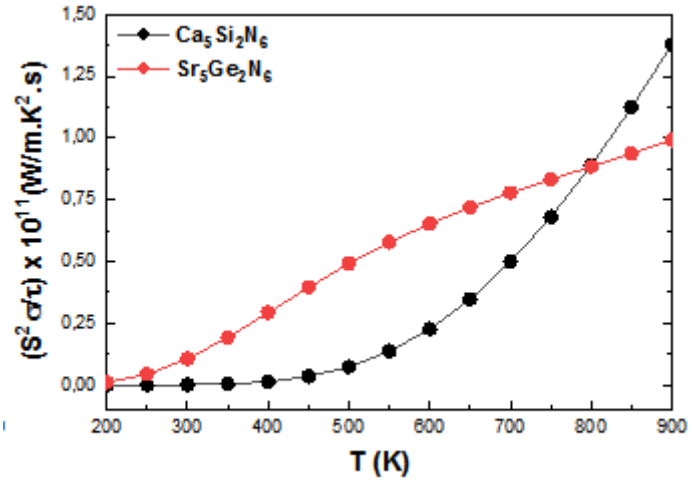


**Figure IV.17:** Calculated values of power factor ($S^2\sigma/\tau$) versus temperature for $Ca_5Si_2N_6$ and $Sr_5Ge_2N_6$.

Figure of merit (ZT) is another parameter that determines energy conversion efficiency in the thermoelectric material [60]. The calculated ZT values of these compounds are illustrated in Fig. IV.18 (a) versus T and in Fig. IV.18 (b) versus chemical potential $\mu$, respectively. At low temperature (200K), the obtained ZT values for both compounds are almost identical. In contrast, at high temperature (900K), ZT factor of $Ca_5Si_2N_6$ maintain its value, while $Sr_5Ge_2N_6$ decreases to a value of 0.84. At 300 K, the figure of merit (ZT) for $Ca_5Si_2N_6$ and $Sr_5Ge_2N_6$ is computed to be 0.986 and 0.978, respectively. Additionally, its behavior versus $\mu$ at room temperature has been plotted in Fig. IV.18 (b). In the given region of μ, ZT fluctuates and approaches the unity in both regions n and p for the two studied compounds, however these materials behave better in the p-type region as can be seen in Fig 7(b). One can speculate from these findings that the materials under investigation could have outstanding thermoelectric performance at low and room temperature.

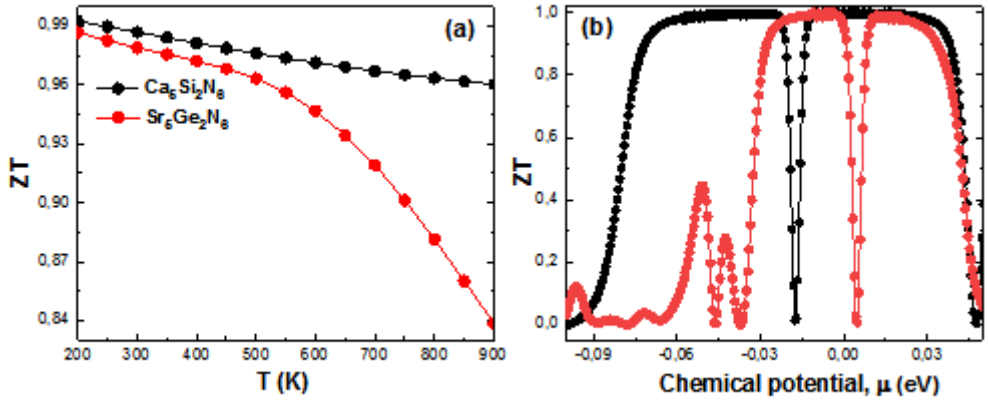


**Figure IV.18:** The calculated figure of merit ZT versus T **(a)**, and chemical potential μ **(b)** for $Ca_5Si_2N_6$ and $Sr_5Ge_2N_6$.

## IV.7.Thermodynamics properties

The study of the thermodynamic properties of materials is a necessary step in order to know their specific behavior when they undergo strong stresses of pressure or temperature. To calculate the thermodynamic properties of our compounds using the Debye's quasi-harmonic approximation. This method implemented in GIBBS program [66], Blanco and his colleagues [67-68] developed this program. Where the main input data to lunch this program are the energy and the corresponding volume E(V). These data are obtained from the optimized structure of studied compounds at different pressure values using CASTEP code. In this part, we have studied the effect of temperature and pressure on some parameters which characterize the compounds $Ca_5Si_2N_6$ and $Sr_5Ge_2N_6$, such as: the bulk modulus B, coefficient of thermal expansion α, heat capacity at constant volume $C_V$, heat capacity at constant pressure $C_P$ and the Debye temperature $\Theta_D$(K). In a pressure interval varying between 0 to 14 GPa and a temperature interval ranging from 0 to 500K.

### IV.7.1. Bulk modulus

The Figure IV.19 illustrates the variation of B as a function of pressure at different fixed temperatures (0,300 and 500 K). The bulk modulus increases almost linearly with increasing pressure. The decrease in the bulk modulus is justified by the fact that the material loses its resistance when it is heated.

Figure IV.20 represents the variation of the bulk modulus as a function of temperature at different fixed pressures (0, 4, 8.12 and 14 GPa) for $Ca_5Si_2N_6$ and $Sr_5Ge_2N_6$. It is important

to note that the bulk modulus for a fixed value of the pressure is almost constant if the temperature is below 100 K. Also, we notice that the bulk modulus decreases when the temperature increases for a given pressure.

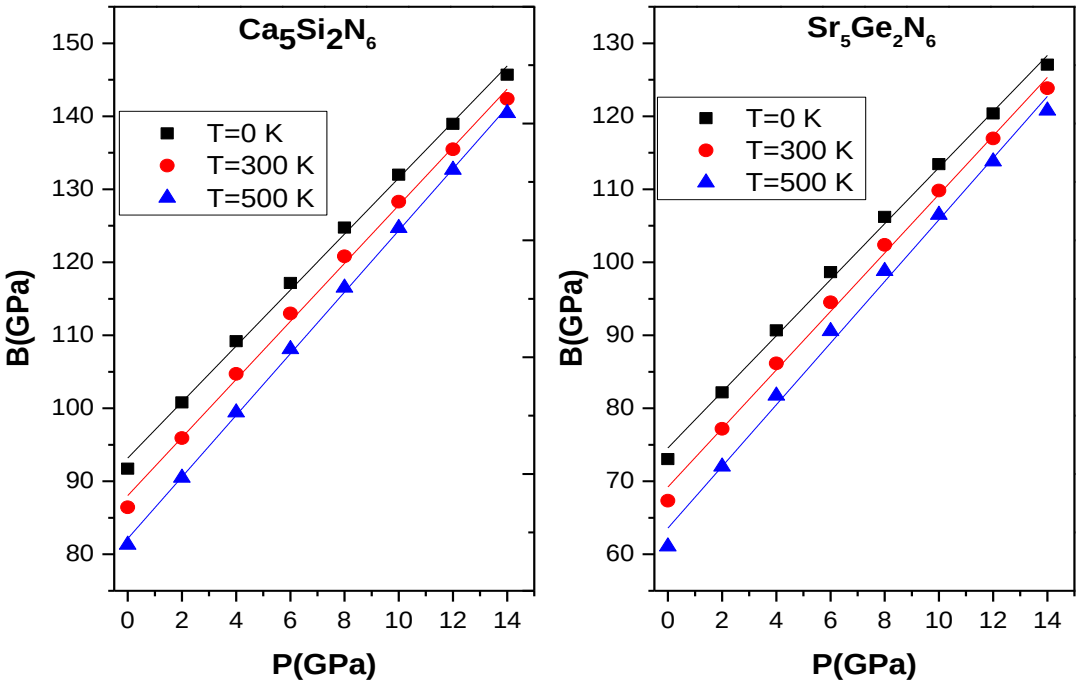


**Figure IV.19:** Variation of the bulk modulus with the pressure at different temperatures for $Ca_5Si_2N_6$ and $Sr_5Ge_2N_6$.

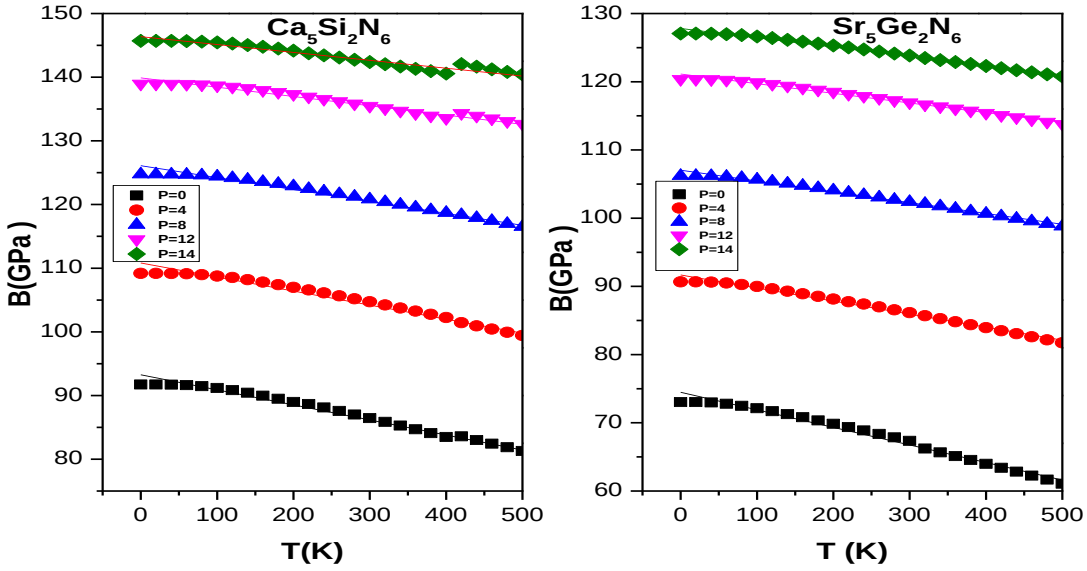


**Figure** IV.20**:** Variation of the modulus of compressibility with the temperature at different pressures for $Ca_5Si_2N_6$ and $Sr_5Ge_2N_6$.

### IV.7.2. Coefficient of thermal expansion

The thermal expansion coefficient α expresses the correspondence between the volume of the material and the temperature it undergoes, it is linked to the strength (hardness) of the atomic bonds. Strong atomic bonding results in smaller thermal expansion and high melting points. The variation of the coefficient of thermal expansion α as a function of temperature for $Ca_5Si_2N_6$ and $Sr_5Ge_2N_6$ is shown respectively in the figure IV.21.

It turns out that at a given pressure, there is a sharp increase in the coefficient of expansion with temperature in the interval 0 < T < 300K. At temperatures above 300 K, the thermal expansion increases slowly with increasing temperature and becomes almost constant (see figure IV.21). Therefore, high temperatures do not influence thermal expansion. We can also see that the thermal expansion is more sensitive to the increase in temperature for P=0 GPa. When the temperature is fixed, the thermal expansion decreases with growth pressure.

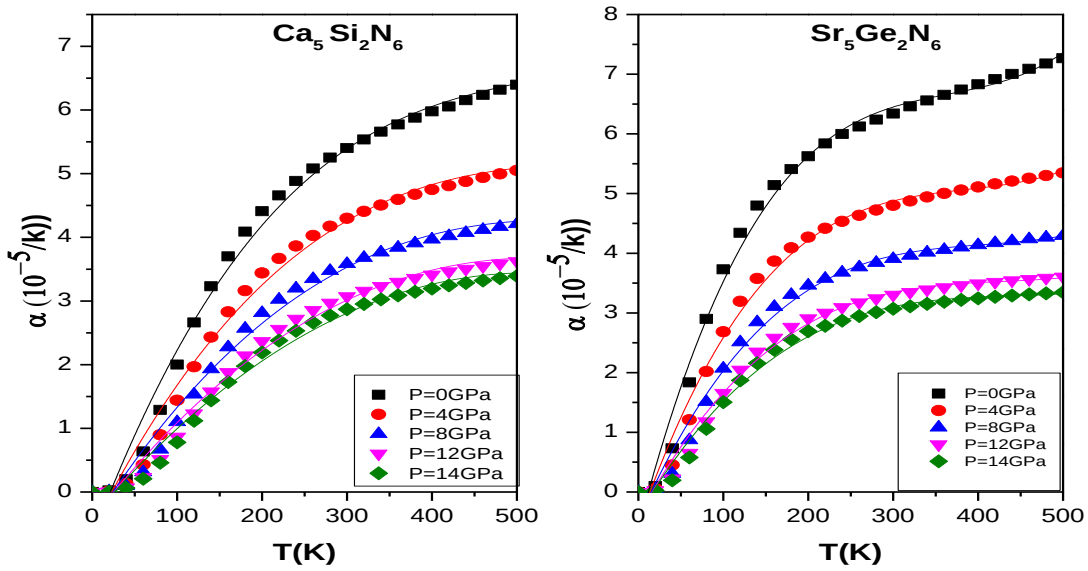


**Figure IV.21:** Variation of the coefficient of expansion α with the temperature at different pressures for $Ca_5Si_2N_6$ and $Sr_5Ge_2N_6$.

### IV.7.3. Heat Capacity

The heat capacity of materials is one of the most important thermal parameters that reflect their vibrational properties. It is the energy that must be brought to a mole of a body to increase its temperature by one Kelvin.

#### IV.7.3.a. Heat capacity at constant volume $C_V$

Figure IV.22 illustrates the variation of heat capacity at constant volume $C_V$ as a function of pressure at different fixed temperatures (200, 300 and 500 K). The heat capacity at a constant volume $C_V$ decreases linearly with increasing pressure. We also note that at a given pressure the heat capacity $C_V$ increases with the increase in the applied temperature.

The evolution of heat capacity at constant volume $C_V$ with temperature at different pressures for $Ca_5Si_2N_6$ and $Sr_5Ge_2N_6$ is shown in figure IV.23 respectively. For low temperatures (T<100 K), the increase of Cv is governed by the formula $C_v = \alpha T + \beta T^3$, increasing temperature causes a rapid increase in the value of the heat capacity at low temperatures (below 300K). It then slowly increases at high temperatures, reaching the Dulong and Petit limits ($C_v=3nN_AK_B$ where n is the number of atoms per molecule, $N_A$ the Avogadro number, and $K_B$ the Boltzmann constant).which is 616 and 635 $J.K^{-1}.Mol^{-1}$ for $Ca_5Si_2N_6$ and $Sr_5Ge_2N_6$ respectively, this behavior is common to all solids at high temperature. We also note that at a given temperature, the heat capacity $C_V$ decreases with the increase in the applied pressure.

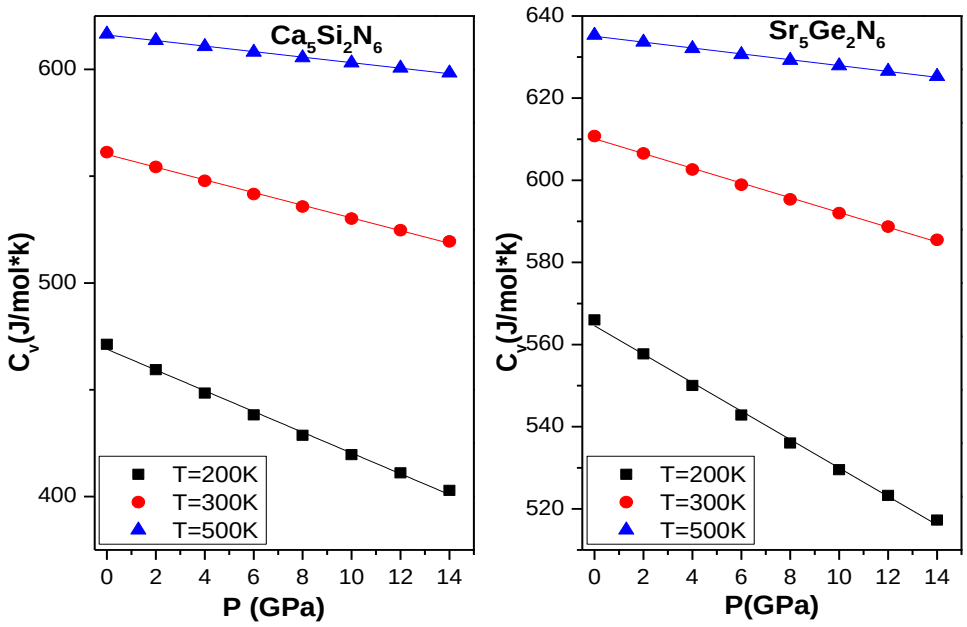


**Figure IV.22:** Variation of heat capacity $C_V$ with pressure at different temperatures for $Ca_5Si_2N_6$ and $Sr_5Ge_2N_6$.

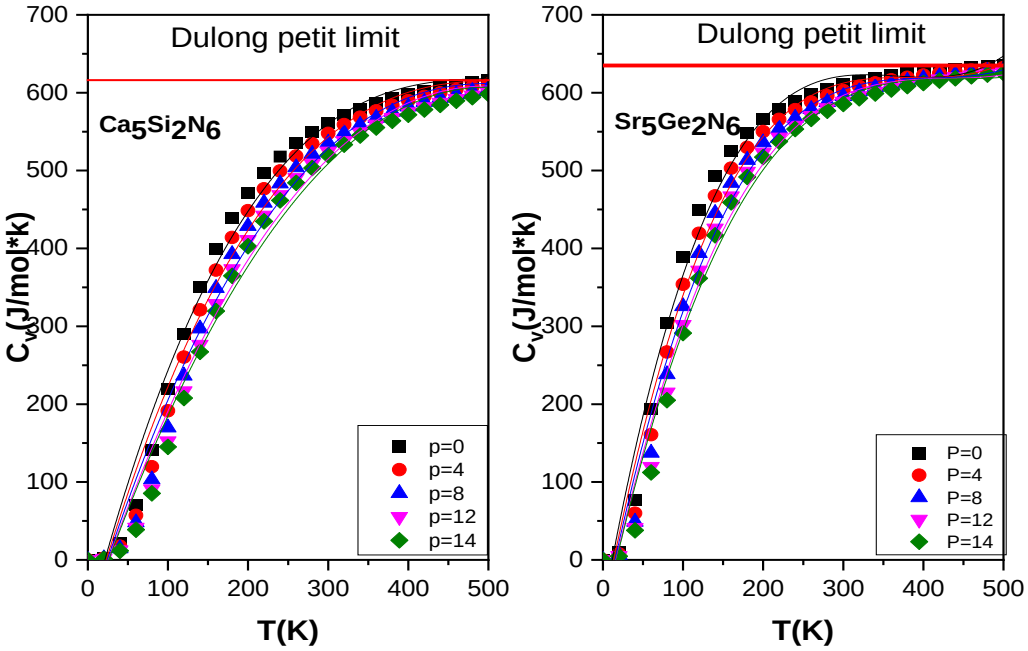


**Figure IV.23:** Variation of the heat capacity $C_V$ with the temperature at different Pressures for $Ca_5Si_2N_6$ and $Sr_5Ge_2N_6$.

### IV.7.3.b.Heat capacity at constant pressure Cp

The variation of heat capacity at constant pressure $C_P$ as a function of temperature at different pressures for $Ca_5Si_2N_6$ and $Sr_5Ge_2N_6$ is shown in Fig IV.24. At low temperatures, $C_P$ exhibits rapid variation with temperature as $C_V$ does. While for high temperatures, $C_P$ increases very slowly with increasing temperature. We see a remarkable increase in $C_P$ at temperatures above 300K. At a given temperature, the heat capacity $C_P$ decreases with increasing pressure.

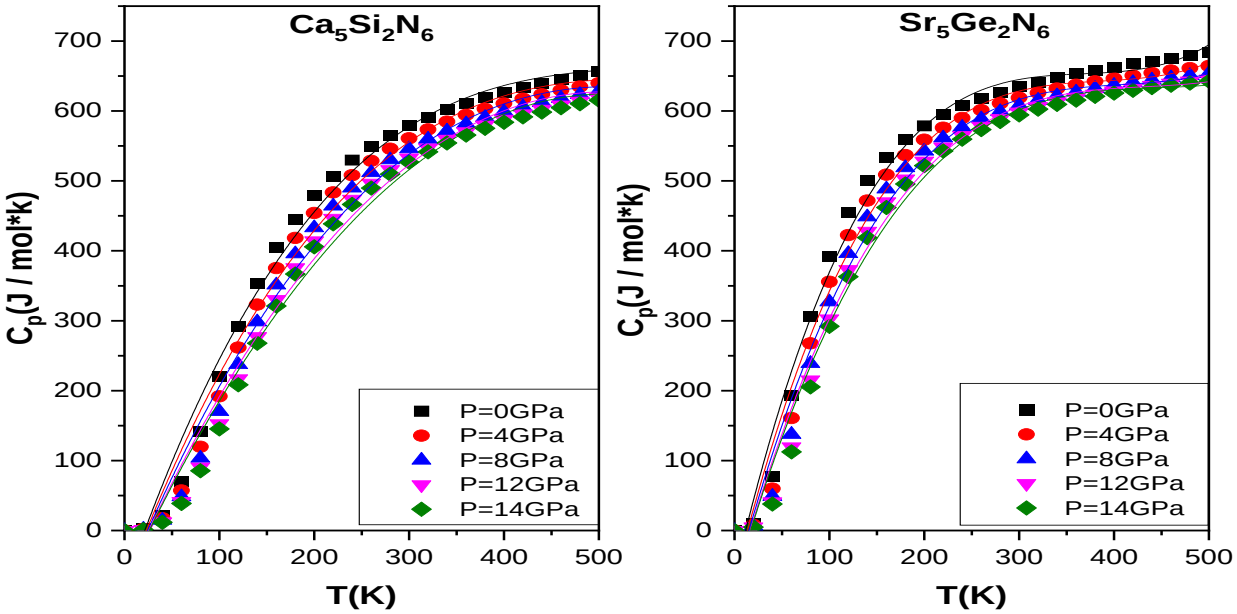


**Figure IV.24:** Variation of the heat capacity $C_p$ with the temperature at different pressures for $Ca_5Si_2N_6$ and $Sr_5Ge_2N_6$.

### IV.7.4. Debye temperature

The Debye temperature $\theta_D(K)$ is defined as the maximum temperature that can cause normal vibration of lattice atoms. The results obtained from the GIBBS program [66] for the Debye temperature at zero pressure and zero temperature, are in good agreement with those calculated from the elastic constants. This is proof that the calculations performed are reliable.

The figure IV.25 illustrates the variation of the Debye temperature as a function of the pressure at different fixed temperatures (0, 300 and 500 K) for $Ca_5Si_2N_6$ and $Sr_5Ge_2N_6$. The Debye temperature increases linearly with increasing pressure. It is also noted that at a given pressure the Debye temperature decreases with the increase in the applied temperature.

Figure IV.26 shows that for different pressure values, the Debye temperature is almost constant from 0 up to 100 K, and then it decreases almost linearly with temperature at temperatures above 200 K. We also find that when the temperature is fixed, the Debye temperature increases with the applied pressure. The behavior of the Debye temperature towards temperature and pressure is similar to that of the bulk modulus. This result is in good agreement with the fact that the Debye temperature is proportional to the bulk modulus and that a hard material exhibits a high Debye temperature. Therefore the vibration frequency of the particles changes under the effects of pressure and temperature.

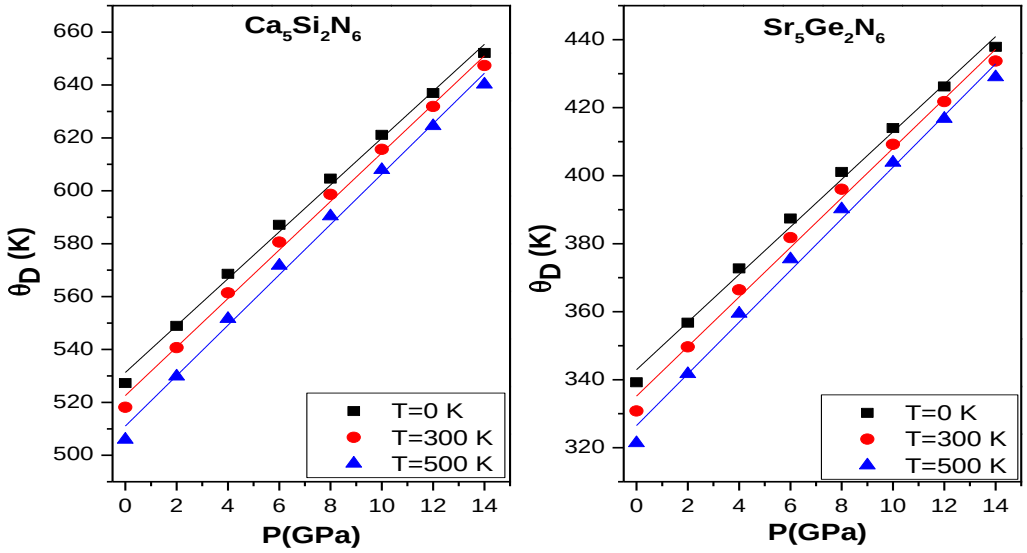


**Figure IV.25:** Variation of the Debye temperature $\theta_D(K)$ with pressure at different temperatures for $Ca_5Si_2N_6$ and $Sr_5Ge_2N_6$.

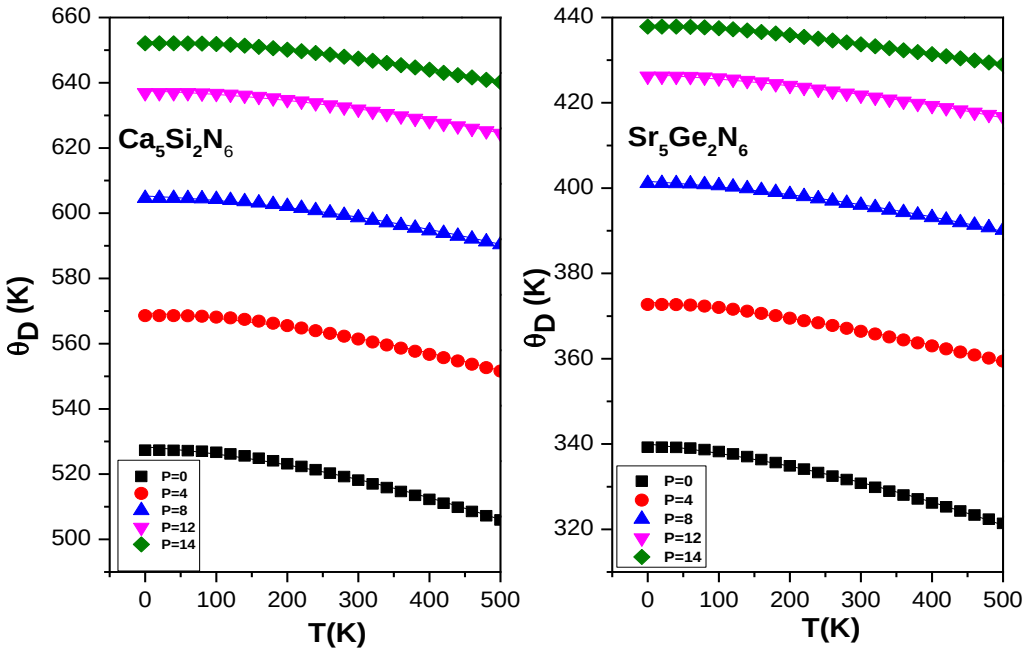


**Figure IV.26:** Variation of the Debye temperature $\theta_D(K)$ with the temperature at different pressures For $Ca_5Si_2N_6$ and $Sr_5Ge_2N_6$.

**References**

[1] Clark, S. J., Segall, M. D., Pickard, C. J., Hasnip, P. J., Probert, M. I., Refson, K., & Payne, M. C. (2005). First principles methods using CASTEP. *Zeitschrift für kristallographie-crystalline materials*, *220*(5-6), 567-570.

[2] Perdew, J. P., Ruzsinszky, A., Csonka, G. I., Vydrov, O. A., Scuseria, G. E., Constantin, L. A., ... Burke, K. (2008). Restoring the density-gradient expansion for exchange in solids and surfaces. *Physical review letters*, *100*(13), 136406.

[3] Vanderbilt, D. (1990). Soft self-consistent pseudopotentials in a generalized eigenvalue formalism. *Physical review B*, *41*(11), 7892.

[4] Pack, J. D., & Monkhorst, H. J. (1977). " Special points for Brillouin-zone integrations"—a reply. *Physical Review B*, *16*(4), 1748.

[5] Ottinger, F., & Nesper, R. (2005). Synthesis and crystal structure of the nitridosilicates Ca5 [Si2N6] and Ca7 [NbSi2N9]. *Zeitschrift für anorganische und allgemeine Chemie*, *631*(9), 1597-1602.

[6] Junggeburth, S. C., Oeckler, O., & Schnick, W. (2008). Sr5Ge2N6–A Nitridogermanate with Edge-sharing Double Tetrahedra. *Zeitschrift für anorganische und allgemeine Chemie*, *634*(8), 1309-1311.

[7] Fischer, T. H., & Almlof, J. (1992). General methods for geometry and wave function optimization. *The Journal of Physical Chemistry*, *96*(24), 9768-9774.

[8] Guechi, N., Bouhemadou, A., Khenata, R., Bin-Omran, S., Chegaar, M., Al-Douri, Y., & Bourzami, A. (2014). Structural, elastic, electronic and optical properties of the newly synthesized monoclinic Zintl phase BaIn2P2. *Solid state sciences*, *29*, 12-23.

[9] Tanaka, K., & Koiwa, M. (1996). Single-crystal elastic constants of intermetallic compounds. *Intermetallics*, *4*, S29-S39.

[10] Golesorkhtabar, R., Pavone, P., Spitaler, J., Puschnig, P., & Draxl, C. (2013). ElaStic: A tool for calculating second-order elastic constants from first principles. *Computer Physics Communications*, *184*(8), 1861-1873.

[11] Lu, G., & Zhang, L. (2012). Connecting microscopic structure and macroscopic mechanical properties of structural materials from first-principles. *Science China Physics, Mechanics and Astronomy*, *55*, 2305-2315.

[12] Boucenna, S., Haddadi, K., Bouhemadou, A., Louail, L., Soyalp, F., & Khenata, R. (2019). Elastic, electronic, chemical bonding and thermodynamic properties of the ternary nitride Ca4TiN4: Ab initio predictions. *Journal of Molecular Graphics and Modelling*, *92*, 74-85.

[13] Boucenna, S., Mosbah, A., Haddadi, K., Louail, L., Bouhemadou, A., & Uğur, G. Ö. K. A. Y. (2022). Theoretical investigation of some fundamental physical properties of the ternary nitrides Ca4SiN4 and Ca4GeN4 under pressure and temperature effect. *Computational Condensed Matter*, *32*, e00711

[14] Wu, Y., Duan, Y., Wang, X., Peng, M., Shen, L., & Qi, H. (2022). Elastic anisotropy and thermal properties of Zr-Al-N ternary nitrides using first-principles explorations. *Materials Today Communications*, *33*, 104651.

[15] Milman, V., & Warren, M. C. (2001). Elasticity of hexagonal BeO. *Journal of Physics: Condensed Matter*, *13*(2), 241.

[16] Voigt, W. J. T. L. (1928). A determination of the elastic constants for beta-quartz lehrbuch de kristallphysik. *Terubner Leipzig*, *40*, 2856-2860.

[17] Reuss, A. (1929). Berechnung der fließgrenze von mischkristallen auf grund der plastizitätsbedingung für einkristalle. *ZAMM-Journal of Applied Mathematics and Mechanics/Zeitschrift für Angewandte Mathematik und Mechanik*, *9*(1), 49-58.

[18] Hill, R. (1952). The elastic behaviour of a crystalline aggregate. *Proceedings of the Physical Society. Section A*, *65*(5), 349.

[19] Wu, Z. J., Zhao, E. J., Xiang, H. P., Hao, X. F., Liu, X. J., & Meng, J. (2007). Crystal structures and elastic properties of superhard Ir N 2 and Ir N 3 from first principles. *Physical Review B*, *76*(5), 054115.

[20] Pugh, S. F. (1954). XCII. Relations between the elastic moduli and the plastic properties of polycrystalline pure metals. *The London, Edinburgh, and Dublin Philosophical Magazine and Journal of Science*, *45*(367), 823-843.

[21] Frantsevich, I. N., Voronov, F. F., & Bokuta, S. A. (1983). Elastic Constants and Elastic Moduli of Metals and Insulators ed IN Frantsevich (Kiev).

[22] Vaitheeswaran, G., Kanchana, V., Svane, A., & Delin, A. (2007). Elastic properties of MgCNi3—a superconducting perovskite. *Journal of Physics: Condensed Matter*, *19*(32), 326214.

[23] Savin, A., Flad, H. J., Flad, J., Preuss, H., & von Schnering, H. G. (1992). On the bonding in carbosilanes. *Angewandte Chemie International Edition in English*, *31*(2), 185-187.

[24] Anderson, O. L. (1963). A simplified method for calculating the Debye temperature from elastic constants. *Journal of Physics and Chemistry of Solids*, *24*(7), 909-917.

[25] Schreiber, E., Anderson, O. L., Soga, N., & Bell, J. F. (1975). Elastic constants and their measurement.

[26] Qin, X., Liu, X., Huang, W., Bettinelli, M., & Liu, X. (2017). Lanthanide-activated phosphors based on 4f-5d optical transitions: theoretical and experimental aspects. *Chemical reviews*, *117*(5), 4488-4527.

[27] Wang, Z., Chu, I. H., Zhou, F., & Ong, S. P. (2016). Electronic structure descriptor for the discovery of narrow-band red-emitting phosphors. *Chemistry of materials*, *28*(11), 4024-4031.

[28] Brgoch, J., DenBaars, S. P., & Seshadri, R. (2013). Proxies from ab initio calculations for screening efficient Ce3+ phosphor hosts. *The Journal of Physical Chemistry C*, *117*(35), 17955-17959.

[29] Denault, K. A., Brgoch, J., Kloß, S. D., Gaultois, M. W., Siewenie, J., Page, K., & Seshadri, R. (2015). Average and local structure, Debye temperature, and structural rigidity in some oxide compounds related to phosphor hosts. *ACS applied materials & interfaces*, *7*(13), 7264-7272.

[30] Zhuo, Y., Mansouri Tehrani, A., Oliynyk, A. O., Duke, A. C., & Brgoch, J. (2018). Identifying an efficient, thermally robust inorganic phosphor host via machine learning. *Nature communications*, *9*(1), 4377.

[31] Jiang, L., Jiang, X., Lv, G., & Su, Y. (2022). A mini review of machine learning in inorganic phosphors. *J. Mater. Inf.*, *2*(3), 14.

[32] Ravindran, P., Fast, L., Korzhavyi, P. A., Johansson, B., Wills, J., & Eriksson, O. (1998). Density functional theory for calculation of elastic properties of orthorhombic crystals: Application to TiSi 2. *Journal of Applied Physics*, *84*(9), 4891-4904.

[33] Tang, S., Li, Y., Gao, Y., Zheng, Q., Liu, Z., & Ren, X. (2018). First-Principles investigations of the structural, anisotropic mechanical, thermodynamic and electronic properties of the AlNi2Ti compound. *Crystals*, *8*(2), 93.

[34] Ranganathan, S. I., & Ostoja-Starzewski, M. (2008). Universal elastic anisotropy index. *Physical review letters*, *101*(5), 055504.

[35] Luan, S., Dong, L., & Jia, R. (2019). Analysis of the structural, anisotropic elastic and electronic properties of β-Ga2O3 with various pressures. *Journal of Crystal Growth*, *505*, 74-81.

[36] Niklaus, R., Minár, J., Strobel, P., Schmidt, P. J., & Schnick, W. (2019). Ab initio exploration and prediction of AE-containing nitrido (litho/magneso) tetrelates (AE= Ca, Sr; Tt= Si, Ge) with [Si 2 N 6] 10− or [Ge 2 N 6] 10− units. *Dalton Transactions*, *48*(24), 8671-8677.

[37] Perdew, J. P., & Levy, M. (1983). Physical content of the exact Kohn-Sham orbital energies: band gaps and derivative discontinuities. *Physical Review Letters*, *51*(20), 1884

[38] Sham, L. J., & Schlüter, M. (1983). Density-functional theory of the energy gap. *Physical review letters*, *51*(20), 1888.

[39] Mori-Sánchez, P., Cohen, A. J., & Yang, W. (2008). Localization and delocalization errors in density functional theory and implications for band-gap prediction. *Physical review letters*, *100*(14), 146401.

[40] Koller, D., Blaha, P., & Tran, F. (2013). Hybrid functionals for solids with an optimized Hartree–Fock mixing parameter. *Journal of Physics: Condensed Matter*, *25*(43), 435503.

[41] Shishkin, M., & Kresse, G. (2007). Self-consistent G W calculations for semiconductors and insulators. *Physical Review B*, *75*(23), 235102.

[42] Koller, D., Tran, F., & Blaha, P. (2011). Merits and limits of the modified Becke-Johnson exchange potential. *Physical Review B*, *83*(19), 195134.

[43] Koller, D., Tran, F., &Blaha, P. (2012). Improving the modified Becke-Johnson exchange potential. *Physical Review B*, *85*(15), 155109.

[44] Blaha, P., Schwarz, K., Madsen, G. K. H., Kvasnicka, D., &Luitz, J., (2013). *WIEN2k: An Augmented Plane Wave Plus Local Orbitals Program for Calculating Crystal Properties*. University Karlheinz Schwarz.

[45] Duan, C. J., Wang, X. J., Otten, W. M., Delsing, A. C., Zhao, J. T., & Hintzen, H. T. (2008). Preparation, electronic structure, and photoluminescence properties of Eu2+-and Ce3+/Li+-activated alkaline earth silicon nitride MSiN2 (M= Sr, Ba). *Chemistry of materials*, *20*(4), 1597-1605.

[46] Huang, J., Jiang, T., Yao, N., Li, H., & Xu, X. (2015). Synthesis and Characterization of Novel Nitride Phosphors Ca 5 Si 2 N 6: Eu 2+/Ce 3+. *Asian Journal of Chemistry*, *27*(3).

[47]Dadsetani, M., & Pourghazi, A. (2006). Optical properties of strontium monochalcogenides from first principles. *Physical Review B*, *73*(19), 195102.

[48] Philipp, H. R., & Ehrenreich, H. (1963). Optical properties of semiconductors. *Physical Review*, *129*(4), 1550-1560.

[49] Ambrosch-Draxl, C., & Sofo, J. O. (2006). Linear optical properties of solids within the full-potential linearized augmented planewave method. *Computer physics communications*, *175*(1), 1-14.

[50] Lucarini, V., Saarinen, J. J., Peiponen, K. E., & Vartiainen, E. M. (2005). *Kramers-Kronig relations in optical materials research* (Vol. 110). Springer Science & Business Media.

[51] Kronig, R. D. L. (1926). On the theory of dispersion of x-rays. *Josa*, *12*(6), 547-557.

[52] Penn, D. R. (1962). Wave-number-dependent dielectric function of semiconductors. *Physical review*, *128*(5), 2093.

[53] Fox, M. (2001). Classical propagation. *Optical properties of solids*, *2*, 28-58.

[54] Wooten, F. (1972). *Optical properties of solids*. Academic Press.

[55] Amin, B., Ahmad, I., Maqbool, M., Goumri-Said, S., & Ahmad, R. (2011). Ab initio study of the bandgap engineering of Al1− xGaxN for optoelectronic applications. Journal of Applied Physics, 109(2).

[56] Li, C., Wang, Z., & Wang, C. (2011). First-principles study of the structural, elastic, electronic and optical properties of the monoclinic BiScO3. *Physica B: Condensed Matter*, *406*(10), 2028-2032.

[57] Amin, B., Ahmad, I., Maqbool, M., Goumri-Said, S., & Ahmad, R. (2011). Ab initio study of the bandgap engineering of Al1− xGaxN for optoelectronic applications. Journal of Applied Physics, 109(2).

[58] Kangsabanik, J., & Alam, A. (2019). High-performance ternary alkali nitrides for renewable energy applications. *Physical Review Materials*, *3*(10), 105405.

[59] Gorai, P., Stevanović, V., & Toberer, E. S. (2017). Computationally guided discovery of thermoelectric materials. *Nature Reviews Materials*, *2*(9), 1-16

[60] Lu, N., & Ferguson, I. (2013). III-nitrides for energy production: photovoltaic and thermoelectric applications. *Semiconductor Science and Technology*, *28*(7), 074023.

[61] Madsen, G. K., & Singh, D. J. (2006). BoltzTraP. A code for calculating band-structure dependent quantities. *Computer Physics Communications*, *175*(1), 67-71.

[62] Zhang, X., & Zhao, L. D. (2015). Thermoelectric materials: Energy conversion between heat and electricity. *Journal of Materiomics*, *1*(2), 92-105.

[63] Wu, G., & Yu, X. (2020). Contributions of chemical potential to the diffusive Seebeck coefficient for bulk semiconductor materials. *The European Physical Journal Plus*, *135*(6), 1-15.

[64] Alburaih, H. A., Aman, S., Mehmood, S., Ali, Z., Ejaz, S. R., Khosa, R. Y., & Farid, H. M. T. (2022). First principle study of opto-electronic and thermoelectric properties of Zintl Phase XIn2Z2 (X= Ca, Sr and Z= As, Sb). *Applied Physics A*, *128*(5), 451.

[65] Behera, D., Sharma, R., Ullah, H., Waheed, H. S., & Mukherjee, S. K. (2022). Electronic, optical, and thermoelectric investigations of Zintl phase AAg2Se2 (A= Sr, Ba) compounds: A first-principle approach. *Journal of Solid State Chemistry*, *312*, 123259.

[66] Blanco, M. A., Francisco, E., & Luana, V. (2004). GIBBS: isothermal-isobaric thermodynamics of solids from energy curves using a quasi-harmonic Debye model. *Computer Physics Communications*, *158*(1), 57-72.

[67] Blanco, M. A., Francisco, E., & Luana, V. (2004). GIBBS: isothermal-isobaric thermodynamics of solids from energy curves using a quasi-harmonic Debye model. *Computer Physics Communications*, *158*(1), 57-72.

[68] Blanco, M. A., Pendás, A. M., Francisco, E., Recio, J. M., & Franco, R. (1996). Thermodynamical properties of solids from microscopic theory: applications to MgF2 and Al2O3. *Journal of Molecular Structure: THEOCHEM*, *368*, 245-255.

# GENERAL CONCLUSION

Density functional theory based on two complementary codes is used for a complete check of structural parameters, elasticity, electronic, optical, thermoelectric and thermodynamic properties for $Ca_5Si_2N_6$ and $Sr_5Ge_2N_6$ materials. The first part of this work, namely structural optimization and elastic constants, was done by the psedopetential plane wave method (PP-PW) as implemented in CASTEP code. The second part in this work namely electronic and optic, was performed via the full potential-linearized augmented plane wave (FP-LAPW) method as implemented in the WIEN2k package. Using BoltzTraP program and the FP-LAPW density of states, we have calculated the thermoelectric properties of both compounds. Finally, thermodynamic properties are also predicted by the combination of GIBBS program and the pseudopotential plane waves of E-V results. Our main conclusions are the following:

- ✓ Our results of the geometry optimization show a good agreement with the available experimental ones. Generally, the deviation between the lattice parameters (a, b, c and $\beta$) is less 0.8%. To examine the stability of the present compounds, we have calculated the cohesive energies, the enthalpies of formation and phonon dispersion. All of these quantities confirm the chemical and structural stabilities of the $Ca_5Si_2N_6$ and $Sr_5Ge_2N_6$ compounds. The effect of pressure on the structural parameters shows that the [010] direction is more compressible than the [001] and [100] directions. The calculated elastic constants $C_{ij}$ for both considered materials satisfy the mechanical stability criteria for monoclinic structures. Moreover, the obtained values of Cij show that $C_{33} > C_{11} > C_{22}$, suggesting that the crystal structures of $Ca_5Si_2N_6$ and $Sr_5Ge_2N_6$ should be more easily compressible along the b-axis ([010]) than along the a- ([001]) and ([100]) c-axes. These results are in agreement with those obtained from the pressure effect on structural properties. Using Hill's assumption we have calculated the polycrystalline elastic moduli. The bulk modulus (B) values obtained from the ones derived from the calculated single-crystal elastic constants are in good agreement with to those calculated from the EOS fitting. The isotropic elastic module B, G and Young's modulus (E) has relatively large values, reflecting the high stiffness of the considered materials. The examined compounds have Pugh's ratios greater than 1.75, indicating that these materials are ductile and will be resistant to thermal shocks. The Poisson's ratio $\upsilon$ values of $Ca_5Si_2N_6$ and $Sr_5Ge_2N_6$ are equal to 0.29 and 0.30, implying again their ductile nature. This good agreement confirms the reliability and accuracy of the current calculations. Elastic

anisotropy of these compounds were investigated through different approaches, the obtained results for both studied materials suggest a pronounced elastic anisotropy.

- ✓ It is well known that the GGA/ LDA approaches are usually underestimate the band gap value Therefore, to improve the calculated band structures of the investigated compounds, the TB-mBJ functional was used to model the exchange-correlation potential. Our calculations within the GGA-PBE yielded an indirect band gap (V- Γ) of 2.29 eV and 1.47 eV for both $Ca_5Si_2N_6$ and $Sr_5Ge_2N_6$ respectively. The results of the band structure based on the TB-mBJ exchange potential are nearly identical to those of the GGA-PBEsol ones, with a distinct variation in their band gap values. The band gap energy shifted from indirect to direct (V→V) for $Ca_5Si_2N_6$ at a value of 3.55 eV. Unlike $Sr_5Ge_2N_6$, the band gap remains indirect but with a value of 3.15 eV. Substitution with heavier cations leads to narrowing the Eg value and reducing the $\theta_D$ value. To shed light on the electronic properties of $Ca_5Si_2N_6$ and $Sr_5Ge_2N_6$, the diagrams of total and atomic site projected densities of states (TDOS and PDOS) have been plotted. The investigated nitridosilicate compound can be used as a phosphor material because of its values of band gap and Debye temperature which are within the recommended range.
- ✓ Optical properties were calculated based on the band structure obtained using the TB-mBJ. the absorptive and dispersive parts of the dielectric function, absorption coefficient, refractive index, extinction coefficient, optical reflectivity and energy-loss function spectra were calculated for different polarizations [100], [010] and [001]. As first observation, the noticeable anisotropy exhibited by the complex dielectric functions along the different polarizations [100], [010] and [001]. Moreover, partial density of states were used to assign the origins of possible electronic transitions. The highest α (ω) values are found in the [010] direction, reaching $2.91 \times 10^5$ $cm^{(-1)}$ at 25.2eV for $Sr_5Ge_2N_6$ and $4.16\times10^5$ $cm^{(-1)}$ at 28.7eV for $Ca_5Si_2N_6$. The strong absorptive of electromagnetic waves in the ultraviolet range suggests that these compounds are suitable for UV-optoelectronic applications.
- ✓ The transport properties of the studied nitrides $Ca_5Si_2N_6$ and $Sr_5Ge_2N_6$ are explored using the BoltzTrap package. All thermoelectric parameters are estimated in this work at temperatures ranging from 200 to 900 K. The obtained results reveal:
  - That Seebeck coefficient (S) decreases with increasing temperature for both crystals.
  - The value of S decreases from 1686/859 μV/K (200K) to 514/268μV/K (900 K) for $Ca_5Si_2N_6$ and $Sr_5Ge_2N_6$, respectively. For practical applications TE materials should

have a Seebeck coefficient higher than 200 μV/K, which suggests the good TE behavior of the examined nitrides.

- Both compounds show a positive value of the Seebeck coefficient over the temperature range, indicating that the mobility of carriers is due to holes.
- The value of the electrical conductivity $\sigma/\tau$ for both crystals is $9.85 \times 10^{10}(\Omega ms)^{-1}$at 200K becomes $1.37 \times 10^{18}(\Omega ms)^{-1}$($0{,}52 \times 10^{18}(\Omega ms)^{-1}$) for $Sr_5Ge_2N_6$ ($Ca_5Si_2N_6$) at 900K. $Sr_5Ge_2N_6$ has a higher electrical conductivity than $Ca_5Si_2N_6$ revealing that electrons in $Sr_5Ge_2N_6$ are thermally more excited to the conduction bands than in $Ca_5Si_2N_6$.
- The ratio $\sigma/\kappa_e$ was calculated to be in the order of $10^{-5}$, reflecting the excellent electrical conductivity and the reduced thermal conductivity.
- $Ca_5Si_2N_6$ and $Sr_5Ge_2N_6$ compounds are useful for thermoelectric device applications because they have such a high power factor at high temperatures.
- The large figure of merit (ZT) values of these ternary nitrides, suggests their potential use in thermoelectric devices, especially at low and room temperature.

✓ Using Debye's quasi-harmonic model, we have explored the thermodynamic properties of $Ca_5Si_2N_6$ and $Sr_5Ge_2N_6$ under the effect of temperature from 0 to 500K, and the pressure between 0 and 14 GPa. The obtained results show that the bulk modulus increases almost linearly with increasing pressure, and decreases when the temperature increases for a given pressure.For low temperatures heat capacity follows this low $Cv = \alpha T + \beta T^3$. The increase in temperature causes a rapid increase in the value of the heat capacity at low temperatures (below 300K). Then it increases slowly at high temperatures approaching the Dulong and Petit limit ($CV \approx 3nR$) which is 616 and 635 $J.K^{-1}.Mol^{-1}$ for $Ca_5Si_2N_6$ and $Sr_5Ge_2N_6$ respectively, this behavior is common to all solids at high temperature. The results obtained from the GIBBS program for the Debye temperature at zero pressure and zero temperature, are in good agreement with those calculated from the elastic constants. For a given temperature, the Debye temperature increases with the applied pressure.

Journal of Physics and Chemistry of Solids 179 (2023) 111405

Contents lists available at ScienceDirect

Journal of Physics and Chemistry of Solids

journal homepage: www.elsevier.com/locate/jpcs

# Elastic, electronic, optical and thermoelectric properties of $Ca_5Si_2N_6$ and $Sr_5Ge_2N_6$ ternary nitrides

L. Debache [a,b], Y. Medkour [a,b,**], F. Djeghloul [a,c], K. Haddadi [b], S. Berri [d], M. Kharoubi [a,c], N. Bouarissa [e,*], N. Guechi [a,f], A. Roumili [a,b]

[a] Laboratory for Studies of Surfaces and Interfaces of Solid Materials (LESIMS), Ferhat ABBAS University Setif1, Setif, Algeria
[b] Department of Physics, Faculty of Sciences, Ferhat ABBAS University Setif1, Setif, Algeria
[c] Department of Basic Education in Technology, Ferhat ABBAS University Setif1, Setif, Algeria
[d] Department of Physics, Faculty of Science, University of M'sila, 28000, M'sila, Algeria
[e] Laboratory of Materials Physics and Its Applications, University of M'sila, 28000, M'sila, Algeria
[f] Faculty of Medicine, University Ferhat Abbas Setif 1, Setif, 19000, Algeria

ARTICLE INFO

*Keywords:*
Ternary nitrides
Ab initio
Semiconductors
Thermoelectric
Elastic constants

ABSTRACT

In order to expand the scope of application of ternary nitrides and explore more thoroughly their potential as novel materials, ab initio calculations founded on density functional theory are executed to examine the mechanical, electronic, optical and transport properties of $Ca_5Si_2N_6$ and $Sr_5Ge_2N_6$ nitrides. These compounds are thermodynamically stable established on coherent energy and enthalpy of formation, with $Ca_5Si_2N_6$ having the best stability. The estimated values of elastic constants and their derived properties suggest that the items under examination are mechanically stable, ductile and elastically anisotropic. Electronic properties have been evaluated using the GGA and TB-mBJ exchange-correlation potentials. The band structure calculated via TB-mBJ reveals that these nitrides are semiconductors, where $Ca_5Si_2N_6$ has a direct energy gap of 3.55 eV and $Sr_5Ge_2N_6$ an indirect band-gap of 3.15 eV. By combining Debye temperature and band-gap values, it was concluded that the nitridosilicate compound can be used as phosphor material. According to the optical response, which was examined in terms of dielectric function, complex refractive index, absorption, reflectivity and energy damage function, the potential applications of $Ca_5Si_2N_6$ and $Sr_5Ge_2N_6$ have been discussed. Further, thermoelectric properties are computed utilizing the semi-classical Boltzmann transport notion. The obtained results show a large strength operator and depressed thermal conductivity driving to rising figure of merit values, particularly at 300 K (0.978–0.986), signifying that the studied ternary nitrides are favorable nominees for thermoelectric employments at both low and room temperatures.

## 1. Introduction

Over the different few contracts, a considerable variety of solid-state nitride materials were synthesized and exploited in many novel technologies, including innovations revolving around photovoltaic solar cells, lithium-ion batteries, thermo-electrics, elevated-temperature ceramics or optoelectronics [1–6]. With respect to reducing global energy consumption, different classes of nitrides exhibit luminescence possessions onto doping with rare earth ions such as $Eu^{2+}$ or $Ce^{3+}$, making them suitable as shining substances for light emitting diodes (LEDs) [7–11]. Herein, for example, two subclasses -nitridosilicates and nitridoaluminates-are widely used as steward structures for bright substances (i.e. LED phosphors) because of their large structural variety, chemical and optical properties [10,12–14]. Especially, the $Eu^{2+}$- doped $M_xSi_yN_z$ nitridosilicates phosphors (M = alkali, alkaline earth or rare earth) such as: $Sr_2Si_5N_8$:$Eu^{2+}$ [15], $(A)_2Si_5N_8$ (A = Ca, Sr, Ba):$Eu^{2+}$ [16], (A)(R)$Si_4N_7$:$Eu^{2+}$ (A = Ca, Sr, Ba; R = Sc, Y, Lu) [17,18], $BaSi_7N_{10}$:$Eu^{2+}$ [19] and (A)$SiN_2$:$Eu^{2+}$ (A = Ca, Sr, Ba) [20,21]. Furthermore, the latter compositional range can be further extended by substituting Al and O for Si and N respectively [22], out coming in phosphors like $CaAlSiN_3$:$Eu^{2+}$ [23], $Ba_3Si_6O_{12}N_2$:$Eu^{2+}$ [24], $(A)Si_2O_2N_2$:$Eu^{2+}$ (A = Ca, Sr, Ba) [25], Sr $[LiAl_3N_4]$:$Eu^{2+}$ [14] and $A[Mg_2Al_2N_4]$:$Eu^{2+}$ (A = Ca, Sr, Ba) [26].

* Corresponding author.
** Corresponding author. Laboratory for Studies of Surfaces and Interfaces of Solid Materials (LESIMS), Ferhat ABBAS University Setif1, Setif, Algeria.
*E-mail addresses:* you_med2000@univ-setif.dz (Y. Medkour), N_bouarissa@yahoo.fr (N. Bouarissa).

https://doi.org/10.1016/j.jpcs.2023.111405
Received 14 February 2023; Received in revised form 13 April 2023; Accepted 22 April 2023
Available online 29 April 2023

Newly, a fresh red phosphor, $Ca_5Si_2N_6$: $Eu^{2+}$, is discovered by Huang et al. [27]. This phosphor has an excitation band that extends from 350 to 480 nm, who manufactures it charming for implementation in phosphor-transformed to light-emitting diode [27]. Structurally, $Ca_5Si_2N_6$ includes pairs of edge-proportion tetrahedra of $[Si_2N_6]^{10-}$ identical to the formerly specified in other nitridosilicates like: $Ba_5Si_2N_6$ or $Ca_7NbSi_2N_9$ [28]. Comparable "bow-tie" units of $[Ge_2N_6]^{10-}$ were found in $Sr_5Ge_2N_6$, suggests the presence of structural relations between nitridosilicates and nitridogermanates [29].

Due to technological uses for these materials, e. g. as nonlinear optical materials or efficient luminescent materials for phosphor converted light-emitting diodes (pc-LEDs), solar absorbers, and thermoelectric devices [1,2,6–8,10,27], we have decided to study the recently discovered nitridogermanate $Sr_5Ge_2N_6$ [29] and its nitridosilicate isotope, $Ca_5Si_2N_6$ [28]. Aside from their synthesis and structural characterization [28,29], the essential materialistic possessions of these nitrides have not so far been investigated, either theoretically or experimentally. These facts stimulate us to conduct a thorough investigation on their fundamental physical properties which are crucial to identify the potential of using these compounds in technological implementations. Therefore, in the present application, mechanical, optoelectronic and thermoelectric properties of $Ca_5Si_2N_6$ and $Sr_5Ge_2N_6$ nitrides were investigated in detail using accurate first-principles calculation. This work is structured as follows; computational methods are sited in section 2. Results and discussions are done in section 3. Section 4, summarize the main results of this study.

## 2. Methodology

All ab initio computations are executed employing two complementary codes within density functional theory (DFT). Structural optimization and elastic constants are proceeded through the pseudo-potential plane-wave (PP-PW) process as incorporated in the calculation module Cambridge Serial Total Energy Package (CASTEP) of Materials Studio [30]. The generalized gradient approximation in the scheme of Perdew et al., also recognized as GGA-PBEsol [31] are adopted to estimate the exchange–correlation effects. The GGA-PBEsol functional has been specially developed to enhance the exchange-correlation potential modeling in solids. Vanderbilt-type ultra-soft pseudo-potential [32] is utilized to simulate the potential visible by the electrons of valence due to the frozen-core electrons and the nucleus. The following electron states: Sr -$4s^2$ $4p^6$ $5s^2$, Ca- $3s^2$ $3p^6$ $4s^2$, Ge-$4s^2$ $4p^2$, Si-$3s^3$ $3p^2$ and N-$2s^2$ $2p^3$ are delighted as valence states. A plane-wave cut-off energy of 450 eV and Monkhorst-Pack scheme [33] with $6 \times 12 \times 6$ k-point mesh to specimen the Brillouin zone (BZ) are chosen to guarantee a total energy convergence of $5 \times 10^{-6}$ eV/atom. The elastic constants ($C_{ij}$s) of $Ca_5Si_2N_6$ and $Sr_5Ge_2N_6$ were evaluated by employing the well-known finite strain method [30]. This technique encompasses enforcing a combination of similar deformations with a restricted worth and calculating the resulting stress with regard to optimizing the structure of the crystal, as implemented by Milman and Warren [34]. The polycrystalline elastic aggregate moduli and attached properties were obtained via the single-crystal elastic constants $C_{ij}$ over the Voigt-Reuss-Hill approximations [35–37].

It is well established that the common generalized gradient approximation (we used the PBEsol [31] flavor of GGA) calculation consistently underestimates the energy-gaps of semiconductors and insulators representatively by 30–50% [38–40] compared to the experimental ones. This band-gap problem arises because conventional approaches such as GGA and LDA cannot characterize precisely the agitated electronic states. To address this deficiency and acquire credible energy-gap amounts for semiconductors and insulators in comparison to a metrical ones, some advanced XC functionals have been developed, including hybrid functionals [41], the GW approximation [42], and the Tran-Blaha altered Becke-Johnson (TB-mBJ) potential [43,44]. Compared to the other approaches stated above, the TB-mBJ planner is computationally less expensive and provides energy band gaps that are nearly equal to the experimental ones with an extremely lower counting time [43,44]. For this reason, in addendum to the GGA-PBEsol, the optoelectronic and thermoelectric properties of the examined materials are studied employing the TB-mBJ functional as embedded in the WIEN2k code [45]. The schedule bundle WIEN2k [45] is an accomplishment of the full potential linearized augmented plane wave (FP-LAPW) formalism within the DFT framework. In the FP-LAPW approach, the unit cell is split into non-overlapping muffin-tin spheres (MTS) separated by a space known as the interstitial region (IR). In the MTS, the wave functions are dilated using a linear collection of radial atomic functions time spherical harmonics, whereas in the IR, a plane wave foundation collection is employed. A plane-wave cutoff parameter $R_{MT}{*}K_{max}$ is set to be equal to 7. $R_{MT}$ denoted the slightest radius of the muffin-tin sphere and $K_{max}$ denoted the biggest k-vector in the plane wave extension. The k-integration over the Brillouin zone is computed employing a mesh of 1000 k-points in the irreducible Brillouin zone, according to the Monkhorst–Pack scheme [33].

The optic possession of a material has the ability to be accessed by the complex dielectric function $\varepsilon(\omega) = \varepsilon_1(\omega) + i\varepsilon_2(\omega)$, that is directly related to the linear restraint of issue to incident radiance. The second term $\varepsilon_2(\omega)$ of the complex dielectric function, which distinguishes the sucking of the incident illumination by the object, has the ability to be evaluated by scoring all pliable direct electronic transferences from taken to vacant states [46]. The $\varepsilon_1(\omega)$, that models the scuttle of the incident streaks by the object, has the ability to be derived from the $\varepsilon_2(\omega)$ via the Kramer–Kronig conversion [47]. All the latest frequencies are dependent on optic functions, like the absorption coefficient $\alpha(\omega)$, optic reflectivity $R(\omega)$, extinction coefficient $k(\omega)$, refractive index $n(\omega)$ and energy-loss spectrum $L(\omega)$, can be calculated by the use of the complex dielectric function $\varepsilon(\omega)$. To achieve more accurate calculations, a dense k-point mesh of 12000 is employed for carrying out the optic estates of $Ca_5Si_2N_6$ and $Sr_5Ge_2N_6$.

## 3. Results and discussion

### 3.1. Structural properties

The title compounds adopt a monoclinic crystal structure and belong to space group *C2/c* (N°:15), which has four unit formulation per unit cell (Z = 4) [28,29]. These materials' crystal structure have the ability to be characterized as two edge-sharing $(Si/Ge)_2N_6$ tetrahedron surrounded by (Ca/Sr) atoms. A ball-and-stick representation of $Ca_5Si_2N_6$ and $Sr_5Ge_2N_6$ traditional unit cell is displayed in Fig. 1. Full geometry optimization were obtained via the Broyden–Fletcher– Goldfarb–Shanno (BFGS) algorithm [48] that is known as the speedy path to detect the low-energy structure. Geometrical relaxations are executed with the next convergence standards: (i) overall energy tolerance of $5 \times 10^{-7}$ eV/atom, (ii) extreme ionic Hellmann–Feynman force, of 0.01 eV/Å, (ii) ultimate atomic displacement of $5 \times 10^{-4}$Å and (iii) extreme stress of 0.02. GPa. The obtained structural parameters (*a, b, c,* $\beta^\circ$ and V) of $Ca_5Si_2N_6$ and $Sr_5Ge_2N_6$ have been summarized in Table 1. Also shown for rapprochement are the obtainable experimental datum. For both compounds, we can see that the obtained lattice parameters coincide very well with experiment; the maximum deviation is about 0.8%. However, it should be noted that the equilibrium volumes of $Ca_5Si_2N_6$ and $Sr_5Ge_2N_6$ were underestimated by about 2.3% and 1% respectively. The substitution of Ca and Si with heavier atoms (Sr and Ge) leads to increase the equilibrium volume by about 18% from 729.83 $Å^3$ ($Ca_5Si_2N_6$) to 896.33 $Å^3$ ($Sr_5Ge_2N_6$), the latter being due at larger ionic radii. The trend of increasing cell volume V in the examined crystals is consistent with the corresponding lattice expansion (*a*, *b* and *c*).

Different methods have been used to test crystal stability, including phonon dispersion curves [49–51], cohesive energy and formation enthalpy [52]. As lattice dynamics calculations are time-consuming and

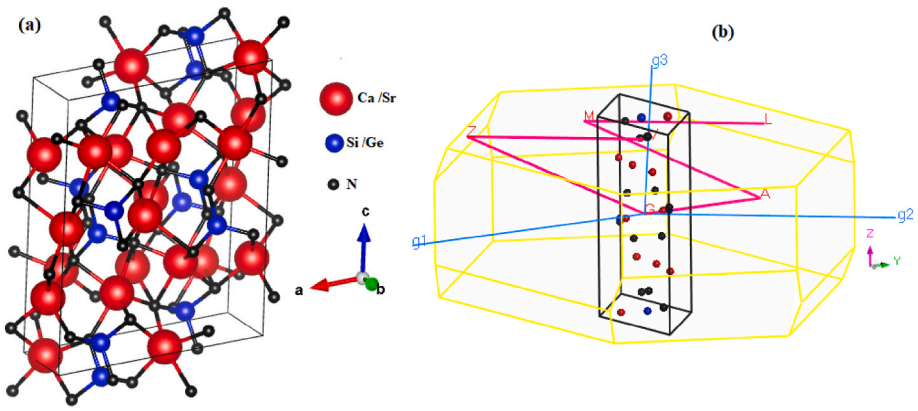


**Fig. 1.** **(a)** Conventional unit cell, **(b)** Primitive unit cell and its Brillouin zone of $Ca_5Si_2N_6$ and $Sr_5Ge_2N_6$.

**Table 1**
Calculated values of lattice constants (*a*, *b* and *c* in Å), angle between *a* and *c* axes ($\beta$ in °), unit-cell volume V (in $Å^3$) compared with existing work, cohesive energy ($E_{coh}$ in eV/atom) and enthalpy of formation ($\Delta H_f$ in eV/atom) for the ternary nitrides $Ca_5Si_2N_6$ and $Sr_5Ge_2N_6$.

| | | *a* | *B* | *c* | $\beta$ | V | $E_{coh}$ | $\Delta H_f$ |
|---|---|---|---|---|---|---|---|---|
| $Ca_5Si_2N_6$ | Present work | 9.759 | 6.004 | 12.657 | 100.27 | 729.83 | −6.96 | −1.54 |
| | Expt. [28] | 9.836 | 6.052 | 12.757 | 100.20 | 747.40 | | |
| $Sr_5Ge_2N_6$ | Present work | 10.342 | 6.530 | 13.486 | 100.27 | 896.33 | −6.19 | −1.03 |
| | Expt. [29] | 10.408 | 6.521 | 13.565 | 100.29 | 905.80 | | |

these compounds have already been synthesized, we restricted our study to the other two criteria. Thus, to explore the chemical and structural stability of the studied materials, the cohesive energy $E_{coh}$ and the enthalpy of formalization $\Delta H_f$ have been estimated according to the equations [52]:

$$E_{coh} = \frac{1}{N_{Ca} + N_{Si} + N_N}\left[E_{Tot}(Ca_5Si_2N_6) - \left(N_{Ca}E^{Ca}_{atom} + N_{Si}E^{Si}_{atom} + N_NE^N_{atom}\right)\right] \quad (1)$$

$$\Delta H_f = \frac{1}{N_{Ca} + N_{Si} + N_N}\left[E_{Tot}(Ca_5Si_2N_6) - (N_{Ca}E_{Ca} + N_{Si}E_{si} + N_NE_N)\right] \quad (2)$$

Here, $N_{Ca}$, $N_{Si}$ and $N_N$ are the numeral of Ca, Si and N atoms in the primitive cell of $Ca_5Si_2N_6$ and $E_{Tot}(Ca_5Si_2N_6)$ its total energy; $E^{Ca}_{atom}$, $E^{Si}_{atom}$ and $E^N_{atom}$ denote the overall energies of segregate Ca, Si and N atoms, respectively; $E_{Ca}$, $E_{si}$ and $E_N$ represent the overall energies per atom of the pure element Ca, Si and N in bulk form. The two energy definitions for the other material ($Sr_5Ge_2N_6$) are identical and have been eliminated here. As shown in Table 1, the obtained coherent energy and fashioning enthalpy values are negative, indicating the thermodynamic stability of the examined crystals at normal status of pressure and temperature. Further, $Ca_5Si_2N_6$ is further stabilized than $Sr_5Ge_2N_6$ at nil pressure and temperature due to bring down negative consistent energy and fashioning enthalpy.

### 3.2. Elastic constants and related properties

The reciprocal relation between elastic ownerships and many other fundamental physical properties, from microscopic level (electronic properties, bond stiffness, etc.) to macroscopic level (dislocation, compressibility, etc.) gives the investigation of elastic properties a critical importance in numerous domains of materials research [53–56]. Recently, DFT approaches permit us to prophesy reliable results for the elastic properties of a considerable scale of materials [57–59]. Elastic properties of monoclinic systems can be described using thirteen independent elastic constants $C_{ij}$ [60]. Table 2 displays the full calculated collection of elastic constants concerning the suggested compounds. The evaluated elastic constants $C_{ij}$ for $Ca_5Si_2N_6$ and $Sr_5Ge_2N_6$ are content with the mechanical settlement standard of monoclinic structure [60], which means that the title materials are stable mechanically. According to Table 2, one may observe that the unidirectional elastic constants $C_{11}$ along *a*-axis, $C_{22}$ along *b*-axis and $C_{33}$ along *c*-axis have the highest values compared to the other $C_{ij}$. Moreover, it appears that $C_{33}$ has the highest value among all estimated Cij for both compounds, indicating that both crystals should be more resistant to compression strain along c-axis. On the other hand, $C_{44}$, $C_{55}$ and $C_{66}$ (that reflects the stiffness to shear deformation) are lower than the stiffness to uniaxial strains (i.e.: $C_{11}$, $C_{22}$ and $C_{33}$) by about 60%, suggesting that $Ca_5Si_2N_6$ and $Sr_5Ge_2N_6$ are rigid to compression descent than to shear descent. Additionally, it is important to mentioned here that $Ca_5Si_2N_6$ has a higher stiffness compared to $Sr_5Ge_2N_6$.

Large single crystals are often difficult to get at the moment, making

**Table 2**
Calculated elastic constants $C_{ij}$, bulk (B), shear (G) and Young's (E) moduli in GPa, Poisson's ratio (υ), sound velocity ($V_m$) in m/s and Debye temperature ($T_D$) in K for the monoclinic $Ca_5Si_2N_6$ and $Sr_5Ge_2N_6$.

| | $C_{11}$ | $C_{22}$ | $C_{33}$ | $C_{44}$ | $C_{55}$ | $C_{66}$ | $C_{12}$ | $C_{13}$ | $C_{15}$ | $C_{23}$ |
|---|---|---|---|---|---|---|---|---|---|---|
| $Ca_5Si_2N_6$ | 181 | 128 | 213 | 58 | 55 | 53 | 84 | 36 | −14 | 80 |
| $Sr_5Ge_2N_6$ | 147 | 95 | 158 | 41 | 40 | 35 | 61 | 38 | −4.84 | 69 |
| | **$C_{25}$** | **$C_{35}$** | **$C_{46}$** | **B** | **G** | **E** | **B/G** | **υ** | **$V_m$** | **$T_D$** |
| $Ca_5Si_2N_6$ | −0.30 | −18 | −10 | 101 | 50 | 129 | 2.01 | 0.29 | 4443 | 548 |
| $Sr_5Ge_2N_6$ | −5.57 | −8.57 | −7.82 | 80 | 36 | 95 | 2.21 | 0.30 | 3003 | 346 |

it impossible to quantify the individual elastic constants. In state of measuring $C_{ij}$, the bulk modulus B and shear modulus G can be evaluated experimentally on the polycrystalline specimens and used to define the mechanical properties of the material. The macroscopically measurable quantities (B and G) may be theoretically computed by a specific averaging of the independent $C_{ij}$ of the mono-crystalline stage. The Voigt–Reuss–Hill homogenization method is used to estimate the B and G moduli [35–37]. Voigt and Reuss approximations are known to give extreme amounts for B and G, while Hill approximation takes the arithmetic average of the two boundaries and recommended it as efficient moduli in usage for polycrystalline specimens [35–37]. Therefore, we have adopted here the Hill's approximation [37] to evaluate the polycrystalline elastic moduli for the titled compounds, which is known as pursued:

$$B = (B_V + B_R)/2\ ;\ G = (G_V + G_R)/2 \tag{3}$$

definitions of the Voigt ($B_V$, $G_V$) and Reuss ($B_R$, $G_R$) restricted for a monoclinic structure has the ability to be established in Ref. [60]. The computed amounts of B and G are used to evaluate the Young's modulus (E) and Poisson's ratio ($\upsilon$) by utilizing the following expressions [37]:

$$E = 9BG(3B+G)^{-1}\ ;\ \upsilon = (1/2)(3B-2G)(3B+G)^{-1} \tag{4}$$

The obtained amounts for the above-reminder parameters for the herein behold materials are summarized in Table 2. It is completely recognized that a material's stiffness can be assessed by looking at its B, that measures the resistance to the volume variation under hydrostatic pressures, G, that represents the resistance to reversible distortion under shear stress, and E, that measures the ratio of linear stress to linear strain in the situation of stretchy forces. According to the amounts of B, G and E reported in Table 2, it is clear that $Ca_5Si_2N_6$ is stiffer $Sr_5Ge_2N_6$. It is seen that $B > G$, suggesting that the G is the factor limiting the stability of the studied crystals. Additionally, B and G give datum regarding the malleability of materials out of Pugh's empirical criterion B/G [61]. Accordingly, if B/G is smaller than 1.75, a brittle behavior is predicted; else, the material proceeds in a ductile attitude. The examined compounds have Pugh's ratios greater than 1.75 (see Table 2), indicating that these materials are ductile and will be resistant to thermal shocks. In this context, the failure mode (ductility/brittleness) can also be predicted via the $\upsilon$ with a critical amount of $\upsilon = 0.26$ [62,63]. If $\upsilon$ is greater (smaller) than 0.26, a material affords ductile (brittle) insufficiency. The $\upsilon$ values of $Ca_5Si_2N_6$ and $Sr_5Ge_2N_6$ are equal to 0.29 and 0.30, implying again their ductile nature. The good approval emphasizes the reliability and precision of the current computations. $\upsilon$ manifests as an effective equipment to appreciate the kind of chemical bonding in crystals [64]. The amount of the $\upsilon$ is equal to 0.33 for completely metallic materials, however for purely ionic compounds, a representative amount of $\upsilon$ is 0.25. Based on these conditions, the stability of the studied materials are maintained by a mixture of metallic ionic-bonds.

Another intriguing physical parameter linked to the elastic ownerships of solid materials is the elastic anisotropy, which considers various bonding qualities in various crystallographic trends. The crystal anisotropy plays an important role in several mechanical properties of solids, like elastic instability, stage transitions, dislocation dynamics, etc. Furthermore, micro-cracks have the ability to be facilely prompted in materials with considerable elastic anisotropy; thus to ameliorate their mechanical strength, it is significant to evaluate their elastic anisotropy [65]. At present, to accurately quantify the elastic anisotropy for the investigated materials, we have adopted the global anisotropy signal $A^U$ proposed by Ranganathan et al. [66] known as:

$$A^U = 5G_V/G_R + B_V/B_R - 6 \tag{5}$$

For perfect isotropic crystals, $A^U$ is amounting to zero ($A^U = 0$); the variations of $A^U$ from zero define the level of anisotropy for the crystal. The estimated amounts of $A^U$ are established to be 1.03 for $Ca_5Si_2N_6$ and 0.785 for $Sr_5Ge_2N_6$, revealing a significant elastic anisotropy for both compounds. To extend a comprehensive description of the mechanical properties, the Debye temperature $T_D$ of the tested materials were appreciated from the isotropic intermediate sound velocity $V_m$ via the next expression [67]:

$$T_D = \frac{h}{k_B}\left[\frac{3n}{4\pi}\frac{\rho N_A}{M}\right]^{1/3} V_m \tag{6}$$

where is $h$ is Plank's constant, $k_B$ is Boltzmann's constant, $n$ is the number of atoms per formula unit, $N_A$ is Avogadro's number, $\rho$ is the crystal structure's density, and $M$ is the molar mass. In a polycrystalline material, $V_m$ might be computed utilizing the longitudinal and transverse sound wave velocities ($V_l$ and $V_t$) as follows [67,68]:

$$V_m = \left[\left(2V_t^{-3} + V_l^{-3}\right)/3\right]^{-1/3}\ ;\ V_l = (3B + 4G/3\rho)^{1/2}\ ;\ V_t = (G/\rho)^{1/2} \tag{7}$$

Here $B$ and $G$ are the DFT calculated bulk and shear moduli. Recently, the material's Debye temperature $T_D$ is considered as the most reliable proxy for phosphor materials, because of its proportionality to the structural rigidity, that in turn is predominating connected to thermal quenching mechanisms and quantum harvest [9,69–71]. As a result, this has even been included into machine learning algorithms to seek for novel promising phosphor materials [72,73]. According to Table 2, $Ca_5Si_2N_6$ has the highest Debye temperature (>500 K), confirming that it is appropriate for employ as a phosphor material [72,74]. In contrast, the nitridogermanate has a lower Debye temperature value (360 K) due to its substitution with heavier cations, resulting in lower the overall phononic contributions.

### 3.3. Electronic properties

Knowing the Debye temperature of a crystal structure alone is insufficient to assess the potential suitability of $Ca_5Si_2N_6$ and $Sr_5Ge_2N_6$ as luminescence materials. A wide band gap (Eg) is also essential when screening for new phosphors [72,74,75]. Therefore, the electronic properties of the herein studied compounds were investigated through their band structure, total and partial density of state (TDOS and PDOS). Various first–principles approaches have been used to examine electronic properties and highlight the atomic contribution to the band structure curves [58,74–77]. Fig. 2 illustrates the computed band-structure of $Ca_5Si_2N_6$ and $Sr_5Ge_2N_6$ over the high symmetry orientations in the first Brillouin zone (BZ) using the GGA-PBEsol and the TB-mBJ methods, respectively. The results show an obvious segregation between the valence and the conduction curves, making these compounds a semiconductor in nature. Our first-principles computation within the GGA-PBEsol yielded an indirect band-gap of 2.29 eV and 1.47 eV for both $Ca_5Si_2N_6$ and $Sr_5Ge_2N_6$ respectively. For Both compounds, the maximum of the valence band happens at the V-point and the minimum of the conduction band happens at the Γ point (see bottom panel of Fig. 2). Given the fact that the GGA approaches are usually underestimate the band-gap amount by about 30%–50%, %, it follows that the actual band gaps of the examined materials should be wider. For the two nitrides, the band profiles obtained from the TB-mBJ exchange potential are nearly identical to those of the GGA-PBEsol ones, with a distinct variation in their band gap values. We see in the upper panel of Fig. 2, that the band-gap energy is shifted from indirect to direct (V→V) for $Ca_5Si_2N_6$ at a value of 3.55 eV. Unlike $Sr_5Ge_2N_6$, the energy gap remains indirect but with an account of 3.15 eV. There is no data on the energy gap amount in the literature to be contrasted with our findings. Another indication that nitridosilicate can be employed as activator produced luminescence (e.g. from $Eu^{2+}$ or $Ce^{3+}$) is that the bandwidth of the compound is within 3.5–3.8 eV [20,74]. This has already been proven by Huang et al. in their study of the $Eu^{2+}$ doped $Ca_5Si_2N_6$ material [27]. Contrary to $Sr_5Ge_2N_6$, where replacing Ca and Si atoms by Sr and Ge atoms leads to narrowing the $Eg$ value. However, this nitridogermanate may still be appropriate for potential optical applications. It

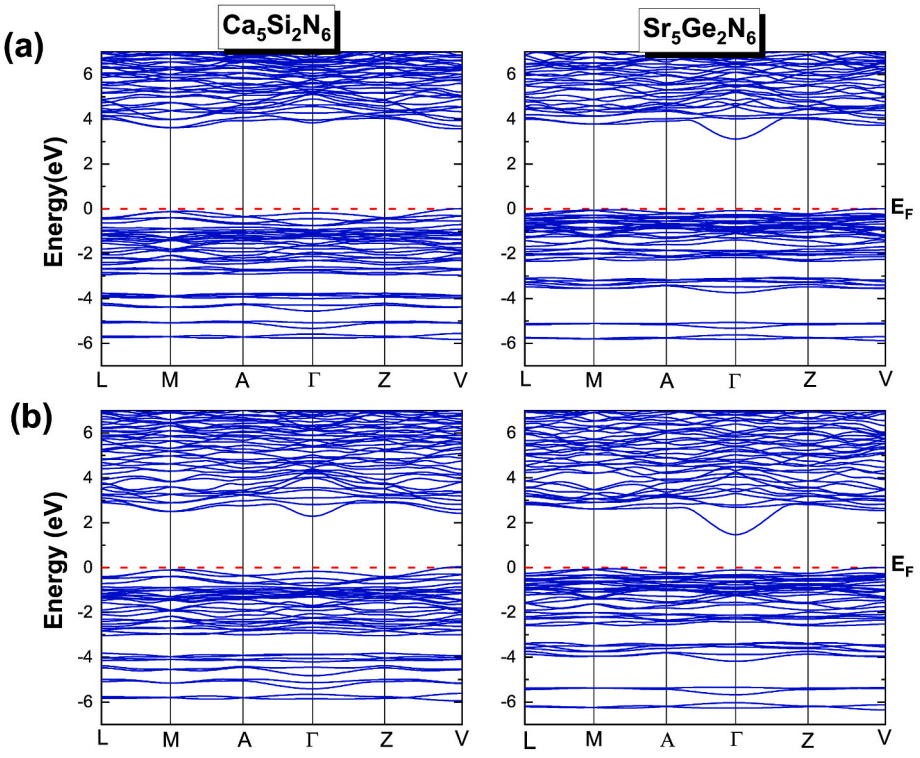


**Fig. 2.** Electronic band structure of $Ca_5Si_2N_6$ and $Sr_5Ge_2N_6$ using **(a)** TB-mBJ, and **(b)** GGA-PBEsol method.

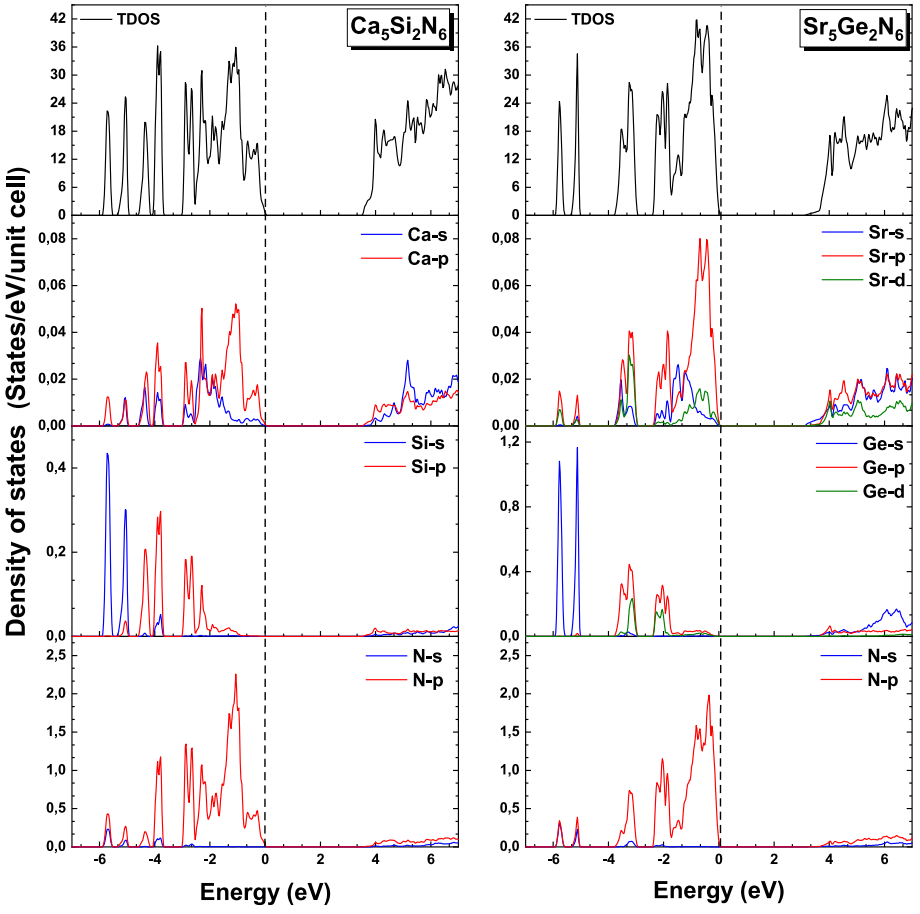


**Fig. 3.** Total (TDOS) and partial (PDOS) density of state for $Ca_5Si_2N_6$ and $Sr_5Ge_2N_6$ using the TB-mBJ functional.

is merit to reminder here that the computed Eg-mBJ values can be improved by partially substituting Li and Mg in $Sr_5Ge_2N_6$ for the discovery of new nitridogermanates that may be used as phosphor materials or wide-gap semiconductors [74].

To shed light on the kind of the electronic structure, the diagrams of total and atomic site projected densities of states (TDOS and PDOS, respectively) are plotted in Fig. 3. For both crystals, there exist three blocks V1, V2 and C1: the first block located around −4 (−3.25) eV for $Ca_5Si_2N_6$ ($Sr_5Ge_2N_6$) is fundamentally collected of N-p and (Si/Ge)-p states with a negligible contribution from (Ca/Sr)-sp states. The second block V2 extending from −3 eV and −2.2 eV up to the Fermi level for $Ca_5Si_2N_6$ and $Sr_5Ge_2N_6$ respectively, originates mainly from the N-2p states with a little involvement from the (Ca/Sr)-*p* and (Si/Ge)-*p* states. The third block C1 above the Fermi level of $Ca_5Si_2N_6$, comes principally from the unoccupied N (*s*, *p*) states with a few contributions (*s*, *p*) states of Si and Ca atoms. The status is not so distinct in the situation of $Sr_5Ge_2N_6$, where the Sr atoms show a small contribution to the C1 block, and the N-2p and Ge-4s states dominate the conduction band followed by the N-2s and Ge-4p states. In other words, most electronic transitions should exist between the controlling N states at the edge of the valence band and the unoccupied Ca, Sr, Ge, and N states in the conduction band.

### 3.4. Optical properties

The optical ownerships of the studied materials supply significant input about their domestic structure. For this, the optical properties of $Ca_5Si_2N_6$ and $Sr_5Ge_2N_6$ have been computed through the TB-mBJ approach and plotted (Fig's 4–5) in a broad energy domain 0–40 eV. As the examined materials belong to a monoclinic regulation, space group *C*2/*c*, it is indispensable to compute dielectric function $(\varepsilon_1, \varepsilon_2)$ and the other macroscopic optical constants for three light polarizations which correspond to the three main crystallographic directions: $a(100)$, $b(010)$ and $c(001)$. Fig. 4 illustrates the curves of the $(\varepsilon_2(\omega))$ and $(\varepsilon_1(\omega))$ of the $Ca_5Si_2N_6$ and $Sr_5Ge_2N_6$ dielectric functions versus the photon energy in the framework 0–18eV, for three incident light polarizations along [100], [010] and [001] directions.

From Fig. 4, one may observe that the intensities and energy positions of the main peaks in $\varepsilon_2(\omega)$ and $\varepsilon_1(\omega)$ are clearly different in the three light polarizations and are smaller for the [100] polarization. This is a clear indication that the complex dielectric functions display a noteworthy anisotropy for different polarizations [100], [010] and [001]. The compound $Ca_5Si_2N_6$ shows a more significant anisotropy than $Sr_5Ge_2N_6$, and even its sucking brink is somewhat proceeded towards low energies for the [100] polarization. Using the DOS diagrams (Fig. 3) and the fact that $\varepsilon_2(\omega)$, is proportionate to the crystal sucking shadow, it is tolerable to attribute the sucking peaks between 3.25 and 8 eV to the electronic commutes from the filled N-2*p* states to the empty Ca/Sr, Ge and N states.

The static dielectric constant is the extreme substantial proportion to be studied in the dispersive $(\varepsilon_1(\omega))$ spectrum, which is known as the zero-energy of $\varepsilon_1(\omega) : \varepsilon_1(\omega \to 0)$. The calculated $\varepsilon_1(0)$ values for $Ca_5Si_2N_6$ ($Sr_5Ge_2N_6$) are found to be 4.31 (4.61) for the [100] polarization and 4.25 (4.53) for the other two polarizations, i.e [010] and [001]. It should be noted that the $\varepsilon_1(0)$ values of $Sr_5Ge_2N_6$ are slightly larger than those of $Ca_5Si_2N_6$. In other words, $\varepsilon_1(0)$ is inversely proportionate with the energy gap, i.e. a least band gap proceeds a bigger $\varepsilon_1(0)$. This agrees well with Penn's model: $\varepsilon(0) \simeq 1 + (\hbar\omega_p / E_g)$ [78], where $E_g$ and $\omega_p$ are the energy gap and plasma frequency, respectively.

The absorption coefficient $\alpha(\omega)$ is a substantial optical parameter, that evaluates the amount of energy for an electromagnetic wave of frequency $(\omega)$, soaked up per unit extent of an average, where it spreads. The absorption spectrum gives useful information that can be used to evaluate certain optoelectronic instruments like sunlight converter. Panel (a) of Fig. 5 displays the computed absorption shadow of the designation materials in an energy zone up to 40 eV for three different polarizations. The absorption coefficient $\alpha(\omega)$ increases quickly while the photon energy is bigger than the absorption border, as seen in Fig. 5 (a). Note that absorption curves for the three various polarizations of the incident radiation start at the same absorption threshold for the $Sr_5Ge_2N_6$ compound, which indicate that the band border is isotropic. This is not the case for the $Ca_5Si_2N_6$ compound, where the absorption edge along the [100] starts earlier than in the other directions ([010] and [001]).

The absorption ranges from 3.6 to 35 eV, with three peaks occurring at around 8.7 eV, 14.3 eV and 28.7 eV for $Ca_5Si_2N_6$, and from 3.2 to 35 eV, with also three peaks occurring at about 4.9 eV, 9.3 eV and 25.3 eV for $Sr_5Ge_2N_6$. The highest $\alpha(\omega)$ values are found in the [010] direction,

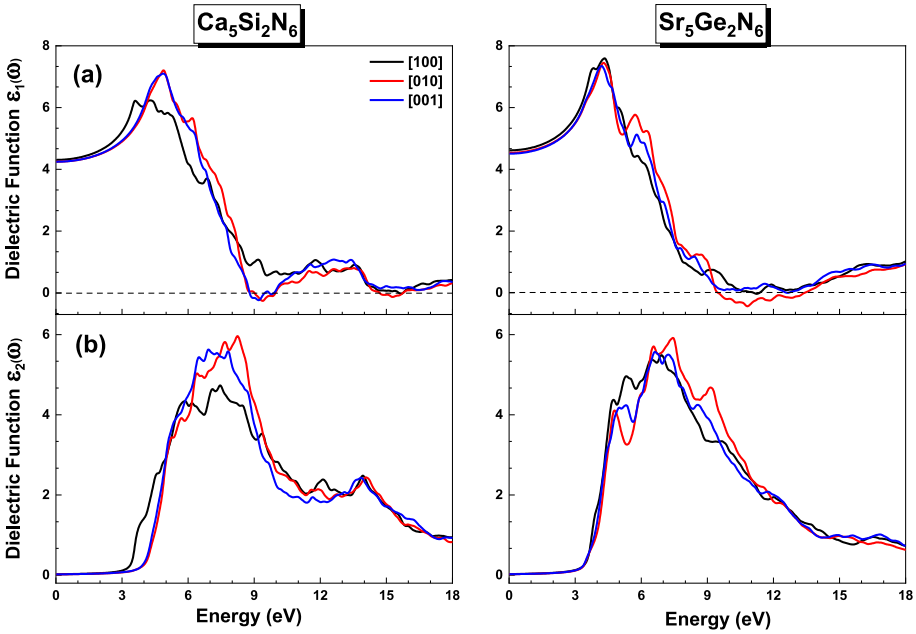


**Fig. 4.** Calculated real $\varepsilon_1(\omega))$ and imaginary $\varepsilon_2(\omega)$ parts of the complex dielectric function for $Ca_5Si_2N_6$ and $Sr_5Ge_2N_6$ compounds for different polarizations of incident radiation.

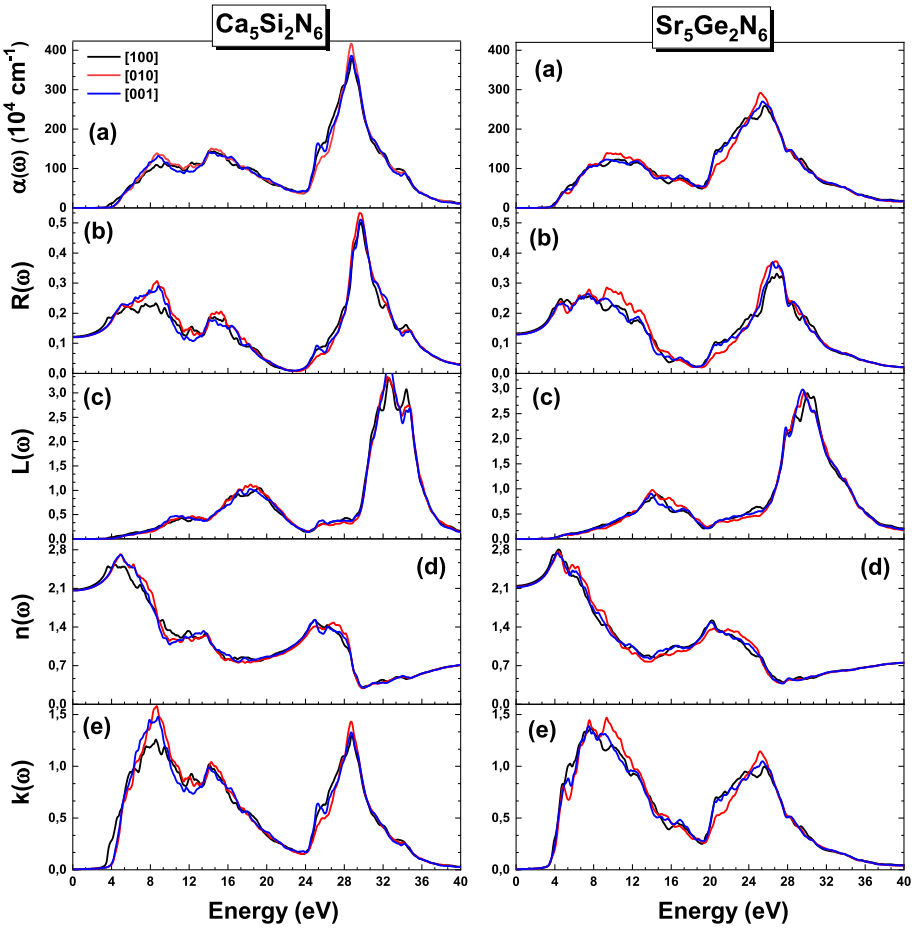


**Fig. 5.** Calculated optical constants: Absorption coefficient $\alpha(\omega)$, reflectivity $R(\omega)$, energy loss function $L(\omega)$, refractive index $n(\omega)$ and extinction coefficient $k(\omega)$ for the $Ca_5Si_2N_6$ and $Sr_5Ge_2N_6$ nitrides for three different polarizations [100], [010] and [001].

reaching $2.91 \times 10^5 cm^{-1}$( 25.2eV) for $Sr_5Ge_2N_6$ and $4.16\times\ 10^5 cm^{-1}$ (28.7eV) for $Ca_5Si_2N_6$, demonstrating a significant anisotropy between [100], [010], and [001] for the two nitrides. The powerful absorptive of electromagnetic waves in the ultraviolet range proposes that these materials are suitable for UV-optoelectronic purposes.

The fraction (amount) of light reflected at an interface is known as the optical reflectivity ($\boldsymbol{\omega}$). Photon energy reliance of the reflectivity $R(\omega)$ of $Ca_5Si_2N_6$ and $Sr_5Ge_2N_6$ single-crystals for three different light polarizations are displayed in Fig. 5(b). One observes that there is clear anisotropy in the reflectivity shadows $R(\omega)$. The static reflectivity $R(0) = R(\omega \rightarrow 0)$ were about 15% and 13% for $Ca_5Si_2N_6$ and $Sr_5Ge_2N_6$, respectively. Then, the reflectivity increases with augmenting photon energy to extent a maximum of $\sim$ 53% at $\sim$ 29.5*eV* for $Ca_5Si_2N_6$ in the [010] direction, and $\sim$ 37% at $\sim$ 26.8eV for $Sr_5Ge_2N_6$ in the same direction. After that, the reflectivity decreases rapidly to its minimum level.

The energy-loss function $L(\omega)$ characterizes the energy lost by a quick electron as it passes over a homogeneous material. Fig. 5 (c) depicted the reliance of the energy loss shadow on the energy of incident electromagnetic radiation gathered parallel to the [100], [010] and [001] crystalline trends. Bulk plasma frequency $(\omega_p)$, which occurs when $\varepsilon_2(\omega) < 1$ and $\varepsilon_1(\omega)$ arrives to the zero point, is generally considered to be the primary peak of the $L(\omega)$ spectrum [79]. The energy loss function is clearly more pronounced along the [010] and [001] directions and is the weakest along the [100] direction. For radiation polarized in the [001] direction, the plasma frequency for $Ca_5Si_2N_6$ ($Sr_5Ge_2N_6$) is approximately similar to 32.52 eV (29.56 eV), which is associated with the sudden lowering in the reflectivity degree.

Fig. 5 (d) and (e) present the computed refractive index $n(\omega)$ and extinction coefficient $k(\omega)$ shadows for the materials investigated in the energy domain from 0 to 40 eV for three polarizations of the happening electromagnetic radiation. The refractive index $n(\omega)$ explains how an electromagnetic wave propagates differently in a material compared to the vacuum. Knowing this optical constant is very useful in optical apparatuses, like photonic crystals and waveguides. We note from Fig. 5, panel (d) that the $n(\omega)$ curves are started from the static refractive index $n(0) = n(\omega \rightarrow 0)$, which are 2.07, 2.06 and 2.06 for $Ca_5Si_2N_6$, and 2.14, 2.12 and 2.12 for $Sr_5Ge_2N_6$ along the [100], [010], and [001] directions, respectively. Then, $n(\omega)$ increased with the increase of photon energy to extent an extreme amount in the near-UV spectrum, that is similar to $\sim$ 2.72 at $\sim$ 4.93 eV for $Ca_5Si_2N_6$ and $\sim$ 2.80 at $\sim$ 4.39 eV for $Sr_5Ge_2N_6$ for the [010] and [100] directions, respectively. We observe here that the more the refractive index increased in this energy range, the more the light beam was refracted. Afterwards, $n(\omega)$ decreased until it reach its minimum value. The refractive index $n(\omega)$ spectrum has similar structures as the dispersive spectrum $\varepsilon_1(\omega)$. The reduction of electromagnetic waves in a material is directly described by the extinction coefficient $k(\omega)$, that is likewise referred to as a damping stable dilution stage. One notes that the zeroes of $\varepsilon_1(\omega)$ correspond to the local maximum of the extinction coefficient $k(\omega)$. By comparison, the spectra of $k(\omega)$ and the absorption $\alpha(\omega)$ are very similar.

### 3.5. *Thermoelectric properties*

Thermoelectric (TE) energy transformation, that includes squandering warmth reclamation, is commonly recognized as a fertile strength generation technique. As a result, discovering and developing more efficient thermoelectric materials is an energetic region of research. The

efficiency of a thermoelectric material in any power generator or cooler is assessed in terms of figure of merit ZT. The ZT value might be calculated by the formula: $ZT = S^2\sigma T/\kappa$, where S attitudes for the Seebeck coefficient, σ for electrical conductivity, T for absolute temperature and κ for total thermal conductivity, which involves both electronic (*e*) and lattice (*l*) contributions i.e., $\kappa = \kappa_e + \kappa_l$ [80–82]. In fact, a good TE material must possess a rising electrical conductivity, a big Seebeck coefficient (S) and a very weak thermal conductivity at a given temperature [82]. The transport properties of the deliberated nitrides $Ca_5Si_2N_6$ and $Sr_5Ge_2N_6$ are explored using the BoltzTrap code over with the constant repose time approach [83]. All thermoelectric parameters are estimated in this work at temperatures which extent from 200 to 900 K.

Furthermore, the band structure, carrier type, and effective mass are all factors that influence the magnitude of the thermoelectric characteristics. The carriers (holes and electrons) involved in the transport phenomenon are mainly found by their energy gap. It is observed that the application of the mBJ approach widens the band gap compared to GGA. Therefore, band gap tuning is crucial in determining the S. Metals exhibit the lowest S, whereas insulators exhibit the highest S [81].

The S measures the thermoelectric voltage manufactured by the temperature gradient between two finishing of a material [84]. The S variation against temperature is plotted in Fig. 6(a). One can observe that S decreases with increasing temperature for both crystals. When the temperature is increased from 200 to 900 K, the value of S decreases from 1686/859 μV/K (200K) to 514/268 μV/K (900 K) for $Ca_5Si_2N_6$ and $Sr_5Ge_2N_6$, respectively. For practical applications TE materials should have a S higher than 200 μV/K, which suggests the good TE behavior of the examined nitrides. Both compounds show a positive value of the S above the temperature framework, pointing out that the mobility of carriers is due to holes [85]. Moreover, the substitution of the Ca atom by the Sr atom present an impact on the S, for example at room temperature, for $Ca_5Si_2N_6$ it was computed to be 1203 μV/K, while for $Sr_5Ge_2N_6$ it was evaluated to be 607 μV/K respectively.

The electrical conductivity $\sigma/\tau$ (τ is the relaxation time) is an important thermoelectric factor, caused by the flow of release transporters (electrons or holes), and with increasing temperature it increases because of enhanced kinetic energy as shown in Fig. 6(b). The value of $\sigma/\tau$ for both crystals is $9.85 \times 10^{10}$ $(\Omega ms)^{-1}$ at 200 K and becomes $1.37 \times 10^{18}$ $(\Omega ms)^{-1}$ $(0,52 \times 10^{18}$ $(\Omega ms)^{-1})$ for $Sr_5Ge_2N_6$ ($Ca_5Si_2N_6$) at 900 K. It is clear that $Sr_5Ge_2N_6$ has an elevated electrical conductivity than $Ca_5Si_2N_6$, revealing that electrons in $Sr_5Ge_2N_6$ have calorically additional agitated to the conduction bands than in $Ca_5Si_2N_6$. This can be attributed to the increase of ionic size from Ca to Sr, causing the bonds of the valence electrons to loosen and facilitating bond breaking with very little amount of energy. Because the band gap decreases from Ca to Sr, less excitation energy is required, and as a result, more free charge carriers are produced, which leads to an increase in electrical conductivity. Likewise, by replacing Calcium atom with Strontium atom, S diminishes since the potentials preserved across the specimen borders can break down as the energy gap narrows, and liberate charge transporters increase at bring down spectacular energies [86,87].

As mentioned above, total thermal conductivity $(\kappa/\tau)$ emerges because of the assistance of electrons and phonons. In this case, only the electronic contribution $(\kappa_e/\tau)$ was evaluated because of limitation of classical theory-based BoltzTraP code [81]. Its trends versus T are elaborated in Fig. 6 (c) which increases from 200 K and reaches to $1.29 \times 10^{14}$ W/m.K.s and $1.06 \times 10^{14}$ W/m.K.s at 900K for $Ca_5Si_2N_6$ and $Sr_5Ge_2N_6$, respectively. The Widemann-Franz law ($\kappa_e = L\sigma T$) establishes a connect between electrical and thermal conductivities [87]. The ratio $\sigma/\kappa_e$ was noted to be in the order of $10^{-5}$, considering very good electrical conductivity and reduced thermal conductivity [87].

Power factor is a crucial parameter for assessing a material's efficiency for practical thermoelectric device applications. It is calculated as the output of electrical conductivity and the quadrate of the S ($PF = S^2\sigma/\tau$) [81,82]. In Fig. 6(d), the estimated PF per relaxation time for both $Ca_5Si_2N_6$ and $Sr_5Ge_2N_6$ are plotted versus temperature. The computed PF of the two nitrides under investigation improves with temperature, and at 900 is determined to be $1.37 \times 10^{11}$ W/m.K$^2$.s for $Ca_5Si_2N_6$ and $0.99 \times 10^{11}$ W/m.K$^2$.s for $Sr_5Ge_2N_6$. These materials are useful for thermoelectric apparatuses employments because they have such an elevated power agent at elevated temperatures. Figure of merit (ZT) is one more parameter that locates energy conversion efficiency in the thermoelectric material [82]. The calculated ZT values of these compounds are shown in Fig. 7(a) versus T and in Fig. 7(b) versus chemical potential $\mu$, respectively. At low temperature (200 K), the obtained ZT values for both compounds are almost identical. In contrast,

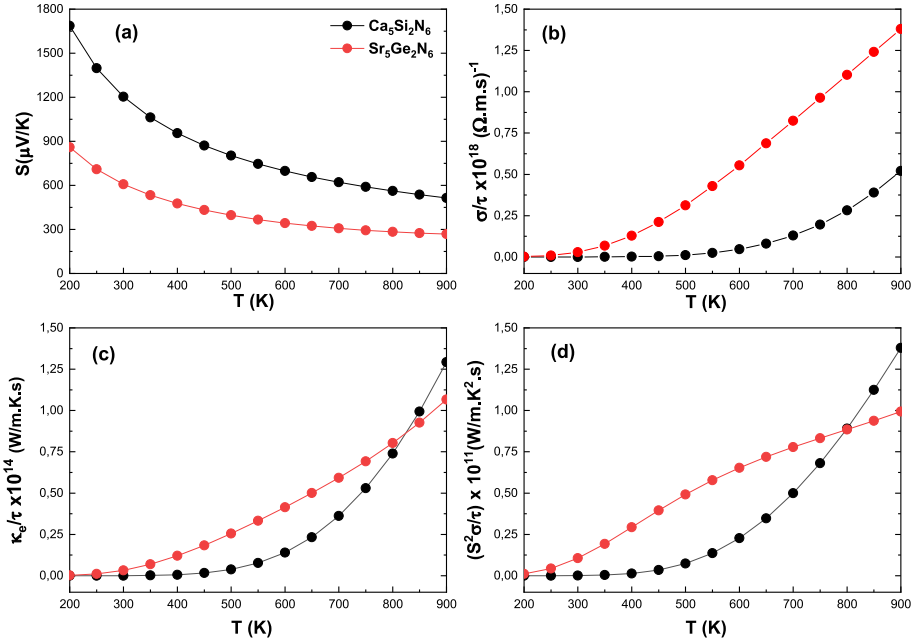


**Fig. 6.** Calculated values of **(a)** Seebeck coefficient (S), (**b**) electrical conductivity $(\sigma/\tau)$, (**c**) thermal conductivity $(\kappa_e/\tau)$ and (**d**) power factor $(S^2\sigma/\tau)$ versus temperature for $Ca_5Si_2N_6$ and $Sr_5Ge_2N_6$.

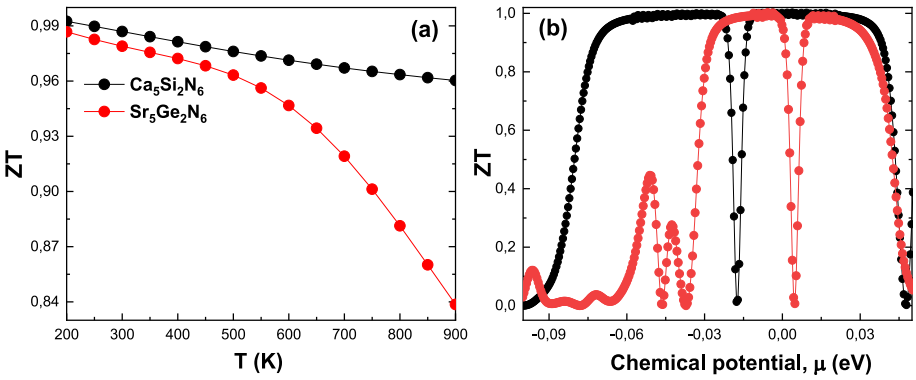


**Fig. 7.** The calculated figure of merit ZT versus **(a)** T and **(b)** μ for $Ca_5Si_2N_6$ and $Sr_5Ge_2N_6$.

at high temperature (900 K), ZT factor of $Ca_5Si_2N_6$ maintain its value, while $Sr_5Ge_2N_6$ decreases to a value of 0.84. At 300 K, the figure of merit (ZT) for $Ca_5Si_2N_6$ and $Sr_5Ge_2N_6$ is computed to be 0.986 and 0.978, respectively. Additionally, its behavior versus $\mu$ at room temperature has been plotted in Fig. 7(b). In the given region of μ, ZT fluctuates and approaches the unity in both regions n and p for the two studied compounds, however these materials behave better in the p-type region as shown in Fig. 7(b). One can speculate according to these findings that the materials under investigation could have outstanding thermoelectric performance at low and room temperature.

## 4. Conclusions

In conclusion, the elastic, electronic, optoelectronic and thermoelectric properties of the ternary nitrides $Ca_5Si_2N_6$ and $Sr_5Ge_2N_6$ are studied using the DFT within the GGA-mBJ approximations. The theoretically predicted lattice parameters constants are consistent with the available experimental results. According to the estimated cohesive energy, formation enthalpy and Born-Huang stability criterion, the thoughtful materials are thermodynamically and mechanically steady. Findings on elastic properties suggest that both nitrides are ductile in nature with significant elastic anisotropy. Through the use of the TB-mBJ electronic band structure, these nitrides were found to be semiconductors with a direct bandgap (V–V) of 3.55 eV for $Ca_5Si_2N_6$ and an indirect band gap (V-Γ) of 3.15 eV for $Sr_5Ge_2N_6$. The nitridosilicate compound can be used as a phosphor material because the bandgap and Deby temperature values are within the recommended range. Substitution with heavier cations leads to narrowing the Eg value and reducing the $T_D$ value. Even that, this material is still useful for other optical applications. The computed optical functions show a modest static dielectric, a notable optical anisotropy and a strong absorptivity of electromagnetic waves in the ultraviolet range, indicating that the title materials are appropriate for UV-optoelectronic employments. Furthermore, transport properties, including Seebeck coefficient, electrical conductivity, thermal conductivity, power factor and figure of merit are studied employing classical BoltzTrap software. The large figure of merit (ZT) values of these ternary nitrides, suggests their potential use in thermoelectric devices, especially at low and room temperature.

## Author statement

All the authors were involved in the preparation of the manuscript. All the authors have read and approved the final version of the manuscript.

## Declaration of competing interest

There is no conflict of interest.

## Data availability

No data was used for the research described in the article.

## References

[1] U. Chatterjee, J. Park, D. Um, C. Lee, III-nitride nanowires for solar light harvesting: a review, Renew. Sustain. Energy Rev. 79 (2017) 1002–1015.
[2] A.L. Greenaway, C.L. Melamed, M.B. Tellekamp, R. Woods-Robinson, E.S. Toberer, J.R. Neilson, A.C. Tamboli, Ternary nitride materials: fundamentals and emerging device applications, Annu. Rev. Mater. Res. 51 (1) (2021) 591–618.
[3] V. Sharma, H.L. Kagdada, P.K. Jha, P. Śpiewak, K.J. Kurzydłowski, Thermal transport properties of boron nitride based materials: a review, Renew. Sustain. Energy Rev. 120 (2020), 109622.
[4] Z. Wen, K. Wang, L. Chen, J. Xie, A new ternary composite lithium silicon nitride as anode material for lithium ion batteries, Electrochem. Commun. 8 (8) (2006) 1349–1352.
[5] M. Zeuner, S. Pagano, W. Schnick, Nitridosilicates and Oxonitridosilicates: from ceramic materials to structural and functional diversity, Angew. Chem. Int. Ed. 50 (34) (2011) 7754–7775.
[6] T.D. Moustakas, R. Paiella, Optoelectronic device physics and technology of nitride semiconductors from the UV to the terahertz, Rep. Prog. Phys. 80 (10) (2017), 106501.
[7] P. Pust, P.J. Schmidt, W. Schnick, A revolution in lighting, Nat. Mater. 14 (5) (2015) 454–458.
[8] M.Z. Baten, S. Alam, B. Sikder, A. Aziz, III-nitride light-emitting devices, Photonics 8 (10) (2021) 430.
[9] X. Qin, X. Liu, W. Huang, M. Bettinelli, X. Liu, Lanthanide-activated phosphors based on 4f-5d optical transitions: theoretical and experimental aspects, Chem. Rev. 117 (5) (2017) 4488–4527.
[10] S. Schmiechen, H. Schneider, P. Wagatha, C. Hecht, P.J. Schmidt, W. Schnick, Toward new phosphors for application in illumination-grade white pc-LEDs: the Nitridomagnesosilicates $Ca[Mg_3SiN_4]:Ce^{3+}$, $Sr[Mg_3SiN_4]:Eu^{3+}$, and Eu[Mg3SiN4], Chem. Mater. 26 (8) (2014) 2712–2719.
[11] M. Zeuner, P.J. Schmidt, W. Schnick, One-pot synthesis of single-source precursors for Nanocrystalline LED phosphors $M_2Si_5N_8$: $Eu^{2+}$(M = Sr, Ba), Chem. Mater. 21 (12) (2009) 2467–2473.
[12] R. Xie, N. Hirosaki, Silicon-based oxynitride and nitride phosphors for white LEDs—a review, Sci. Technol. Adv. Mater. 8 (7–8) (2007) 588–600.
[13] R. Xie, H.T. Bert Hintzen, Optical properties of (Oxy)Nitride materials: a review, J. Am. Ceram. Soc. 96 (3) (2013) 665–687.
[14] P. Pust, V. Weiler, C. Hecht, A. Tücks, A.S. Wochnik, A. Henß, D. Wiechert, C. Scheu, P.J. Schmidt, W. Schnick, Narrow-band red-emitting $Sr[LiAl_3N_4]:Eu^{2+}$ as a next-generation LED-phosphor material, Nat. Mater. 13 (9) (2014) 891–896.
[15] J.W.H. Van Krevel, On New Rare-Earth Doped M-Si-Al-O-N Materials : Luminescence Properties and Oxidation Resistance, Eindhoven University of Technology, 2000.
[16] Y. Li, J. Van Steen, J. Van Krevel, G. Botty, A. Delsing, F. DiSalvo, G. De With, H. Hintzen, Luminescence properties of red-emitting $M_2Si_5N_8:Eu^{2+}$ (M=Ca, Sr, Ba) LED conversion phosphors, J. Alloys Compd. 417 (1–2) (2006) 273–279.
[17] W.B. Park, K.H. Son, S.P. Singh, K. Sohn, Solid-state combinatorial screening of $ARSi_4N_7:Eu^{2+}$ (A = Sr, Ba, Ca; R = Y, la, Lu) phosphors, ACS Comb. Sci. 14 (10) (2012) 537–544.
[18] T. Horikawa, M. Fujitani, H. Hanzawa, K. Machida, Structure and photoluminescence properties of MIIMIIISi4N7:$Eu^{2+}$ (MII= Ca, Sr, Ba/MIII= Sc, Y, La) phosphors prepared by Carbothermal reduction and Nitridation, ECS J. Solid State Sci. Technol. 1 (4) (2012) R113–R118.
[19] Y. Li, A. Delsing, R. Metslaar, G. De With, H. Hintzen, Photoluminescence properties of rare-earth activated BaSi7N10, J. Alloys Compd. 487 (1–2) (2009) 28–33.
[20] C.J. Duan, X.J. Wang, W.M. Otten, A.C. Delsing, J.T. Zhao, H.T. Hintzen, Preparation, electronic structure, and photoluminescence properties of $Eu^{2+}$and

$Ce^{3+}$/$Li^{+}$-activated alkaline earth silicon nitride MSiN2 (M = Sr, Ba), Chem. Mater. 20 (4) (2008) 1597–1605.
[21] Y.Q. Li, N. Hirosaki, R. Xie, T. Takada, Y. Yamamoto, M. Mitomo, K. Shioi, Synthesis, crystal and local electronic structures, and photoluminescence properties of red-emitting CaAlzSiN$^{2+}$z:$Eu^{2+}$ with orthorhombic structure, Int. J. Appl. Ceram. Technol. 7 (6) (2009) 787–802.
[22] Q. Liu, T. Wang, Tuning luminescence by varying the O/N or Al/Si ratio in some Eu-doped nitride phosphors, Phosphors Up Convers. Nano Part. Quant. Dots Appl. (2016) 343–370.
[23] K. Uheda, N. Hirosaki, Y. Yamamoto, A. Naito, T. Nakajima, H. Yamamoto, Luminescence properties of a red phosphor, $CaAlSiN_3$:$Eu^{+2}$, for white light-emitting diodes, Electrochem. Solid State Lett. 9 (4) (2006) H22–H25.
[24] M. Mikami, S. Shimooka, K. Uheda, H. Imura, N. Kijima, New green phosphor Ba3Si6O12N2:Eu for white LED: crystal structure and optical properties, Key Eng. Mater. 403 (2008) 11–14.
[25] A.C. Delsing, G. De With, H.T. Hintzen, Luminescence properties of Eu2+-activated alkaline-earth silicon-oxynitride $MSi_2O_{2-\delta}N_{2+2/3\delta}$ (M = Ca, Sr, Ba): a promising class of novel LED conversion phosphors, Chem. Mater. 17 (12) (2005) 3242–3248.
[26] P. Pust, F. Hintze, C. Hecht, V. Weiler, A. Locher, D. Zitnanska, S. Harm, D. Wiechert, P.J. Schmidt, W. Schnick, Group (III) nitrides $M[Mg_2Al_2N_4]$ (M = Ca, Sr, Ba, Eu) and $Ba[Mg_2Ga_2N_4]$—structural relation and Nontypical luminescence properties of $Eu^{2+}$ doped samples, Chem. Mater. 26 (21) (2014) 6113–6119.
[27] J. Huang, T. Jiang, N. Yao, H. Li, X. Xu, Synthesis and characterization of novel nitride phosphors $Ca_5Si_2N_6$: Eu2+/Ce3+, Asian J. Chem. 27 (3) (2015) 938–940.
[28] F. Ottinger, R. Nesper, Synthesis and crystal structure of the Nitridosilicates Ca5 $[Si_2N_6]$ and $Ca_7[NbSi_2N_9]$, Z. Anorg. Allg. Chem. 631 (9) (2005) 1597–1602.
[29] S.C. Junggeburth, O. Oeckler, W. Schnick, Sr5Ge2N6 – a Nitridogermanate with edge-sharing double tetrahedra, Z. Anorg. Allg. Chem. 634 (8) (2008) 1309–1311.
[30] S.J. Clark, M.D. Segall, C.J. Pickard, P.J. Hasnip, M.I. Probert, K. Refson, M. C. Payne, First principles methods using CASTEP, Z. für Kristallogr. - Cryst. Mater. 220 (5–6) (2005) 567–570.
[31] J.P. Perdew, A. Ruzsinszky, G.I. Csonka, O.A. Vydrov, G.E. Scuseria, L. A. Constantin, X. Zhou, K. Burke, Erratum: restoring the density-gradient expansion for exchange in solids and surfaces, Phys. Rev. Lett. 102 (3) (2009) [Phys. Rev. Lett.100, 136406 (2008)].
[32] D. Vanderbilt, Soft self-consistent pseudopotentials in a generalized eigenvalue formalism, Phys. Rev. B 41 (11) (1990) 7892–7895.
[33] J.D. Pack, H.J. Monkhorst, "Special points for brillouin-zone integrations"—a reply, Phys. Rev. B 16 (4) (1977) 1748–1749.
[34] V. Milman, M.C. Warren, Elasticity of hexagonal BeO, J. Phys. Condens. Matter 13 (2) (2000) 241–251.
[35] W. Voigt, Lehrbuch de Kristallphysik, Terubner, Leipzig, 1928.
[36] A. Reuss, Berechnung Der Fließgrenze von Mischkristallen auf Grund Der Plastizitätsbedingung Fur Einkristalle, ZAMM - Z. Angew. Math. Mech. 9 (1) (1929) 49–58.
[37] R. Hill, The elastic behavior of a crystalline aggregate, Proc. Phys. Soc. 65 (5) (1952) 349–354.
[38] J.P. Perdew, M. Levy, Physical content of the exact Kohn-Sham orbital energies: band gaps and derivative discontinuities, Phys. Rev. Lett. 51 (20) (1983) 1884–1887.
[39] L.J. Sham, M. Schlüter, Density-functional theory of the energy gap, Phys. Rev. Lett. 51 (20) (1983) 1888–1891.
[40] P. Mori-Sánchez, A.J. Cohen, W. Yang, Localization and Delocalization errors in density functional theory and implications for band-gap prediction, Phys. Rev. Lett. 100 (14) (2008).
[41] D. Koller, P. Blaha, F. Tran, Hybrid functionals for solids with an optimized Hartree–Fock mixing parameter, J. Phys. Condens. Matter 25 (43) (2013), 435503.
[42] M. Shishkin, G. Kresse, Self-consistent GW calculations for semiconductors and insulators, Phys. Rev. B 75 (23) (2007), 235102.
[43] D. Koller, F. Tran, P. Blaha, Merits and limits of the modified Becke-Johnson exchange potential, Phys. Rev. B 83 (19) (2011), 195134.
[44] D. Koller, F. Tran, P. Blaha, Improving the modified Becke-Johnson exchange potential, Phys. Rev. B 85 (15) (2012), 155109.
[45] P. Blaha, K. Schwarz, G.K.H. Madsen, D. Kvasnicka, J. Luitz, WIEN2k: an Augmented Plane Wave Plus Local Orbitals Program for Calculating Crystal Properties, University Karlheinz Schwarz, 2013.
[46] M. Dadsetani, A. Pourghazi, Optical properties of strontium monochalcogenides from first principles, Phys. Rev. B 73 (19) (2006), 195102.
[47] H.R. Philipp, H. Ehrenreich, Optical properties of semiconductors, Phys. Rev. 129 (4) (1963) 1550–1560.
[48] T.H. Fischer, J. Almlof, General methods for geometry and wave function optimization, J. Phys. Chem. 96 (24) (1992) 9768–9774.
[49] C. Xie, Y. Liu, Z. Zhang, F. Zhou, T. Yang, M. Kuang, X. Wang, G. Zhang, Sixfold degenerate nodal-point phonons: symmetry analysis and materials realization, Phys. Rev. B 104 (4) (2021), 045148.
[50] Y. Yang, J. Wang, Y. Liu, Y. Cui, G. Ding, X. Wang, Topological phonons in Cs-Te binary systems, Phys. Rev. B 107 (2) (2023), 024304.
[51] Y. Yang, C. Xie, Y. Cui, X. Wang, W. Wu, Maximally charged single-pair multi-weyl point phonons in P23-type BeH2, Phys. Rev. B 107 (5) (2023), 054310.
[52] N. Guechi, A. Bouhemadou, R. Khenata, S. Bin-Omran, M. Chegaar, Y. Al-Douri, A. Bourzami, Structural, elastic, electronic and optical properties of the newly synthesized monoclinic Zintl phase BaIn2P2, Solid State Sci. 29 (2014) 12–23.
[53] K. Tanaka, M. Koiwa, Single-crystal elastic constants of intermetallic compounds, Intermetallics 4 (1996) S29–S39.
[54] R. Golesorkhtabar, P. Pavone, J. Spitaler, P. Puschnig, C. Draxl, Elastic: a tool for calculating second-order elastic constants from first principles, Comput. Phys. Commun. 184 (8) (2013) 1861–1873.
[55] G. Lu, L. Zhang, Connecting microscopic structure and macroscopic mechanical properties of structural materials from first-principles, Sci. China Phys. Mech. Astron. 55 (12) (2012) 2305–2315.
[56] N. Bouarissa, Compositional dependence of the elastic constants and the Poisson ratio of GaxIn1-xSb, Mater. Sci. Eng. B 100 (3) (2003) 280–285.
[57] S. Boucenna, K. Haddadi, A. Bouhemadou, L. Louail, F. Soyalp, R. Khenata, Elastic, electronic, chemical bonding and thermodynamic properties of the ternary nitride Ca4TiN4: ab initio predictions, J. Mol. Graph. Model. 92 (2019) 74–85.
[58] S. Boucenna, A. Mosbah, K. Haddadi, L. Louail, A. Bouhemadou, G. Uğur, Theoretical investigation of some fundamental physical properties of the ternary nitrides Ca4SiN4 and Ca4GeN4 under pressure and temperature effect, Comput. Condens. Matter. 32 (2022), e00711.
[59] Y. Wu, Y. Duan, X. Wang, M. Peng, L. Shen, H. Qi, Elastic anisotropy and thermal properties of Zr-Al-N ternary nitrides using first-principles explorations, Mater. Today Commun. 33 (2022), 104651.
[60] Z. Wu, E. Zhao, H. Xiang, X. Hao, X. Liu, J. Meng, Crystal structures and elastic properties of superhard IrN2 and IrN3 from first principles, Phys. Rev. B 76 (5) (2007), 054115.
[61] S. Pugh, XCII. Relations between the elastic moduli and the plastic properties of polycrystalline pure metals, London, Edinburgh Dublin Phil. Mag. J. Sci. 45 (367) (1954) 823–843.
[62] I.N. Frantsevich, F.F. Voronov, S.A. Bokuta, in: I.N. Frantsevich (Ed.), Elastic Constants and Elastic Moduli of Metals and Insulators Handbook, 1983, pp. 60–180. Kiev: Naukovadumka.
[63] G. Vaitheeswaran, V. Kanchana, A. Svane, A. Delin, Elastic properties of $MgCNi_3$-a superconducting perovskite, J. Phys. Condens. Matter 19 (32) (2007), 326214.
[64] A. Savin, H. Flad, J. Flad, H. Preuss, H.G. Von Schnering, On the bonding in Carbosilanes, Angew Chem. Int. Ed. Engl. 31 (2) (1992) 185–187.
[65] P. Ravindran, L. Fast, P.A. Korzhavyi, B. Johansson, J. Wills, O. Eriksson, Density functional theory for calculation of elastic properties of orthorhombic crystals: application to TiSi2, J. Appl. Phys. 84 (9) (1998) 4891–4904.
[66] S.I. Ranganathan, M. Ostoja-Starzewski, Universal elastic anisotropy index, Phys. Rev. Lett. 101 (5) (2008), 055504.
[67] O.L. Anderson, A simplified method for calculating the Debye temperature from elastic constants, J. Phys. Chem. Solid. 24 (7) (1963) 909–917.
[68] E. Schreiber, O.L. Anderson, N. Soga, Elastic Constants and Their Measurements, McGraw-Hill, New York, 1973.
[69] Z. Wang, I. Chu, F. Zhou, S.P. Ong, Electronic structure descriptor for the discovery of narrow-band red-emitting phosphors, Chem. Mater. 28 (11) (2016) 4024–4031.
[70] J. Brgoch, S.P. DenBaars, R. Seshadri, Proxies from Ab initio calculations for screening efficient Ce+3 phosphor hosts, J. Phys. Chem. C 117 (35) (2013) 17955–17959.
[71] K.A. Denault, J. Brgoch, S.D. Kloß, M.W. Gaultois, J. Siewenie, K. Page, R. Seshadri, Average and local structure, Debye temperature, and structural rigidity in some oxide compounds related to phosphor hosts, ACS Appl. Mater. Interfaces 7 (13) (2015) 7264–7272.
[72] Y. Zhuo, A. Mansouri Tehrani, A.O. Oliynyk, A.C. Duke, J. Brgoch, Identifying an efficient, thermally robust inorganic phosphor host via machine learning, Nat. Commun. 9 (1) (2018) 4377.
[73] L. Jiang, X. Jiang, G. Lv, Y. Su, A mini review of machine learning in inorganic phosphors, J. Mater. Inf. 2 (3) (2022) 14.
[74] R. Niklaus, J. Minár, P. Strobel, P.J. Schmidt, W. Schnick, Ab initio exploration and prediction of AE-containing nitrido(litho/magneso)tetrelates (AE = Ca, Sr; Tt= Si, Ge) with $[Si_2N_6]^{10-}$ or $[Ge_2N_6]^{10-}$ units, Dalton Trans. 48 (24) (2019) 8671–8677.
[75] K. Kassali, N. Bouarissa, Effect of nitrogen concentration on electronic energy bands of Ga1-xInxNyAs1-y alloys, Microelectron. Eng. 54 (3–4) (2000) 277–286.
[76] J. Wang, H. Yuan, Y. Liu, X. Wang, G. Zhang, Multiple dimensions of spin-gapless semiconducting states in tetragonal Sr2CuF6, Phys. Rev. B 106 (6) (2022), L060407.
[77] G. Ding, J. Wang, Z. Yu, Z. Zhang, W. Wang, X. Wang, Single pair of type-III Weyl points half-metals: BaNiIO6 as an example, Phys. Rev. Mater. 7 (1) (2023), 014202.
[78] D.R. Penn, Wave-number-Dependent dielectric function of semiconductors, Phys. Rev. 128 (5) (1962) 2093–2097.
[79] C. Li, Z. Wang, C. Wang, First-principles study of the structural, elastic, electronic and optical properties of the monoclinic BiScO3, Phys. B Condens. Matter 406 (10) (2011) 2028–2032.
[80] J. Kangsabanik, A. Alam, High-performance ternary alkali nitrides for renewable energy applications, Phys. Rev. Mater. 3 (10) (2019), 105405.
[81] P. Gorai, V. Stevanović, E.S. Toberer, Computationally guided discovery of thermoelectric materials, Nat. Rev. Mater. 2 (9) (2017).
[82] N. Lu, I. Ferguson, III-nitrides for energy production: photovoltaic and thermoelectric applications, Semicond. Sci. Technol. 28 (7) (2013), 074023.
[83] G.K. Madsen, D.J. Singh, BoltzTraP. A code for calculating band-structure dependent quantities, Comput. Phys. Commun. 175 (1) (2006) 67–71.
[84] X. Zhang, L. Zhao, Thermoelectric materials: energy conversion between heat and electricity, J. Materiomics 1 (2) (2015) 92–105.

[85] G. Wu, X. Yu, Contributions of chemical potential to the diffusive Seebeck coefficient for bulk semiconductor materials, Eur. Phys. J. Plus 135 (6) (2020).
[86] H.A. Alburaih, S. Aman, S. Mehmood, Z. Ali, S.R. Ejaz, R.Y. Khosa, N. Ahmad, M. S. Al-Buriahi, Z.A. Alrowaili, H.M. Farid, First principle study of opto-electronic and thermoelectric properties of Zintl phase XIn2Z2 (X = Ca, Sr and Z = As, Sb), Appl. Phys. A 128 (5) (2022).
[87] D. Behera, R. Sharma, H. Ullah, H.S. Waheed, S. Mukherjee, Electronic, optical, and thermoelectric investigations of Zintl phase AAg2Se2 (A=Sr, Ba) compounds: a first-principle approach, J. Solid State Chem. 312 (2022), 123259.